Cell

Article

Cell membranes sustain phospholipid imbalance via cholesterol asymmetry

Graphical abstract

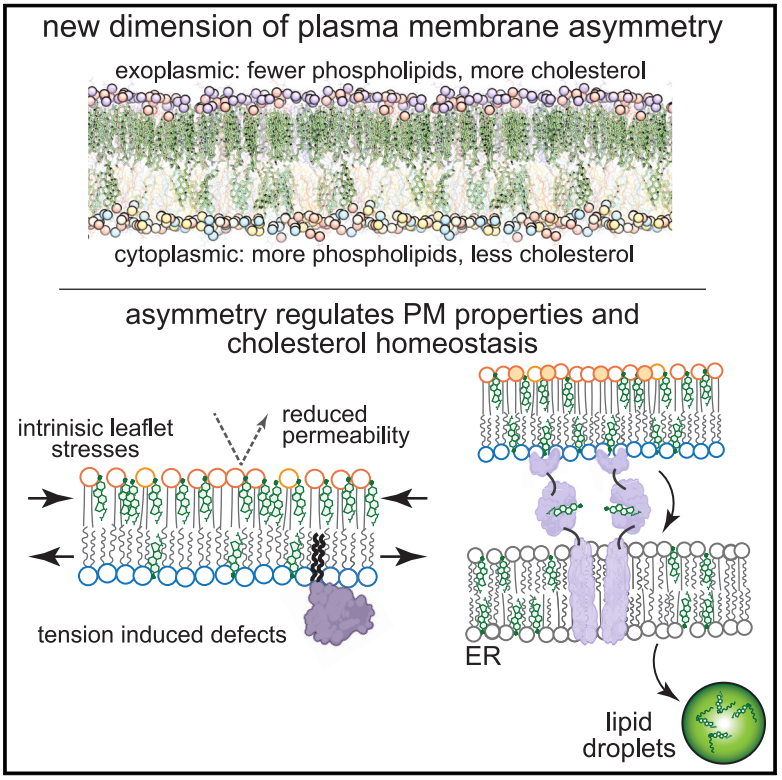

Authors

Milka Doktorova, Jessica L. Symons, Xiaoxuan Zhang, ..., Edward Lyman, Kandice R. Levental, Ilya Levental

Correspondence

milka.doktorova@dbb.su.se (M.D.), krl6c@virginia.edu (K.R.L.), il2sy@virginia.edu (I.L.)

In brief

This work challenges a major assumption in cell biology by showing that lipid bilayers can have drastically different phospholipid abundances between their two leaflets. This lipid abundance asymmetry is enabled by the unique properties of cholesterol and endows biomembranes with distinctive properties and physiological roles.

Highlights

- The two leaflets of mammalian plasma membranes can differ in their lipid abundances
- Phospholipid abundance asymmetry can be stabilized by high cholesterol levels
- Phospholipid and cholesterol asymmetries produce unique membrane properties
- Cellular cholesterol homeostasis is regulated by phospholipid asymmetries

Doktorova et al., 2025, Cell *188*, 2586–2602
May 15, 2025
https://doi.org/10.1016/j.cell.2025.02.034

CellPress

CellPress

Cell

Article

Cell membranes sustain phospholipid imbalance via cholesterol asymmetry

Milka Doktorova,[1,2,*] Jessica L. Symons,[3] Xiaoxuan Zhang,[1] Hong-Yin Wang,[1] Jan Schlegel,[4] Joseph H. Lorent,[5] Frederick A. Heberle,[6] Erdinc Sezgin,[4] Edward Lyman,[7] Kandice R. Levental,[1,*] and Ilya Levental[1,8,*]

[1]Department of Molecular Physiology and Biological Physics, University of Virginia, Charlottesville, VA 22903, USA
[2]Department of Biochemistry and Biophysics, Stockholm University, Science for Life Laboratory, 17165 Solna, Sweden
[3]Department of Integrative Biology & Pharmacology, University of Texas Health Science Center at Houston, Houston, TX 77030, USA
[4]Science for Life Laboratory, Department of Women's and Children's Health, Karolinska Institutet, 17165 Solna, Sweden
[5]Department of Cellular and Molecular Pharmacology, TFAR, LDRI, UCLouvain, Avenue Mounier 73, B1.73.05, 1200 Brussels, Belgium
[6]Department of Chemistry, University of Tennessee Knoxville, Knoxville, TN 37916, USA
[7]Department of Physics and Astronomy, Department of Chemistry and Biochemistry, University of Delaware, Newark, DE 19716, USA
[8]Lead contact
*Correspondence: milka.doktorova@dbb.su.se (M.D.), krl6c@virginia.edu (K.R.L.), il2sy@virginia.edu (I.L.)
https://doi.org/10.1016/j.cell.2025.02.034

SUMMARY

Membranes are molecular interfaces that compartmentalize cells to control the flow of nutrients and information. These functions are facilitated by diverse collections of lipids, nearly all of which are distributed asymmetrically between the two bilayer leaflets. Most models of biomembrane structure and function include the implicit assumption that these leaflets have similar abundances of phospholipids. Here, we show that this assumption is generally invalid and investigate the consequences of lipid abundance imbalances in mammalian plasma membranes (PMs). Using lipidomics, we report that cytoplasmic leaflets of human erythrocyte membranes have >50% overabundance of phospholipids compared with exoplasmic leaflets. This imbalance is enabled by an asymmetric interleaflet distribution of cholesterol, which regulates cellular cholesterol homeostasis. These features produce unique functional characteristics, including low PM permeability and resting tension in the cytoplasmic leaflet that regulates protein localization.

INTRODUCTION

The plethora of molecular processes at the cellular plasma membrane (PM) is enabled by a diverse set of membrane proteins, and also by the membrane's lipid matrix. One characteristic feature of eukaryotic PMs is their compositional asymmetry, i.e., drastically different phospholipid (PL) compositions of the two bilayer leaflets.[1–3] This asymmetry is established and maintained by ATP-driven enzymes that directionally flip PLs across the bilayer.[4,5] Regulation of these processes produces leaflets with distinct compositions and physical properties, including relatively tightly packed exoplasmic leaflets and more charged and fluid cytoplasmic leaflets.[6] The interleaflet distribution of cholesterol (Chol), a major PM component, remains elusive amid conflicting reports.[7] While specific lipid compositions differ between organisms and cell types, structural features of protein transmembrane domains shared across diverse organisms suggest that most eukaryote PMs are asymmetric.[6]

PM asymmetry has been associated with many cellular functions, most notably apoptosis, wherein cell surface exposure of the cytoplasmic leaflet lipid phosphatidylserine (PS) is a central hallmark.[4] PS exposure on platelets is also required for activation of blood coagulation enzymes.[5] This release of lipid asymmetry is often referred to as "scrambling" and is mediated by ATP-independent lipid channels.[5] PM asymmetry has also been implicated in cell-cell fusion,[8] viral entry,[9] and intracellular signaling[10]; however, in most cases, it is not lipid asymmetry per se, but rather its loss that is associated with cellular responses.[11,12] Thus, despite extensive evidence for the prominent chemical and physical asymmetries of PM bilayers, it is yet unknown why most cells expend significant metabolic resources to maintain membrane lipid distributions far away from their symmetric equilibrium.

Here, integrating cellular, biochemical, and computational approaches, we report the discovery of a largely overlooked structural and functional aspect of membrane asymmetry in cells: namely, substantial steady-state PL abundance imbalance between PM leaflets. This imbalance is enabled by asymmetric distributions of Chol, which can rapidly redistribute to buffer leaflet stresses. These unexpected PL and Chol distributions produce unique membrane properties that illuminate the functional roles of PM asymmetry and its regulated release.

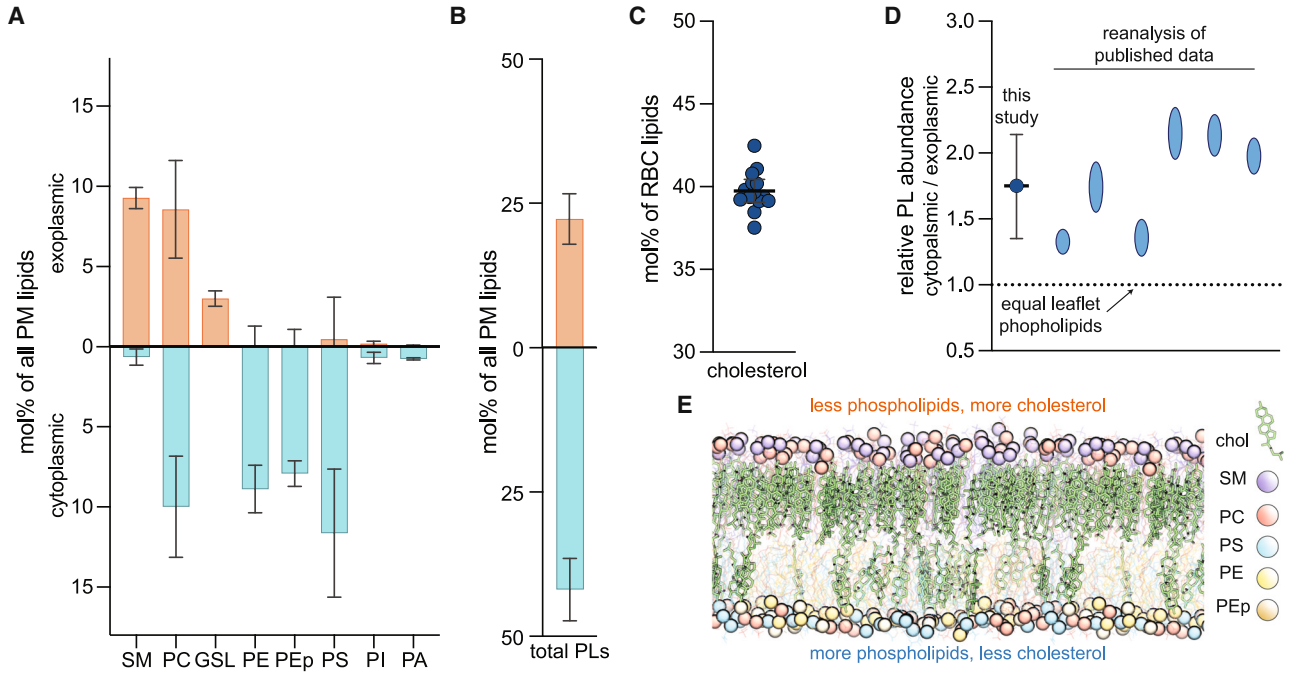

Figure 1. The exoplasmic leaflet of erythrocyte PMs has fewer PLs

(A) Shotgun mass spectrometry quantifications of asymmetric distribution of major lipid classes in the erythrocyte PM. Exoplasmic and cytoplasmic lipidomes are determined by lipase treatment of live cells and include species with a variety of chain compositions. Controls and validations detailed in Lorent et al.[6] Values represent mol % of lipid class as a percentage of PM lipids, with interleaflet distribution shown in orange/blue bars. Average ± SD from >3 independent experiments. SM, sphingomyelin; PC, phosphatidylcholine; GSL, glycosphingolipid; PE, phosphatidylethanolamine; PEp, PE plasmalogen; PS, phosphatidylserine; PI, phosphatidylinositol; PA, phosphatidic acid. Minor classes (<1% not shown).

(B) Total PL (including GSLs) abundances of the two PM leaflets obtained by summing the corresponding leaflet components in (A).

(C) Cholesterol (Chol) measured by lipidomics as a mol % of all erythrocyte lipids. The mean is 40 (±1) mol % of PM lipids; its transbilayer distribution cannot be resolved by this analysis.

(D) Relative total PL abundances between the two PM leaflets of erythrocytes from this work and from re-analysis of previous reports (Table S1).

(E) Snapshot of an equilibrated atomistic computational model of the erythrocyte PM with overabundance of PLs in the cytoplasmic leaflet (Cyto+ model; Table S5). The membrane contains 40 mol % Chol, which converges to an asymmetric distribution with ~3-fold enrichment in the exoplasmic leaflet. Lipid classes are color-coded (phosphorous atoms shown as spheres; Chol in green). Structures of PLs used in simulations shown in Figure S1.

RESULTS

Phospholipid imbalance in PMs

Recently, we combined enzymatic digestion of exoplasmic leaflet lipids with shotgun mass spectrometry to quantify the molecularly detailed compositional asymmetry of nearly all PL classes in the human erythrocyte PM.[6] Here, we completed the characterization of the known erythrocyte PM lipidome by quantifying glycosphingolipids (GSLs) and Chol abundances. We found that GSLs constitute ~15 mol % of exoplasmic leaflet lipids (Figures 1A and S1B) while Chol is present at 40 (±1) mol % of PM lipids (Figure 1C). Due to its rapid transbilayer diffusion, Chol's interleaflet distribution is not accessible by enzymatic approaches.[7]

Internal standards in mass spectrometry measurements allow quantification of individual lipid species, which can then be used to compare total PL abundances between the two PM leaflets. Surprisingly, we found that cytoplasmic leaflet PLs are 1.4- to 2.2-fold more abundant than those resident in the exoplasmic leaflet (Figure 1B) (for simplicity, "PLs" here includes GSLs despite their lack of a phosphate group). Such large differences in PL abundances between leaflets were unexpected because monolayer areas in a near-flat bilayer must match. This imbalance cannot be explained by membrane components not included in this analysis, such as glycosylphosphatidylinositol (GPI)-anchored proteins, phosphoinositides, or protein transmembrane domains (see STAR Methods for estimates and discussion). Notably, differences in interleaflet PL abundances are not unprecedented, with similar imbalances evident when the foundational data that originally reported lipid asymmetry[1,13–16] are reanalyzed (Figure 1D; Table S1).

PL imbalance is sustained by Chol

To investigate the previously dismissed[15] feasibility of a membrane with extensive PL abundance imbalance, we built an atomically detailed computational PM model with lipid compositions of the two leaflets guided by lipidomics data (Table S5). The model was built with more PLs in the cytoplasmic leaflet (relative to the exoplasmic one) and was termed Cyto+ (Figure 1E). The simulated Cyto+ membrane also contained 40 mol % Chol, and the initial interleaflet distribution was adjusted to ensure matching leaflet surface areas. Having the unique ability to

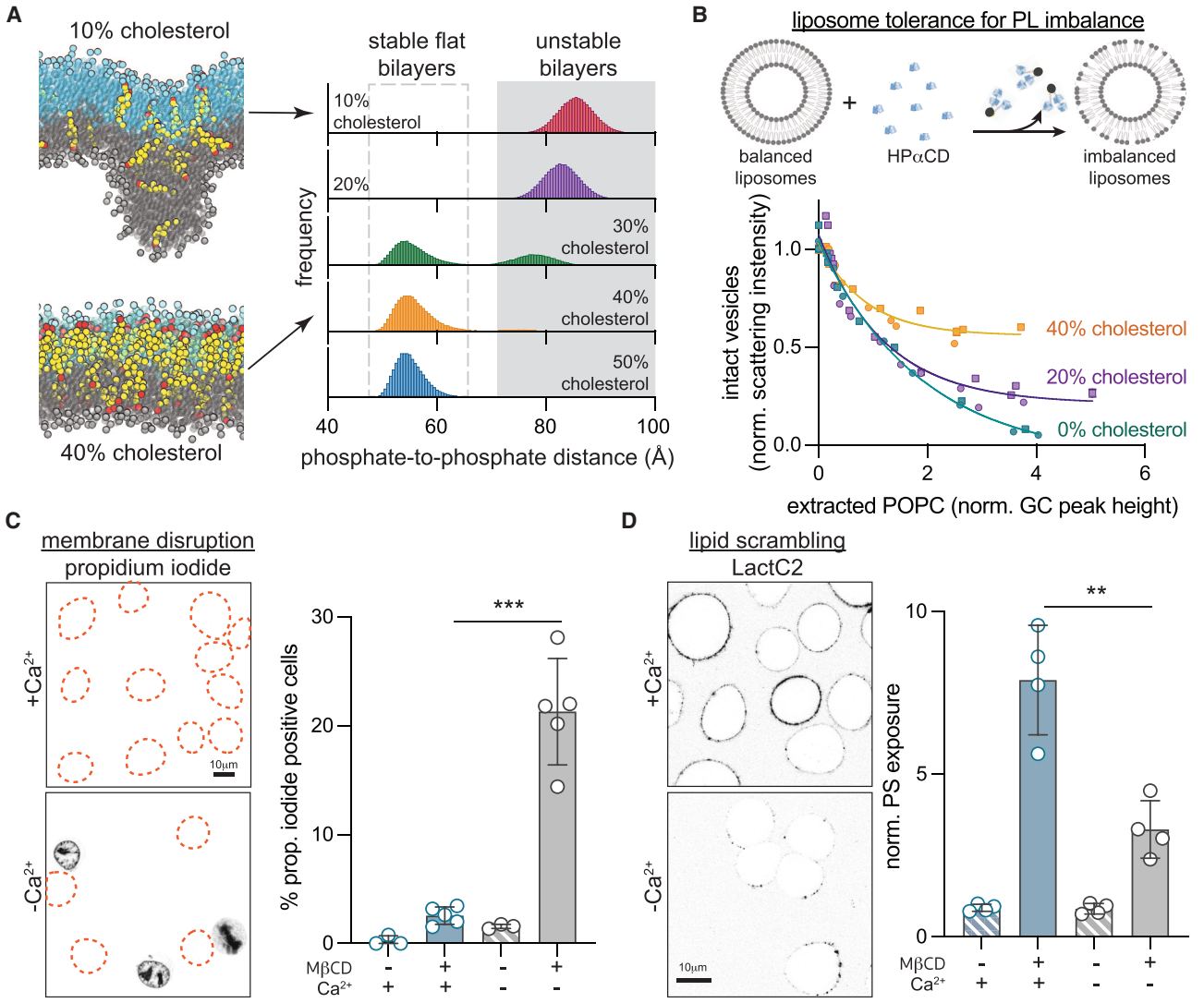

Figure 2. Chol imparts tolerance for PL abundance imbalance between bilayer leaflets

(A) Coarse-grained simulations of a PM model with 35% more PLs in the cytoplasmic leaflet and varying Chol abundance (10%–50%; Table S2). Histograms show the distributions of maximal distances between lipid phosphate groups in the two leaflets. Values >70 Å indicate unstable bilayers with non-lamellar morphology. Representative snapshots from simulated bilayers with 10% and 40% Chol shown for reference (exoplasmic leaflet PL phosphate groups shown in cyan, cytoplasmic in gray, Chol is yellow with hydroxyl headgroup in red).

(B) Extraction of external leaflet PLs from extruded liposomes with 0, 20, and 40 mol % Chol. PLs are extracted from the external leaflet by HPαCD, which induces PL imbalance between leaflets causing membrane instability and liposome destruction. Amount of extracted lipid is quantified by gas chromatography-mass spectrometry (GC-MS), while the corresponding fraction of intact vesicles is measured by light scattering (data from two independent experiments).

(C) Extraction of Chol compromises PM integrity, evidenced by propidium iodide (PI) staining of nuclei, if lipid scrambling is suppressed by chelating Ca^{2+}. Outlines represent PI-negative cells.

(D) Extraction of Chol from the PM of RBL cells with MβCD leads to scrambling of PM lipids evidenced by exposure of PS on the cell surface (binding of external PS-marker, LactC2-mClover), while suppressing scrambling reduces PS exposure. Average intensity of LactC2-mClover on the PM (PS exposure) normalized to −MβCD is shown on the right. Data shown in (C) and (D) are from average ± SD from 3 to 5 independent experiments. Paired t test comparing means of 3–5 independent experiment. Each mean is of >10 cells per experiment. $^{**}p < 0.01$, $^{***}p < 0.001$.

See also Figure S2.

quickly flip-flop between leaflets,[17,18] Chol equilibrated its distribution during the 17-μs-long trajectory (Tables S5 and S6), with 77% of Chol molecules accumulating in the PL-poor exoplasmic leaflet (Figure 1E). Thus, we hypothesized that Chol can enrich in PL-poor leaflets, enabling large interleaflet PL imbalances.

To test this hypothesis, we simulated a series of coarse-grained asymmetric bilayers with fixed PL leaflet imbalance (cytoplasmic leaflet with 35% more PLs than exoplasmic) and Chol abundances ranging from 10 to 50 mol % (Figure 2A; Table S2). In all these simulations, Chol equilibrated to an

asymmetric distribution, accumulating in the PL-poor exoplasmic leaflet (Figure S2A). Notably, low Chol concentrations were unable to sustain stable, flat bilayer morphologies under PL imbalance; instead, the systems adopted unusual, nonlamellar configurations (Figure 2A). In contrast, membranes with $\geq$30 mol % Chol produced stable, flat bilayers, confirming that Chol (in sufficient abundance) enables tolerance for large PL imbalances via its asymmetric interleaflet distribution.

To experimentally evaluate this inference, we measured the tolerance of liposomes to PL imbalance via single-sided lipid extraction (Figure 2B). Large unilamellar vesicles (composed of POPC with 0–40 mol % Chol) were titrated with 2-hydroxypropyl-α-cyclodextrin (HPαCD), a cyclic polysaccharide that avidly extracts PLs but not Chol from the outward-facing membrane leaflet.[19] More HPαCD extracts more PL, inducing larger leaflet imbalances, which ultimately destroy the liposomes, evidenced by decreased light scattering of the suspensions (Figure S2B). By directly quantifying the amount of extracted PL (i.e., induced interleaflet PL abundance imbalance) by gas chromatography, we observed that Chol protects vesicles from destruction in a dose-dependent fashion (Figure 2B), consistent with simulations.

Our lipidomics measurements indicate that Chol comprises ~40 mol % of PM lipids in erythrocytes, consistent with previous estimates in mammalian PMs.[7] Our simulations and synthetic membrane experiments suggest that such high Chol levels are required to sustain large PL imbalances (Figures 2A and 2B). Thus, we hypothesized that extracting Chol from cell PMs would destabilize the bilayer and compromise membrane integrity. To facilitate imaging and genetic manipulations, cellular experiments were conducted with cultured rat basophil leukemia (RBL) cells. We selectively extracted Chol from RBL PMs with methyl-β-cyclodextrin (MβCD), which depletes both PM leaflets through Chol's rapid transbilayer movement[20] but does not extract PLs.[21] Contrary to our prediction, membrane integrity was not affected by MβCD, as revealed by lack of propidium iodide (PI) staining (Figure 2C) or permeability to dextran polymers (Figure S2E). Rather, as previously reported,[22] Chol extraction induced rapid PL scrambling evidenced by externalization of inner-leaflet PS (Figures 2D and S2C), which likely serves to eliminate any pre-existing PL imbalance between leaflets. To suppress scrambling and thereby isolate the effects of PL imbalance, we relied on the calcium dependence of the most widely characterized scramblase TMEM16F.[5] Indeed, treatment of RBL cells with MβCD under Ca^{2+}-free conditions significantly reduced PS exposure (Figures 2D and S2C). Strikingly, this treatment also disrupted membrane integrity, revealed by robust staining of nuclei with PI (Figures 2C and S2D) and leakage of dextran into the cytoplasm (Figure S2E). These results reveal that in response to Chol extraction, PLs are redistributed between PM leaflets to preserve membrane integrity. If this mechanism is inhibited, membrane integrity is lost, supporting the notion that Chol imparts tolerance for interleaflet PL abundance imbalance in living cells.

Chol distribution in the PM

Our Cyto+ model indicates that Chol can balance excess PLs in the cytoplasmic leaflet by accumulating in the exoplasmic leaflet (Figure 1E). PL imbalance in the PM can be established by the activity of enzymes termed flippases, which use ATP to translocate aminophospholipids (PS and phosphatidylethanolamine [PE]) from the exoplasmic to the cytosolic leaflet against their concentration gradient.[5] In the absence of compensatory lipid movement, active lipid flipping from the outer to the inner leaflet would underpopulate the former and over-populate the latter, creating tension in the underpopulated leaflet and compression in the overpopulated one due to the requirement that leaflet areas match despite different lipid abundances. This effect was confirmed by a series of simulations in which increasing numbers of PS lipids were flipped into the "inner" leaflet (Figure 3A). We also found that the resulting stresses could be alleviated by Chol passively "flopping" to the outer leaflet, consistent with previous reports of rapidly flipping lipids buffering leaflet tension.[18,23]

In addition to this stress-buffering role, Chol preferentially interacts with saturated versus unsaturated lipids, especially the saturated sphingomyelins (SMs) that are characteristic of the PM exoplasmic leaflet.[24] To incorporate this effect, we simulated a series of coarse-grained asymmetric membranes with one fully saturated (outer) and one highly unsaturated (inner) leaflet. Interleaflet PL abundances were varied, while Chol was initiated at 30 mol % in both leaflets (Figure 3B). In nearly all cases, we observed net Chol flux toward the outer leaflet (Figure 3B); e.g., when PLs were initially balanced, Chol equilibrates at >40 mol % in the outer leaflet (~4-fold enriched relative to unsaturated leaflet) producing an overpopulated outer leaflet even at the cost of generating, rather than alleviating, membrane stress (Figure S2F). Net Chol flux could only be eliminated in these simulations when the saturated lipid-rich "outer" leaflet had 2-fold more PLs than the inner.

These findings reveal that Chol's preference for certain lipid classes (saturated lipids, sphingolipids) combines with its tendency to populate under-packed leaflets to determine its ultimate transbilayer distribution, as discussed in previous theoretical and computational work.[25–27] In our lipidomics measurements, erythrocyte PM exoplasmic leaflets are more saturated (Figure S1A), rich in sphingolipids (Figure 1A), and PL-underpopulated (Figure 1B), making a strong prediction for Chol enrichment therein.

To test this prediction, we developed an assay to assess Chol distribution in a living cell PM. Erythrocytes were isolated from healthy donors and a small fraction of Chol was exchanged for the fluorescent Chol analog, dehydroergosterol (DHE; Figure 3C), which has similar chemical and biophysical properties.[28,29] We assayed the asymmetric distribution of DHE by fluorescence resonance energy transfer (FRET) to a quencher present only in the outer leaflet (Figure 3C). To that end, we added the fluorophore Di4 (which is charged and cannot flip between leaflets[6]) into the erythrocyte outer leaflet. DHE and Di4 form a FRET pair with a Förster distance that is approximately half the bilayer thickness and therefore exchange energy much more efficiently when they are in the same leaflet (STAR Methods). Thus, Di4-induced quenching of DHE fluorescence provides a readout of the relative outer leaflet enrichment of DHE, as a proxy for Chol's transbilayer distribution. Labeling conditions were tuned to ensure that overall sterol levels and membrane physical properties were unaffected (Figure S3) and that ~50% of DHE is quenched in symmetric liposomes (Figure S4). Titration of Di4

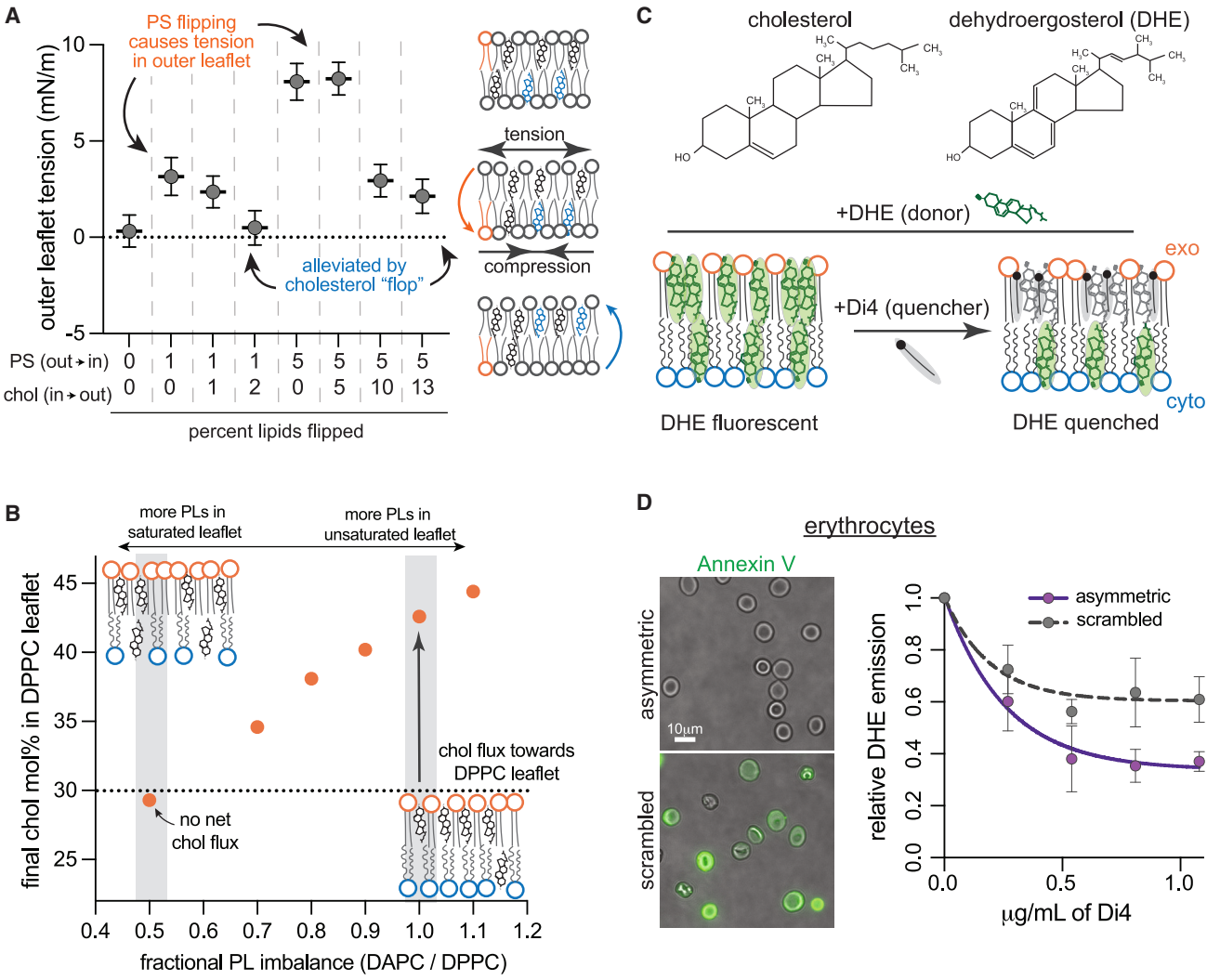

Figure 3. Chol interleaflet distribution in model and cell membranes

(A) Leaflet tension (differential stress) in the outer leaflet of simulated bilayers composed of POPS (PS), POPC, and Chol modeling various extents of PS and Chol flipping. Atomistic bilayers were constructed with the indicated percentage of PS lipids effectively flipped from the outer leaflet to the inner leaflet, and Chol molecules flopped from the inner to the outer leaflet (Table S3). Outer leaflet tension calculated from equilibrated lateral pressure distributions.

(B) Chol distribution in coarse-grained asymmetric bilayers composed of a fully saturated outer leaflet (dipalmitoyl [C16:0] PC, DPPC) with fixed number of PLs opposing a highly unsaturated inner leaflet (diarachidonoyl [20:4] PC, DAPC) with varying PL abundance (Table S4). The fractional imbalance of DAPC-to-DPPC lipids goes from underpopulated DAPC leaflet (left) to underpopulated DPPC leaflet (right). Chol was initiated at 30 mol % in each leaflet. Simulations were run for 10 μs allowing Chol to equilibrate between the two leaflets; the equilibrated Chol concentrations in the outer leaflet are shown. Schematics of the equilibrated relative lipid distributions are shown for comparison.

(C) Schematic illustration of experimental approach for measuring Chol interleaflet distribution in erythrocytes. Minor fraction (<10%) of Chol in the erythrocyte PM is exchanged with DHE. A quencher, Di4, is added externally leading to its insertion into the outer leaflet. The fraction of DHE fluorescence quenched by Di4 provides a readout of relative DHE residence in the exoplasmic leaflet.

(D) DHE fluorescence in erythrocyte membranes as a function of Di4 concentration comparing untreated cells to cells whose PM lipids were scrambled with 100 μM PMA. Representative images show binding of PS-marker annexin V (AnxV) before (top) and after (bottom) PMA treatment. Average ± SD for 3 independent experiments.

into erythrocytes quenched DHE fluorescence, plateauing at ~64% reduction of DHE emission (Figure 3D). Quenching of the majority of DHE fluorescence by an externally applied quencher is consistent with the prediction that Chol is enriched in the exoplasmic leaflet of a living cell PM. This enrichment was eliminated by releasing lipid asymmetry via treatment with phorbol myristate acetate (PMA) (Figure 3D), which scrambles erythrocyte PLs.[30] Thus, computational predictions and experimental measurements suggest that Chol is enriched in the exoplasmic leaflet of human erythrocyte PMs. We discuss caveats and other previous studies of Chol asymmetry in the caption of Figure S4.

Validation of the Cyto+ model

Our results suggest that the exoplasmic leaflet of human erythrocyte PMs is relatively saturated, PL-depleted, and Chol-rich, a model of PM structure that we termed Cyto+. A large, atomistic simulation of this model was stable over >17 μs with Chol continuing to partition away from the cytoplasmic leaflet, producing an exoplasmic leaflet with high density, lipid packing, and acyl chain order (Figures S5A–S5E). To validate this emerging model of lipid organization and membrane structure, we developed methods to quantitatively compare its structural and dynamical properties with those of living cell membranes. Previous measurements used the leaflet-specific fluorescence lifetime of Di4[6] to infer that the exoplasmic PM leaflet of mammalian cells is more tightly packed than the cytoplasmic. To examine how leaflet imbalances contribute to this observation, we calibrated experimental Di4 lifetimes to simulated lipid packing (i.e., area/lipid) in simple synthetic bilayers spanning a range of lipid densities (Figure 4A). These two measures were highly correlated, allowing us to translate experimental Di4 lifetimes into a specific membrane structural parameter (area/lipid). We found that the exoplasmic PM leaflet of NIH 3T3 fibroblasts is ∼20% more tightly packed (40.9 ± 2.31 Å^2/lipid) than the cytoplasmic leaflet (51.2 ± 2.22 Å^2/lipid) (Figure 4C, hatched bars). We directly compared these measurements with three distinct models of PM organization: in addition to the Cyto+ model (Figure 1E) derived from lipidomics and supported by measurements (Figures 3C and 3D), we simulated two alternative models with identical leaflet lipid *compositions* but either equal (Equal) or greater (Exo+) PL *abundance* in the exoplasmic monolayer (Figure 4B; Tables S5 and S6). The lipid packing of the exoplasmic leaflet of the Cyto+ model matched nearly perfectly with the experimental measurement, while Exo+ was least accurate (Figure 4C, left). Further, the large difference in area/lipid between the two leaflets was successfully captured only by the Cyto+ model (Figures 4C and S5F). We also simulated a scrambled version of Cyto+ (i.e., same lipid composition, but all lipids equally distributed between leaflets) and observed an intermediate lipid density between the exoplasmic and cytoplasmic leaflets, which matched very closely to experimental measurements of the fibroblast PM scrambled by treatment with the calcium ionophore A23187 (Figure 4D). Thus, leaflet structural differences in living mammalian cells are most consistent with an overabundance of PLs in the cytoplasmic leaflet (Cyto+).

Next, we investigated the correspondence in lipid *dynamics* between live cells and our Cyto+ model by comparing lipid diffusion in simulated membranes with measurements in cells (Figures 4E–4H). Recently, it was reported that a pool of cellular Chol diffuses much faster than PLs in both cultured cells and chordate embryos, which was notably different from synthetic, cell-derived, and computational model membranes, where the two lipid types diffused similarly.[31] Thus, this rapidly diffusing pool of Chol may be a hallmark of the lipid organization of living cell PMs.[31] We confirmed these findings in fibroblast PMs by measuring diffusion of fluorescently tagged SM (TF-SM[32]) and Chol (TF-Chol[33,34]) via fluorescence correlation spectroscopy (FCS) (Figures 4E and 4F). TF-Chol diffused 1.6-fold faster than TF-SM, and this difference was eliminated by scrambling PM lipids. Similar trends were observable in the Cyto+ simulation: overall, Chol diffused 1.7-fold faster than SM, and this difference was eliminated by lipid scrambling (Figure 4G). Further comparison between Chol and PL diffusion in each leaflet revealed that these differences were attributable to the much faster diffusion of Chol (relative to PLs) in the cytoplasmic PM leaflet (Figure 4H). In contrast, large differences between Chol and PL diffusion were not observed in any of the leaflets of the Exo+ and Equal models (Figure 4H). Consistently, Chol has been reported to diffuse faster than PLs only in simulations of highly unsaturated, loosely packed membranes with low Chol concentration.[35] Thus, the previously reported unexpected dynamics of Chol in mammalian PMs are consistent with the unusual lipid configurations proposed by the Cyto+ model.

Functional consequences of lipid imbalances

Having validated the compositional, structural, and dynamical features of the Cyto+ PM model against cell measurements, we examined the consequences of this unconventional lipid organization on membrane biophysical properties. The large lipid asymmetries suggest the presence of stress in the membrane, and we first calculated the lateral pressure distribution in each leaflet (Figure 5A). While the bilayer has no net stress, the exoplasmic leaflet is compressed to 8.2 ± 0.8 mN/m while the cytoplasmic leaflet is under tension of the same magnitude. Such balanced compressive/tensile forces in an overall-tensionless membrane are termed "differential stress."[25,36] In the Cyto+ model, differential stress arises both from differences in leaflet PL abundances and from Chol's preference for the outer leaflet. Lipid scrambling eliminates lipid asymmetries and alleviates differential stress (Figure S5H).

Based on its significant lipid compression, we hypothesized that the Chol-enriched outer leaflet may constitute a robust barrier to transbilayer permeability. This hypothesis was tested first *in silico* by calculating the flux of water molecules through the bilayer (i.e., entering from one side and exiting from the other). Comparing the Cyto+ model with its scrambled counterpart revealed that the scrambled PM was ∼80% more permeable to water than the asymmetric PM (Figure 5B), highlighting a functional PM property arising from asymmetric lipid distribution, rather than overall lipid composition. To experimentally validate this observation, we investigated asymmetry-dependent PM permeability in erythrocytes. We measured transbilayer permeation of a small molecule, fluorescein diacetate (FDA), which becomes fluorescent only after encountering intracellular esterases. Because transbilayer flux is the rate-limiting step in this assay, the rate of fluorescence increase is directly proportional to membrane permeability.[37] Scrambled erythrocytes were ∼35% more permeable to FDA than asymmetric controls (Figure 5C), in qualitative agreement with the computational observation (Figure 5B). Simulations further suggested that this difference is likely due to the tightly packed outer leaflet, which presents the main barrier to transbilayer permeation in the Cyto+ model. We observed many partial transitions of water molecules entering and exiting the cytosolic leaflet, but none from the exoplasmic leaflet (Figure 5D), illustrating the bipolar nature of the asymmetric membrane.

The low lipid packing, high resting tension, and high permeability of the cytoplasmic leaflet in the Cyto+ model suggest

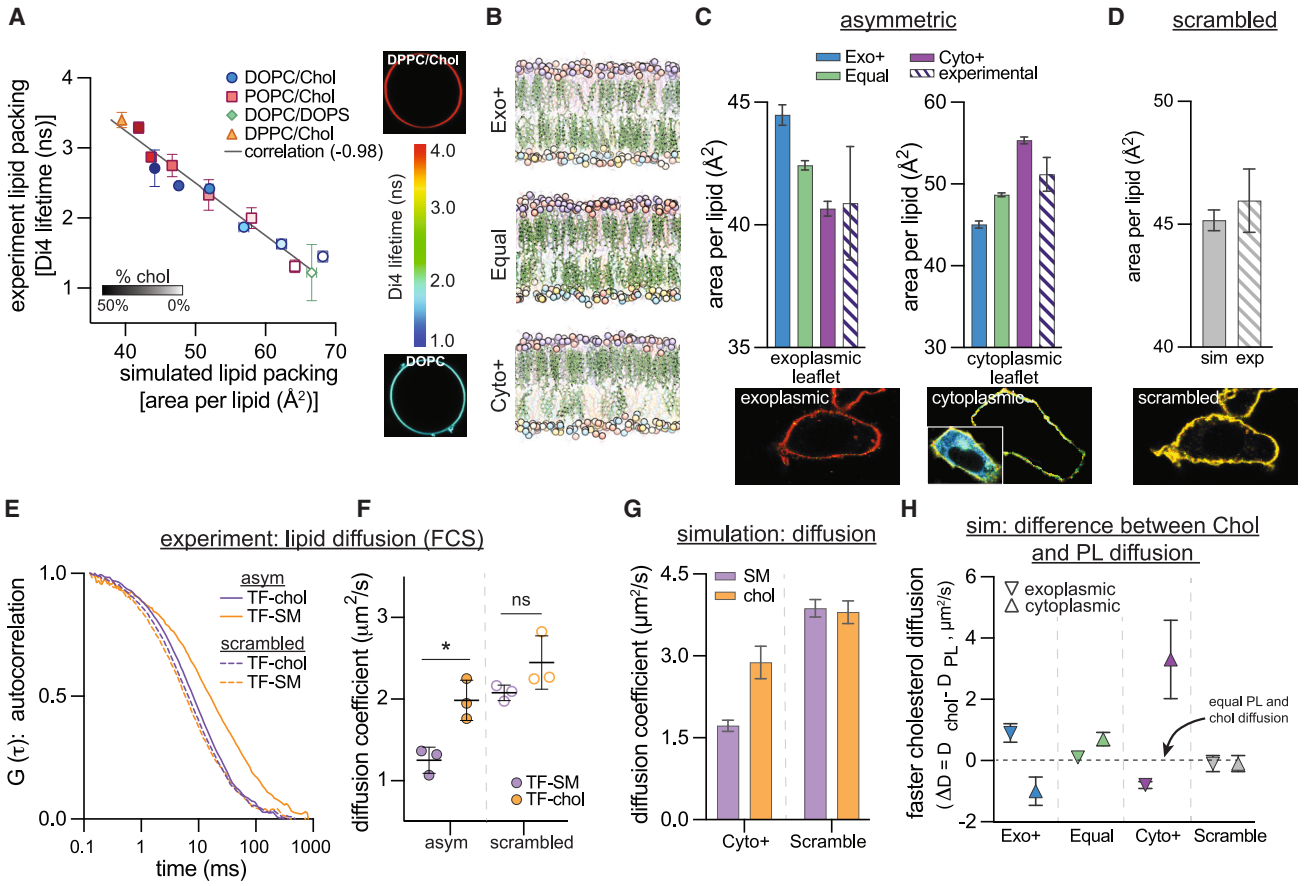

Figure 4. Experimental validation of Cyto+ model

(A) Calibration of Di4 lifetime, an experimental reporter of lipid packing measured in giant unilamellar vesicles (GUVs), with simulated area per lipid (APL) across a set of synthetic symmetric bilayers. Shown is average ± SD of individual experiments. Representative images of the least and most tightly packed GUVs are shown on the right. Color bar indicates Di4 lifetime. Light- to dark-filled symbols represent increasing mol % of Chol.

(B) Snapshots of three simulated PM models having more PLs in their exoplasmic (top) or cytoplasmic (bottom) leaflets, or similar numbers of PLs in both leaflets (middle). Lipid representation is the same as in Figure 1E.

(C) Leaflet packing densities (APL) from the three simulated PM models with different interleaflet PL abundances from (B) compared with experimental measurements in PMs of live fibroblasts.

(D) APL of the scrambled Cyto+ model compared with the experimentally scrambled fibroblast PM (via ionophore treatment). Representative images at bottom of (C) and (D) are of Di4 lifetime in the PM of fibroblast cells (color scale for lifetime shown in A). "Cytoplasmic" panel shows the masked PM of a microinjected cell with full image as an inset.

(E) Representative FCS curves for TF-SM and TF-Chol in the PM of live fibroblasts before (asym) and after (scrambled) ionophore treatment.

(F) Corresponding diffusion coefficients of TF-SM and TF-Chol calculated from FCS measurements. Data points represent means of three biologically independent replicates, each with >5 cells and >5 measurements per cell; thus, each point is the average of >25 FCS curves. Paired t test of the means of the 3 independent experiments. *$p < 0.01$.

(G) Diffusion coefficients of SM and Chol in the simulated Cyto+ membrane (left) and its scrambled counterpart (right). Chol diffusion in Cyto+ represents the asymmetry-weighted average of the slowly diffusing population in the exoplasmic leaflet and the rapidly diffusing population in the cytoplasmic leaflet (Figure S7A).

(H) Difference between Chol and PL diffusion (ΔD) in each leaflet of the simulated asymmetric PM models and the Cyto+ scrambled membrane. Errors in (G) and (H) were calculated from bootstrapping as detailed in STAR Methods. All simulations shown in this figure are all-atom.

the likelihood of frequent hydrophobic defects, i.e., areas where the hydrophobic bilayer core is transiently exposed to water. Consistent with this prediction, simulations revealed that the Cyto+ cytoplasmic leaflet has more and larger deep hydrophobic defects than either the exoplasmic or scrambled leaflets (Figures 5E and 5F). Such defects have been previously implicated as "binding sites" for peripheral proteins that interact with membranes through hydrophobic moieties such as lipid anchors[38] or amphipathic helices.[39,40] Our analysis predicts that the structure of the Cyto+ membrane facilitates peripheral protein binding to the cytoplasmic leaflet by promoting the insertion of hydrophobic anchors.[38]

To test this hypothesis in live cells, we examined the asymmetry-dependent PM binding of a short lipidated peptide, the SH4

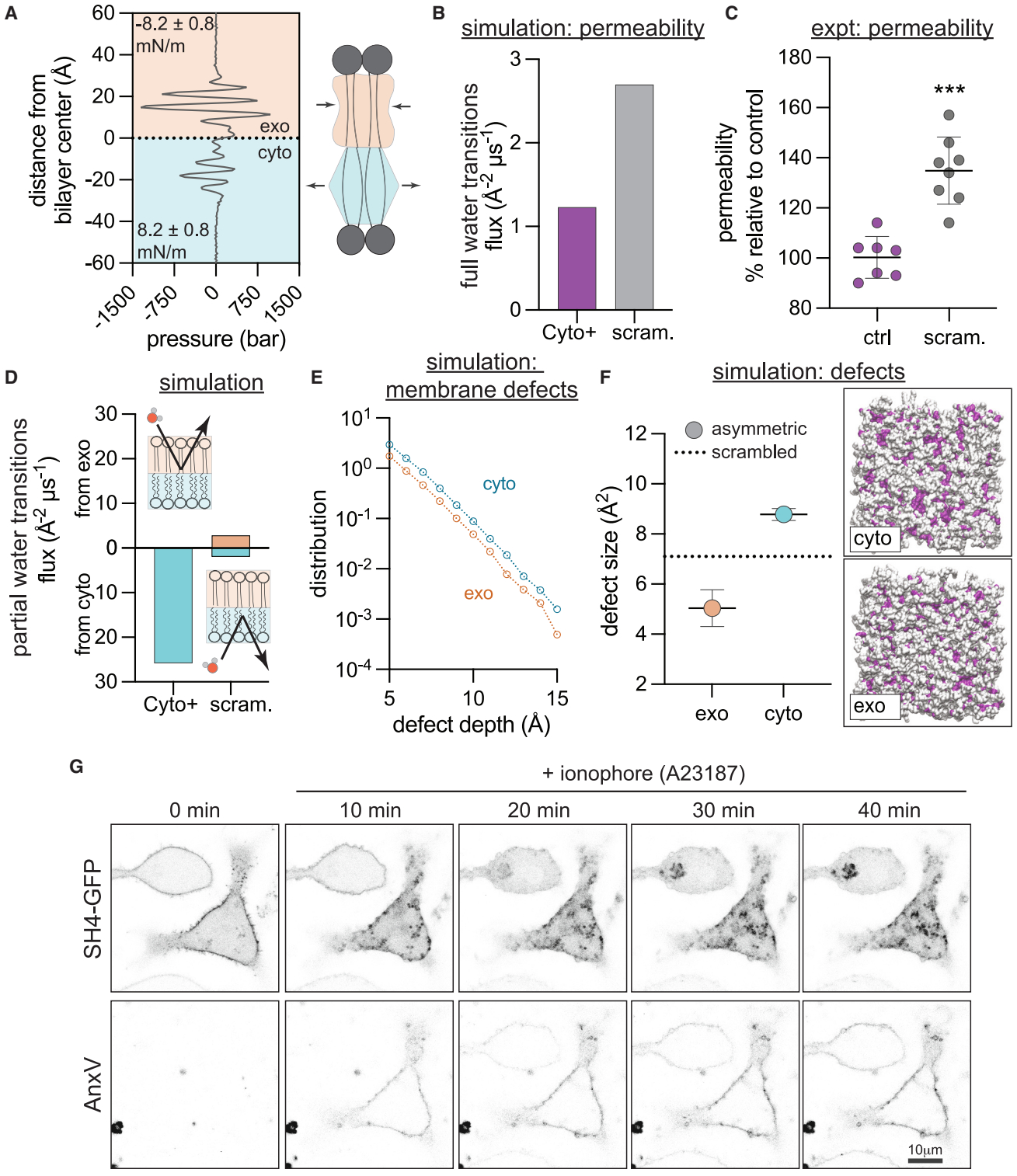

Figure 5. Biophysical features of the Cyto+ model

(A) Transbilayer lateral pressure distribution in the simulated Cyto+ PM shows that the bilayer is differentially stressed, i.e., the exoplasmic leaflet (orange) is compressed while the cytoplasmic leaflet (cyan) is under tension of the same magnitude.

(B) Simulated water flux through Cyto+ compared with scrambled PM.

(C) Experimental permeability of erythrocyte membranes to FDA. PMA-scrambled erythrocytes shown relative to untreated asymmetric controls. Shown are average ± SD of ≥7 independent experiments; unpaired t test were performed on the means of the experiments.

(legend continued on next page)

domain of the Src-family kinase Lyn, which associates with membranes via two lipid anchors (Figure 5G). To release PM asymmetry, cells were treated with A23187, a calcium ionophore that induces scrambling (evidenced by binding of the PS-marker annexin V [AnxV] to the cell surface). In untreated cells, AnxV did not bind, and the peptide localized largely at the PM. Ionophore treatment produced the predicted scrambling (i.e., AnxV binding), but also a concomitant detachment of the peptide from the PM and relocation to the cytosol and intracellular organelles (Figure 5G). The same behavior was observed for two other peptides representative of the membrane anchoring domain of an unrelated peripheral protein, H-Ras (Figure S6). These peptides bear no overall charge, suggesting that their behavior was not dependent on changes in inner leaflet electrostatics.[41] Rather, the general desorption of lipidated peptides from the PM after scrambling suggests that their PM association is likely mediated by the deep hydrophobic defects that arise in the tensed, Chol-poor cytosolic leaflet.

Transbilayer lipid imbalance regulates cellular Chol sensing

To explore the physiological consequences of asymmetric lipid distributions, we inferred that since most cellular Chol sensing and transfer machinery is in the cytoplasm, only cytoplasmic leaflet Chol would be relevant to these processes. Therefore, manipulating the determinants of Chol's transbilayer distribution would be expected to affect cellular Chol handling. To test this hypothesis, we manipulated two of these determinants: outer leaflet SM (Figure 6) and transbilayer PL abundance (Figure 7).

Chol accumulates in the exoplasmic PM leaflet in part due to its preferred interactions with saturated sphingolipids. Thus, we reasoned that reducing SM levels would lower Chol's affinity for the outer leaflet, leading to its redistribution to the inner leaflet (Figure 6A). Simulations supported this inference, as replacing SM with ceramide (Cer) in simulated asymmetric membranes (see Figure 2A) notably reduced Chol asymmetry and increased its concentration in the cytoplasmic leaflet (Figure 6B). To explore this effect experimentally in living cells, we used a cytoplasmic Chol-binding probe based on the Chol-sensing element of the transport protein GRAMD1b (Aster-B). The isolated GRAM domain of this protein has been engineered into a biosensor (GRAM-H), which translocates to the PM when "accessible Chol" is increased.[42] We observed a robust and significant increase in PM recruitment induced by treating cells with sphingomyelinase (SMase) to convert SM into Cer (Figure 6C) or by inhibiting SM synthesis with myriocin (Figure 6D). Thus, reducing outer leaflet SM increased inner leaflet Chol. These results are quantitatively consistent with previous observations[42] and provide a mechanistic explanation: Chol "accessibility" is determined, at least in part, by its transbilayer asymmetry. How this SMase-liberated inner leaflet Chol pool corresponds to the ~30% of PM Chol that becomes accessible to probes binding on the outer leaflet after SMase treatment remains to be determined.[43]

To manipulate transbilayer PL imbalance, we developed a method to increase the PL abundance of the PM outer leaflet without changing its composition (Figure 7A). We extracted outer leaflet PLs from a confluent dish of "donor" RBL cells at 37°C with MαCD. We then transferred the PL-saturated-MαCD to a new dish of "acceptor" RBL cells, which had lower confluence and incubated at 4°C (Figure 7A). We reasoned that lower temperature reduces the solubility of PL in MαCD and leads to its deposition into the acceptor cells, as it does in synthetic systems.[44] To test this hypothesis, we measured the lipid abundance in the PL-MαCD solution before and after incubation with acceptor cells and found that 4 nmol of PLs could be delivered to ~3×10^5 cells (Figure 7B), increasing outer leaflet lipid abundance in acceptor cells by ~40% (see STAR Methods for details). This manipulation did not induce PM lipid scrambling nor extensive PM deformations[45] (Figure S8C).

According to our hypothesis, increasing PL abundance in the outer leaflet should redistribute Chol to the inner leaflet (compare Cyto+ versus Exo+ in Figure 4B), and indeed, we observed significant recruitment of GRAM-H to the PM upon outer leaflet lipid loading (Figure 7C). Similar effects were observable when the PM was loaded with pure synthetic lipids (Figures S8E and S8F). We then hypothesized that the increase in inner leaflet Chol would activate cellular Chol homeostasis machinery, leading to Chol transport to internal organelles. The machinery mediating such PM-to-ER Chol transport has been recently identified as the GRAMD1/Aster proteins, which are residents of the endoplasmic reticulum (ER) that translocate to PM-ER contact sites upon Chol loading and use their StAR (steroidogenic acute regulatory) domains to shuttle excess PM Chol to the ER.[46–48] We observed translocation of GRAMD1A (Figure 7D) and GRAMD1B (Figure 7E) to puncta at the PM induced by loading either outer leaflet or synthetic PLs (Figure S8G) into the PM outer leaflet, presumably due to Chol redistribution to the inner leaflet. Consistent with our inference that GRAMD1b transports excess cytosolic leaflet Chol from the PM to the ER, the membrane packing sensor C-Laurdan reported a significant increase in lipid packing of internal cell membranes induced by loading the outer leaflet with PLs (Figure 7F).

During Laurdan imaging, we noted spherical structures with unusually high GP values (Figures 7F and S8D), which have been previously associated with Chol ester-rich lipid droplets (LDs).[49]

(D) Flux of water molecules partially permeating the leaflets in simulations, i.e., entering the bilayer from the exoplasmic (top) or cytoplasmic (bottom) leaflet and exiting from the same leaflet.
(E and F) Hydrophobic defects in leaflets of simulated Cyto+ membrane and its scrambled counterpart.
(E) Histogram comparing defect sizes in the two Cyto+ leaflets.
(F) Defect size constants of deep defects in the Cyto+ leaflets (data points) compared with the scrambled bilayer (dashed line). Illustrative simulation snapshots of the Cyto+ bilayer viewed from the Cyto or Exo leaflet show shallow (in white) and deep (in color) solvent-exposed areas (defects) in surface representation. Opposite leaflet is shown in gray. Errors are standard deviations calculated from block averaging.
(G) Redistribution of lipidated peptide, the SH4 domain of Lyn (SH4-GFP), in RBL cells induced by PM scrambling with A23187, evidenced by concomitant exposure of PS monitored by the PS-marker AnxV-647. ***$p < 0.001$.
See also Figures S5 and S6.

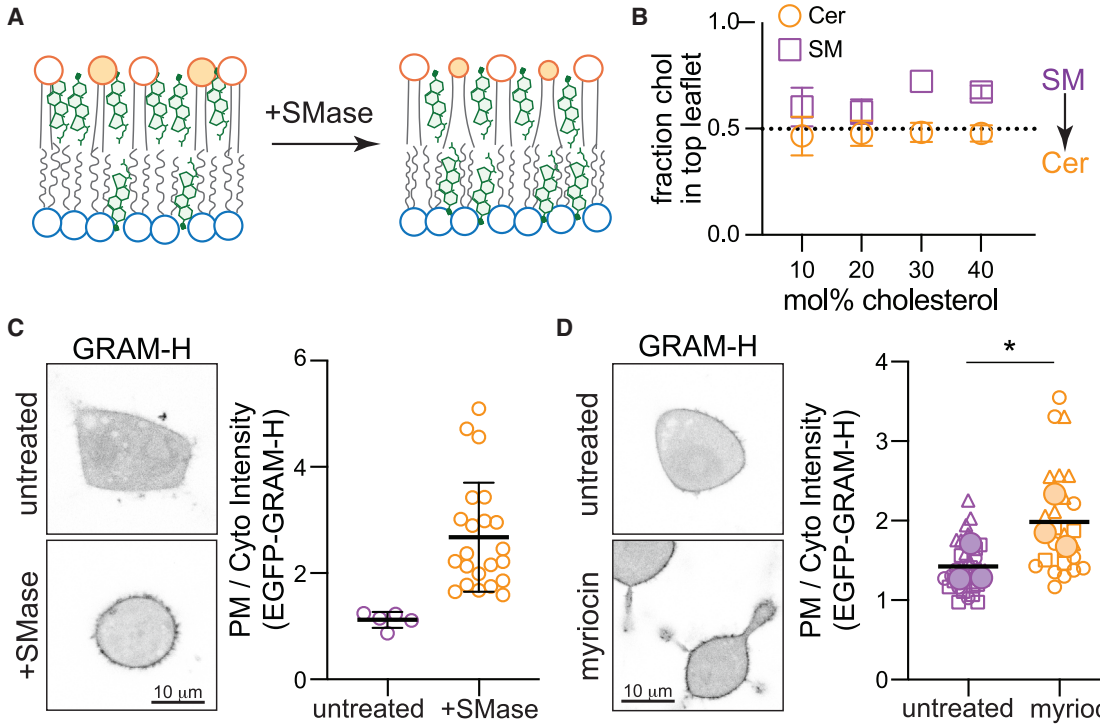

Figure 6. SM drives Chol asymmetry

(A) Schematic of proposed Chol redistribution induced by SMase.

(B) Interleaflet Chol distributions in CG simulations of the simplified PM model from Figure 2A before (purple) and after (orange) all SM has been converted to Cer.

(C) EGFP-GRAM-H localization in RBL cells following SMase treatment; representative images on left, quantification on right. Each data point is a cell. Symbols represent individual cells, with error bars showing mean and SD.

(D) EGFP-GRAM-H localization in RBL cells treated with 25 μM myriocin for 24 h; representative images on left, quantification on right. Small symbols represent individual cells, with symbol shapes denoting independent experiments. Filled larger symbols are means of the 3 independent experiments. Paired t test on means of independent experiments; $^*p < 0.05$.

We hypothesized that these may represent newly accumulating LDs induced by the transfer of Chol to the ER, which activates cellular Chol storage via its esterification and deposition into LDs.[50] To assay LD accumulation, we stained cells with the neutral lipid dye Bodipy 493/503, which accumulates in LDs, and imaged cell volumes by confocal microscopy (Figure 7G). We observed a robust increase in the number, size, and fluorescence intensity of LDs induced by PL loading (Figures 7G–7I, S8H, and S8I), similar to loading cells directly with Chol (Figures S8L and S8M). We observed the same effect after SMase treatment (Figures S8J and S8K), consistent with SMase inducing redistribution of Chol to the cytoplasmic leaflet (Figure 6), as previously shown.[43] To confirm that these LDs were due to increased Chol esterification, we inhibited the enzyme responsible for Chol esterification, acyl-coenzymeA:Chol acyltransferase (ACAT). Indeed, ACAT inhibition blocked accumulation of LDs induced by outer leaflet PL loading (and SMase), confirming their dependence on Chol esters (Figures 7J and S8H–S8M).

These observations reveal that cellular Chol sensing, homeostasis, and storage can be activated without changes in Chol levels (Figure S8B), but rather by Chol's transbilayer distribution, which can be regulated by the PL composition and abundance of PM leaflets.

DISCUSSION

We report a previously overlooked feature of cell membranes: large differences in steady-state PL abundance between bilayer leaflets, facilitated by asymmetric Chol distribution. High Chol concentrations support bilayer tolerance for the large PL imbalances revealed by our lipidomics measurements (Figures 1 and 2), and Chol extraction compromises membrane integrity (Figures 2C–2E). While the relative paucity of PLs in exoplasmic leaflets was unexpected and had not been widely reported, reanalysis of previous measurements of lipid asymmetry is consistent with our observations (Figure 1D; Table S1). This result was perceived as physically unrealistic due to the usually implicit assumption that leaflets with equal areas must also contain similar PL abundances.[15] This assumption is fundamental to most current conceptions of biomembrane lipid distributions, underlying the interpretations and design of most experiments and models. However, theory,[25] simulations, and our measurements reveal that this assumption is generally invalid and is likely incorrect for some mammalian PMs.

Chol sustains interleaflet PL imbalances by accumulating in PL-poor leaflets. This capacity is enabled by Chol's uniquely rapid passive diffusion between leaflets. Chol's equilibrium

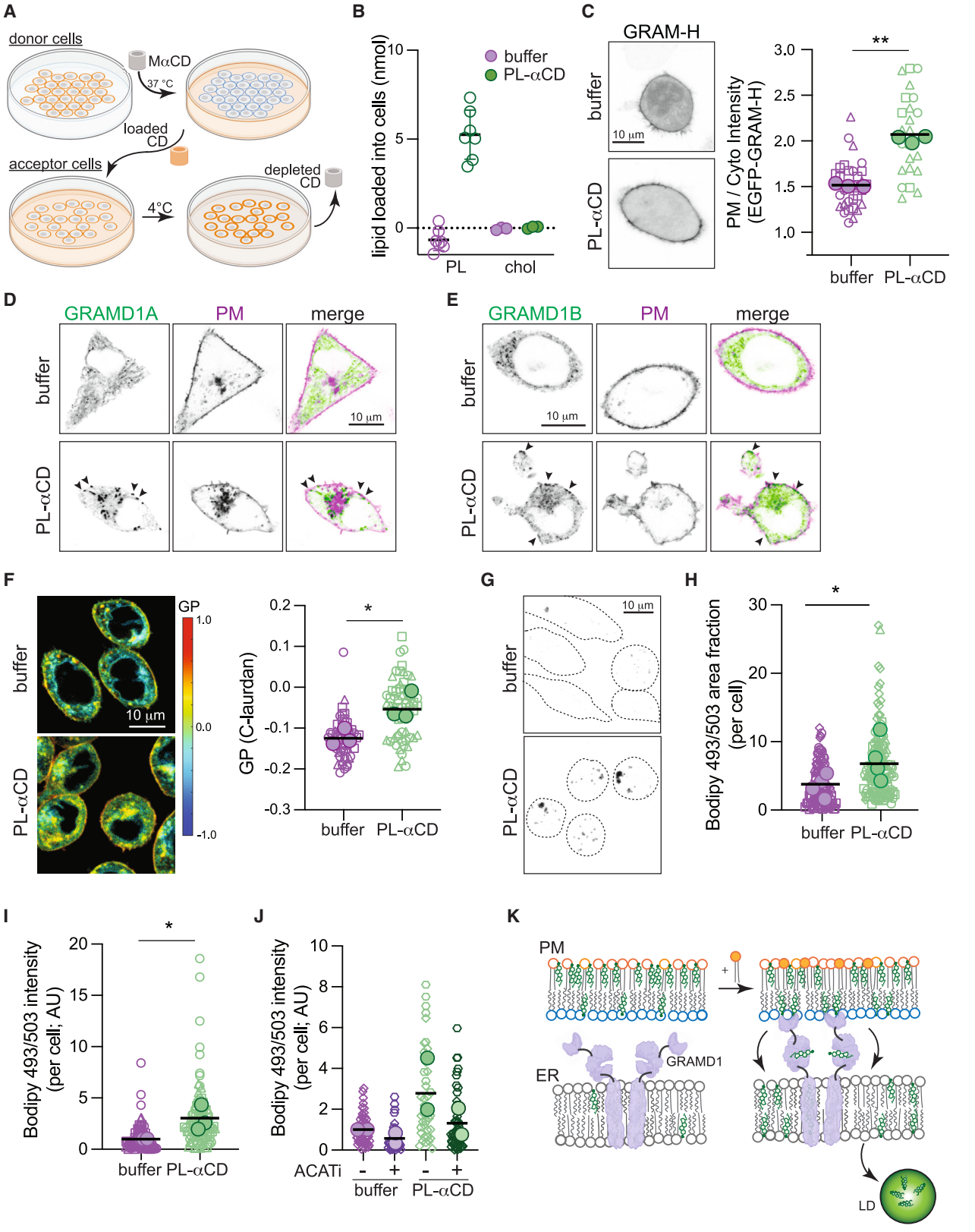

(legend on next page)

distribution is determined by a balance of its tendency to "fill gaps" in the underpopulated leaflet, its preference for saturated and sphingolipids, and entropic effects favoring symmetric arrangement (Figures 3A and 3B). The balance between these factors is described in an elegant theory by Deserno and co-workers.[25,51] As exoplasmic leaflets in our measurements are not only more saturated but also relatively PL-poor, Chol is predicted to enrich in the exoplasmic leaflet. Consistent with this reasoning and theoretical predictions,[25] we observe enrichment of Chol in the erythrocyte outer leaflet (Figure 3D). This result is consistent with a study that used engineered sensors to infer much higher Chol concentrations in the outer PM leaflet.[52] Notably, in the two recently reported structures of membrane proteins determined in native cell membranes,[53,54] cholesterol was associated to the exoplasmic side of the transmembrane domains, consistent with its enrichment in the exoplasmic leaflet. The possibility of significant Chol enrichment in one leaflet was questioned on the theoretical grounds that its rapid flip-flop would appear to preclude significant disparity between leaflets.[7] Our findings reveal a simple mechanism that not only allows, but demands, interleaflet Chol imbalances. While other studies have reported on Chol's distribution in PMs (Figure S4, caption), our model provides a mechanistic explanation for Chol's ultimate transbilayer distribution.

Experimental measurements of leaflet lipid packing support our model of a PM with a PL-rich and Chol-poor cytoplasmic leaflet (Figures 4A–4D and S5). Similarly, experimentally observed fast Chol diffusion (Figures 4E and 4F) appears to be a signature of a differentially stressed, unsaturated lipid-rich, Chol-poor leaflet (Figures 4G, 4H, and S7), consistent only with the Cyto+ model. The inference that the cytoplasmic PM leaflet is under tension may seem contradictory with its relative over-abundance of PLs (Figure 1). However, in the presence of Chol, such stresses are not solely the result of lipid imbalances, but rather several independent drivers of Chol distribution (Figure 3), which can induce, rather than alleviate, leaflet tension (Figure S2F). It may be surprising that a membrane with one compressed and one tensed leaflet would not spontaneously deform (i.e., bend) to alleviate these stresses. However, differential stress can be balanced by curvature stresses arising from differences in the preferred (spontaneous) curvatures of leaflet lipids,[26] which is the case for the Cyto+ PM model (Figure S5I). Further, other mechanical constraints (most prominently the cytoskeleton) may prevent spontaneous bending in living cells.

The asymmetric distributions of PLs and Chol in the two PM leaflets revealed by our analyses have far-reaching implications for biomembrane structure and function (Figures 5, 6, and 7). Lipid abundance asymmetries between the two PM leaflets provide cells with novel regulatory modes, namely the possibility of tuning leaflet packing, tension, and dynamics independent of lipid chemistry. These arrangements may underlie PM properties such as low permeability and regulated binding of lipidated proteins and may be relevant for cellular responses to membrane lipid perturbations, e.g., in genetic diseases of (sphingo)lipid metabolism[55,56] or from dietary lipids.[37] Crucially, abundance asymmetry also regulates the mechanisms of cellular Chol homeostasis (e.g., trafficking, efflux, and storage), which underlie sterol uptake,[57] bile acid production,[58] steroid hormone synthesis,[46] and the levels of circulating lipoproteins that are strongly predictive of cardiovascular disease.[59] We therefore posit that abundance asymmetry of membrane lipids presents a previously unexplored, yet broadly consequential dimension of PM organization and function.

Limitations of the study

The most significant limitation of our study is that direct analysis of lipidomic asymmetry remains limited to erythrocyte PMs. While the general features of this asymmetry (e.g., charged lipids confined to inner leaflet) have been confirmed in many contexts,[11] neither the detailed lipid compositions of PM leaflets nor their abundance imbalances can be directly measured in nucleated cells using currently available methods. The same limitation persists for organellar membranes. Similarly, directly measuring Chol asymmetry remains a major technical challenge: our experiments reveal relative enrichments but not absolute concentrations. In the context of these limitations, it is important to emphasize that both parameters (leaflet composition and interleaflet abundance imbalance) are likely context dependent, being determined by a complex interplay between cell state (e.g., lipid metabolism and membrane trafficking) and its environment (e.g., raw materials for lipid synthesis). Thus, there is unlikely to be a single, universal description of living membrane asymmetry; rather, our study emphasizes that PL and Chol abundance imbalances are an independent, regulated,

Figure 7. Chol homeostasis is regulated by PM transbilayer PL distribution

(A) Schematic of PL loading into the PM outer leaflet of target cells via MαCD extraction of PL and loading onto fresh cells.

(B) Quantification of PL and Chol loading into ~3 × 10^5 RBLs via PL-MαCD.

(C) EGFP-GRAM-H localization in cells treated with PL-MαCD; representative images on left, quantification on right.

(D and E) (D) EGFP-GRAMD1A and (E) EGFP-GRAMD1B localization in cells treated with PL-MαCD (co-expressing a PM marker, magenta). Arrowheads denote GRAM protein puncta at the PM induced by PL-MαCD.

(F) Left, C-Laurdan GP maps of cells treated with PL-MαCD. Warm colors represent higher GP (i.e., tighter lipid packing). Right, quantification of GP of internal membranes.

(G) Bodipy 493/503 staining of cells treated with PL-MαCD. Representative confocal max projection images.

(H) Quantification of area fraction with Bodipy 493/503 staining per cell.

(I) Quantification of total Bodipy 493/503 intensity per cell.

(J) Quantification of Bodipy 493/503 intensity in cells treated with PL-MαCD with and without ACAT inhibition (1 μg/mL Sandoz 58-035).

(K) Schematic of Chol translocation from the outer leafler of the PM to LDs when PLs are loaded to the outer leaflet.

In (C), (F), and (H)–(J), small symbols represent individual cells, with symbol shapes denoting independent experiments. Filled larger symbols are means of independent experiments. Paired t test on means of independent experiments; $p < 0.05$, $p < 0.01$.

See also Figure S8.

physiologically important aspect of the membrane phenotype.[60] Finally, our study focuses solely on computational, synthetic, and cultured cell models, thus its implications for physiological lipid homeostasis remain hypothetical. While the epidemiological connections between diet, health, and disease are among the strongest correlations in biomedicine, underlying mechanistic understanding remains incomplete. Whether and how transbilayer lipid asymmetries affect these mechanisms of physiological lipid handling is an important future direction of research.

RESOURCE AVAILABILITY

Lead contact

Further information and requests for resources and reagents should be directed to and will be fulfilled by the lead contact, Ilya Levental (il2sy@virginia.edu).

Materials availability

No reagents were generated specifically for this study.

Data and code availability

Some simulation trajectories have been uploaded to publicly accessible archives: Zenodo: https://doi.org/10.5281/zenodo.14626487 and https://doi.org/10.5281/zenodo.14748699. All other data and code used for analysis will be provided upon request.

ACKNOWLEDGMENTS

We thank Madhusmita Tripathy and Anand Srivastava for providing their code for calculating packing defects in three dimensions and Anne Kenworthy, Robert Ernst, and Itay Budin for critical reading of the manuscript. M.D. acknowledges support by NIH F32GM134704 and the SciLifeLab & Wallenberg Data Driven Life Science Program (grant KAW 2024.0159). J.S. is funded by the Marie Skłodowska-Curie Actions Postdoctoral Fellowship (grant 101059180). E.S. is funded by Karolinska Institutet, SciLifeLab, Swedish Research Council Starting Grant 2020-02682, and the Human Frontiers Science Program (grant RGP0025/2022). F.A.H. is supported by NIH/NIGMS R01GM138887. E.L. was supported by R01 GM120351. J.L.S. was supported by GM008280. K.R.L. and I.L. are supported by NIH (GM120351 and GM134949), the Volkswagen Foundation (grant 93091), and the Human Frontiers Science Program (RGP0059/2019).

AUTHOR CONTRIBUTIONS

Conceptualization, M.D., K.R.L., and I.L.; methodology, M.D., J.L.S., K.R.L., J.H.L., E.L., F.A.H., and E.S.; investigation, M.D., J.L.S., X.Z., H.-Y.W., J.S., and K.R.L.; visualization, M.D., K.R.L., I.L., and J.L.S.; formal analysis, M.D., K.R.L., J.L.S., and J.S.; resources, E.L. and E.S.; data curation, M.D. and K.R.L.; funding acquisition, M.D., J.S., E.S., F.A.H., E.L., and I.L.; supervision, E.S., E.L., F.A.H., K.R.L., and I.L.; writing – original draft, M.D., K.R.L., and I.L.; writing – review and editing, M.D., J.L.S., X.Z., H.-Y.W., J.S., J.H.L., F.A.H., E.S., E.L., K.R.L., and I.L.

DECLARATION OF INTERESTS

The authors declare no competing interests.

STAR★METHODS

Detailed methods are provided in the online version of this paper and include the following:

SUPPLEMENTAL INFORMATION

Supplemental information can be found online at https://doi.org/10.1016/j.cell.2025.02.034.

Received: September 6, 2023
Revised: December 5, 2024
Accepted: February 27, 2025
Published: April 2, 2025

REFERENCES

1. Verkleij, A.J., Zwaal, R.F., Roelofsen, B., Comfurius, P., Kastelijn, D., and van Deenen, L.L. (1973). The asymmetric distribution of phospholipids in the human red cell membrane. A combined study using phospholipases and freeze-etch electron microscopy. Biochim. Biophys. Acta *323*, 178–193. https://doi.org/10.1016/0005-2736(73)90143-0.
2. Devaux, P.F. (1991). Static and dynamic lipid asymmetry in cell membranes. Biochemistry *30*, 1163–1173. https://doi.org/10.1021/bi00219a001.
3. Bretscher, M.S. (1972). Asymmetrical lipid bilayer structure for biological membranes. Nat. New Biol. *236*, 11–12. https://doi.org/10.1038/newbio236011a0.
4. Nagata, S., Sakuragi, T., and Segawa, K. (2020). Flippase and scramblase for phosphatidylserine exposure. Curr. Opin. Immunol. *62*, 31–38. https://doi.org/10.1016/j.coi.2019.11.009.
5. Sakuragi, T., and Nagata, S. (2023). Regulation of phospholipid distribution in the lipid bilayer by flippases and scramblases. Nat. Rev. Mol. Cell Biol. *24*, 576–596. https://doi.org/10.1038/s41580-023-00604-z.
6. Lorent, J.H., Levental, K.R., Ganesan, L., Rivera-Longsworth, G., Sezgin, E., Doktorova, M., Lyman, E., and Levental, I. (2020). Plasma membranes are asymmetric in lipid unsaturation, packing and protein shape. Nat. Chem. Biol. *16*, 644–652. https://doi.org/10.1038/s41589-020-0529-6.
7. Steck, T.L., and Lange, Y. (2018). Transverse distribution of plasma membrane bilayer cholesterol: picking sides. Traffic *19*, 750–760. https://doi.org/10.1111/tra.12586.
8. van den Eijnde, S.M., van den Hoff, M.J., Reutelingsperger, C.P., van Heerde, W.L., Henfling, M.E., Vermeij-Keers, C., Schutte, B., Borgers, M., and Ramaekers, F.C. (2001). Transient expression of phosphatidylserine at cell-cell contact areas is required for myotube formation. J. Cell Sci. *114*, 3631–3642. https://doi.org/10.1242/jcs.114.20.3631.
9. Mercer, J., and Helenius, A. (2008). Vaccinia virus uses macropinocytosis and apoptotic mimicry to enter host cells. Science *320*, 531–535. https://doi.org/10.1126/science.1155164.
10. Elliott, J.I., Surprenant, A., Marelli-Berg, F.M., Cooper, J.C., Cassady-Cain, R.L., Wooding, C., Linton, K., Alexander, D.R., and Higgins, C.F. (2005). Membrane phosphatidylserine distribution as a non-apoptotic signalling mechanism in lymphocytes. Nat. Cell Biol. *7*, 808–816. https://doi.org/10.1038/ncb1279.
11. Doktorova, M., Symons, J.L., and Levental, I. (2020). Structural and functional consequences of reversible lipid asymmetry in living membranes. Nat. Chem. Biol. *16*, 1321–1330. https://doi.org/10.1038/s41589-020-00688-0.
12. Bevers, E.M., and Williamson, P.L. (2016). Getting to the outer leaflet: physiology of phosphatidylserine exposure at the plasma membrane. Physiol. Rev. *96*, 605–645. https://doi.org/10.1152/physrev.00020.2015.

13. Zwaal, R.F., Roelofsen, B., Comfurius, P., and van Deenen, L.L. (1975). Organization of phospholipids in human red cell membranes as detected by the action of various purified phospholipases. Biochim. Biophys. Acta *406*, 83–96. https://doi.org/10.1016/0005-2736(75)90044-9.

14. Renooij, W., Van Golde, L.M., Zwaal, R.F., Roelofsen, B., and Van Deenen, L.L. (1974). Preferential incorporation of fatty acids at the inside of human erythrocyte membranes. Biochim. Biophys. Acta *363*, 287–292. https://doi.org/10.1016/0005-2736(74)90069-8.

15. Rawyler, A., van der Schaft, P.H., Roelofsen, B., and Op den Kamp, J.A. (1985). Phospholipid localization in the plasma membrane of Friend erythroleukemic cells and mouse erythrocytes. Biochemistry *24*, 1777–1783. https://doi.org/10.1021/bi00328a031.

16. Van der Schaft, P.H., Roelofsen, B., Op den Kamp, J.A., and Van Deenen, L.L. (1987). Phospholipid asymmetry during erythropoiesis. A study on Friend erythroleukemic cells and mouse reticulocytes. Biochim. Biophys. Acta *900*, 103–115. https://doi.org/10.1016/0005-2736(87)90282-3.

17. Lange, Y., Dolde, J., and Steck, T.L. (1981). The rate of transmembrane movement of cholesterol in the human erythrocyte. J. Biol. Chem. *256*, 5321–5323. https://doi.org/10.1016/S0021-9258(19)69200-8.

18. Bruckner, R.J., Mansy, S.S., Ricardo, A., Mahadevan, L., and Szostak, J.W. (2009). Flip-flop-induced relaxation of bending energy: implications for membrane remodeling. Biophys. J. *97*, 3113–3122. https://doi.org/10.1016/j.bpj.2009.09.025.

19. Huang, Z., and London, E. (2013). Effect of cyclodextrin and membrane lipid structure upon cyclodextrin-lipid interaction. Langmuir *29*, 14631–14638. https://doi.org/10.1021/la4031427.

20. Zidovetzki, R., and Levitan, I. (2007). Use of cyclodextrins to manipulate plasma membrane cholesterol content: evidence, misconceptions and control strategies. Biochim. Biophys. Acta *1768*, 1311–1324. https://doi.org/10.1016/j.bbamem.2007.03.026.

21. McGraw, C., Yang, L., Levental, I., Lyman, E., and Robinson, A.S. (2019). Membrane cholesterol depletion reduces downstream signaling activity of the adenosine A2a receptor. Biochim. Biophys. Acta Biomembr. *1861*, 760–767. https://doi.org/10.1016/j.bbamem.2019.01.001.

22. Arashiki, N., Saito, M., Koshino, I., Kamata, K., Hale, J., Mohandas, N., Manno, S., and Takakuwa, Y. (2016). An Unrecognized Function of Cholesterol: Regulating the Mechanism Controlling Membrane Phospholipid Asymmetry. Biochemistry *55*, 3504–3513. https://doi.org/10.1021/acs.biochem.6b00407.

23. Miettinen, M.S., and Lipowsky, R. (2019). Bilayer Membranes with Frequent Flip-Flops Have Tensionless Leaflets. Nano Lett. *19*, 5011–5016. https://doi.org/10.1021/acs.nanolett.9b01239.

24. Almeida, P.F.F. (2009). Thermodynamics of lipid interactions in complex bilayers. Biochim. Biophys. Acta *1788*, 72–85. https://doi.org/10.1016/j.bbamem.2008.08.007.

25. Varma, M., and Deserno, M. (2022). Distribution of cholesterol in asymmetric membranes driven by composition and differential stress. Biophys. J. *121*, 4001–4018. https://doi.org/10.1016/j.bpj.2022.07.032.

26. Hossein, A., and Deserno, M. (2020). Spontaneous Curvature, Differential Stress, and Bending Modulus of Asymmetric Lipid Membranes. Biophys. J. *118*, 624–642. https://doi.org/10.1016/j.bpj.2019.11.3398.

27. Allender, D.W., Sodt, A.J., and Schick, M. (2019). Cholesterol-Dependent Bending Energy Is Important in Cholesterol Distribution of the Plasma Membrane. Biophys. J. *116*, 2356–2366. https://doi.org/10.1016/j.bpj.2019.03.028.

28. McIntosh, A.L., Atshaves, B.P., Huang, H., Gallegos, A.M., Kier, A.B., and Schroeder, F. (2008). Fluorescence techniques using dehydroergosterol to study cholesterol trafficking. Lipids *43*, 1185–1208. https://doi.org/10.1007/s11745-008-3194-1.

29. Pourmousa, M., Róg, T., Mikkeli, R., Vattulainen, L., Solanko, L.M., Wüstner, D., List, N.H., Kongsted, J., and Karttunen, M. (2014). Dehydroergosterol as an analogue for cholesterol: why it mimics cholesterol so well-or does it? J. Phys. Chem. B *118*, 7345–7357. https://doi.org/10.1021/jp406883k.

30. Wesseling, M.C., Wagner-Britz, L., Nguyen, D.B., Asanidze, S., Mutua, J., Mohamed, N., Hanf, B., Ghashghaeinia, M., Kaestner, L., and Bernhardt, I. (2016). Novel Insights in the Regulation of Phosphatidylserine Exposure in Human Red Blood Cells. Cell. Physiol. Biochem. *39*, 1941–1954. https://doi.org/10.1159/000447891.

31. Pinkwart, K., Schneider, F., Lukoseviciute, M., Sauka-Spengler, T., Lyman, E., Eggeling, C., and Sezgin, E. (2019). Nanoscale dynamics of cholesterol in the cell membrane. J. Biol. Chem. *294*, 12599–12609. https://doi.org/10.1074/jbc.RA119.009683.

32. Sezgin, E., Levental, I., Grzybek, M., Schwarzmann, G., Mueller, V., Honigmann, A., Belov, V.N., Eggeling, C., Coskun, U., Simons, K., et al. (2012). Partitioning, diffusion, and ligand binding of raft lipid analogs in model and cellular plasma membranes. Biochim. Biophys. Acta *1818*, 1777–1784. https://doi.org/10.1016/j.bbamem.2012.03.007.

33. Hölttä-Vuori, M., Uronen, R.L., Repakova, J., Salonen, E., Vattulainen, I., Panula, P., Li, Z., Bittman, R., and Ikonen, E. (2008). BODIPY-cholesterol: a new tool to visualize sterol trafficking in living cells and organisms. Traffic *9*, 1839–1849. https://doi.org/10.1111/j.1600-0854.2008.00801.x.

34. Wüstner, D., Lund, F.W., Röhrl, C., and Stangl, H. (2016). Potential of BODIPY-cholesterol for analysis of cholesterol transport and diffusion in living cells. Chem. Phys. Lipids *194*, 12–28. https://doi.org/10.1016/j.chemphyslip.2015.08.007.

35. Javanainen, M., and Martinez-Seara, H. (2019). Rapid diffusion of cholesterol along polyunsaturated membranes via deep dives. Phys. Chem. Chem. Phys. *21*, 11660–11669. https://doi.org/10.1039/c9cp02022e.

36. Doktorova, M., and Levental, I. (2022). Cholesterol's balancing act: Defying the status quo. Biophys. J. *121*, 3771–3773. https://doi.org/10.1016/j.bpj.2022.08.036.

37. Levental, K.R., Malmberg, E., Symons, J.L., Fan, Y.Y., Chapkin, R.S., Ernst, R., and Levental, I. (2020). Lipidomic and biophysical homeostasis of mammalian membranes counteracts dietary lipid perturbations to maintain cellular fitness. Nat. Commun. *11*, 1339. https://doi.org/10.1038/s41467-020-15203-1.

38. Larsen, J.B., Jensen, M.B., Bhatia, V.K., Pedersen, S.L., Bjørnholm, T., Iversen, L., Uline, M., Szleifer, I., Jensen, K.J., Hatzakis, N.S., et al. (2015). Membrane curvature enables N-Ras lipid anchor sorting to liquid-ordered membrane phases. Nat. Chem. Biol. *11*, 192–194. https://doi.org/10.1038/nchembio.1733.

39. Cui, H., Lyman, E., and Voth, G.A. (2011). Mechanism of membrane curvature sensing by amphipathic helix containing proteins. Biophys. J. *100*, 1271–1279. https://doi.org/10.1016/j.bpj.2011.01.036.

40. Vanni, S., Vamparys, L., Gautier, R., Drin, G., Etchebest, C., Fuchs, P.F.J., and Antonny, B. (2013). Amphipathic lipid packing sensor motifs: probing bilayer defects with hydrophobic residues. Biophys. J. *104*, 575–584. https://doi.org/10.1016/j.bpj.2012.11.3837.

41. Yeung, T., Gilbert, G.E., Shi, J., Silvius, J., Kapus, A., and Grinstein, S. (2008). Membrane phosphatidylserine regulates surface charge and protein localization. Science *319*, 210–213. https://doi.org/10.1126/science.1152066.

42. Koh, D.H.Z., Naito, T., Na, M., Yeap, Y.J., Rozario, P., Zhong, F.L., Lim, K.L., and Saheki, Y. (2023). Visualization of accessible cholesterol using a GRAM domain-based biosensor. Nat. Commun. *14*, 6773. https://doi.org/10.1038/s41467-023-42498-7.

43. Das, A., Brown, M.S., Anderson, D.D., Goldstein, J.L., and Radhakrishnan, A. (2014). Three pools of plasma membrane cholesterol and their relation to cholesterol homeostasis. eLife *3*, e02882. https://doi.org/10.7554/eLife.02882.

44. Reagle, T., Xie, Y., Li, Z., Carnero, W., and Baumgart, T. (2024). Methyl-beta-cyclodextrin asymmetrically extracts phospholipid from bilayers, granting tunable control over differential stress in lipid vesicles. Soft Matter *20*, 4291–4307. https://doi.org/10.1039/d3sm01772a.

45. Bettache, N., Baisamy, L., Baghdiguian, S., Payrastre, B., Mangeat, P., and Bienvenue, A. (2003). Mechanical constraint imposed on plasma membrane through transverse phospholipid imbalance induces reversible actin polymerization via phosphoinositide 3-kinase activation. J. Cell Sci. *116*, 2277–2284. https://doi.org/10.1242/jcs.00424.

46. Sandhu, J., Li, S., Fairall, L., Pfisterer, S.G., Gurnett, J.E., Xiao, X., Weston, T.A., Vashi, D., Ferrari, A., Orozco, J.L., et al. (2018). Aster Proteins Facilitate Nonvesicular Plasma Membrane to ER Cholesterol Transport in Mammalian Cells. Cell *175*, 514–529.e20. https://doi.org/10.1016/j.cell.2018.08.033.

47. Naito, T., Ercan, B., Krshnan, L., Triebl, A., Koh, D.H.Z., Wei, F.Y., Tomizawa, K., Torta, F.T., Wenk, M.R., and Saheki, Y. (2019). Movement of accessible plasma membrane cholesterol by the GRAMD1 lipid transfer protein complex. eLife *8*, e51401. https://doi.org/10.7554/eLife.51401.

48. Besprozvannaya, M., Dickson, E., Li, H., Ginburg, K.S., Bers, D.M., Auwerx, J., and Nunnari, J. (2018). GRAM domain proteins specialize functionally distinct ER-PM contact sites in human cells. eLife *7*, e31019. https://doi.org/10.7554/eLife.31019.

49. Ventura, A.E., Pokorna, S., Huhn, N., Santos, T.C.B., Prieto, M., Futerman, A.H., and Silva, L.C. (2023). Cell lipid droplet heterogeneity and altered biophysical properties induced by cell stress and metabolic imbalance. Biochim. Biophys. Acta Mol. Cell Biol. Lipids *1868*, 159347. https://doi.org/10.1016/j.bbalip.2023.159347.

50. Chang, T.Y., Chang, C.C.Y., Ohgami, N., and Yamauchi, Y. (2006). Cholesterol sensing, trafficking, and esterification. Annu. Rev. Cell Dev. Biol. *22*, 129–157. https://doi.org/10.1146/annurev.cellbio.22.010305.104656.

51. Foley, S.L., Varma, M., Hossein, A., and Deserno, M. (2023). Elastic and thermodynamic consequences of lipid membrane asymmetry. Emerg. Top. Life Sci. *7*, 95–110. https://doi.org/10.1042/ETLS20220084.

52. Liu, S.L., Sheng, R., Jung, J.H., Wang, L., Stec, E., O'Connor, M.J., Song, S., Bikkavilli, R.K., Winn, R.A., Lee, D., et al. (2017). Orthogonal lipid sensors identify transbilayer asymmetry of plasma membrane cholesterol. Nat. Chem. Biol. *13*, 268–274. https://doi.org/10.1038/nchembio.2268.

53. Tao, X., Zhao, C., and MacKinnon, R. (2023). Membrane protein isolation and structure determination in cell-derived membrane vesicles. Proc. Natl. Acad. Sci. USA *120*, e2302325120. https://doi.org/10.1073/pnas.2302325120.

54. Coupland, C.E., Karimi, R., Bueler, S.A., Liang, Y., Courbon, G.M., Di Trani, J.M., Wong, C.J., Saghian, R., Youn, J.Y., Wang, L.Y., et al. (2024). High-resolution electron cryomicroscopy of V-ATPase in native synaptic vesicles. Science *385*, 168–174. https://doi.org/10.1126/science.adp5577.

55. Simons, K., and Gruenberg, J. (2000). Jamming the endosomal system: lipid rafts and lysosomal storage diseases. Trends Cell Biol. *10*, 459–462. https://doi.org/10.1016/s0962-8924(00)01847-x.

56. Pekkinen, M., Terhal, P.A., Botto, L.D., Henning, P., Mäkitie, R.E., Roschger, P., Jain, A., Kol, M., Kjellberg, M.A., Paschalis, E.P., et al. (2019). Osteoporosis and skeletal dysplasia caused by pathogenic variants in SGMS2. JCI Insight *4*, e126180. https://doi.org/10.1172/jci.insight.126180.

57. Ferrari, A., Whang, E., Xiao, X., Kennelly, J.P., Romartinez-Alonso, B., Mack, J.J., Weston, T., Chen, K., Kim, Y., Tol, M.J., et al. (2023). Aster-dependent nonvesicular transport facilitates dietary cholesterol uptake. Science *382*, eadf0966. https://doi.org/10.1126/science.adf0966.

58. Cortés, V., and Eckel, R.H. (2022). Insulin and Bile Acids in Cholesterol Homeostasis: New Players in Diabetes-Associated Atherosclerosis. Circulation *145*, 983–986. https://doi.org/10.1161/CIRCULATIONAHA.122.058883.

59. Xiao, X., Kennelly, J.P., Ferrari, A., Clifford, B.L., Whang, E., Gao, Y., Qian, K., Sandhu, J., Jarrett, K.E., Brearley-Sholto, M.C., et al. (2023). Hepatic nonvesicular cholesterol transport is critical for systemic lipid homeostasis. Nat. Metab. *5*, 165–181. https://doi.org/10.1038/s42255-022-00722-6.

60. Bigay, J., and Antonny, B. (2012). Curvature, lipid packing, and electrostatics of membrane organelles: defining cellular territories in determining specificity. Dev. Cell *23*, 886–895. https://doi.org/10.1016/j.devcel.2012.10.009.

61. Schindelin, J., Arganda-Carreras, I., Frise, E., Kaynig, V., Longair, M., Pietzsch, T., Preibisch, S., Rueden, C., Saalfeld, S., Schmid, B., et al. (2012). Fiji: an open-source platform for biological-image analysis. Nat. Methods *9*, 676–682. https://doi.org/10.1038/nmeth.2019.

62. Phillips, J.C., Hardy, D.J., Maia, J.D.C., Stone, J.E., Ribeiro, J.V., Bernardi, R.C., Buch, R., Fiorin, G., Hénin, J., Jiang, W., et al. (2020). Scalable molecular dynamics on CPU and GPU architectures with NAMD. J. Chem. Phys. *153*, 044130. https://doi.org/10.1063/5.0014475.

63. Abraham, M.J., Murtola, T., Schulz, R., Páll, S., Smith, J.C., Hess, B., and Lindahl, E. (2015). GROMACS: high performance molecular simulations through multi-level parallelism from laptops to supercomputers. SoftwareX *1–2*, 19–25. https://doi.org/10.1016/j.softx.2015.06.001.

64. Humphrey, W., Dalke, A., and Schulten, K. (1996). VMD: visual molecular dynamics. J. Mol. Graph. *14*, 33–38. https://doi.org/10.1016/0263-7855(96)00018-5.

65. Gautier, R., Bacle, A., Tiberti, M.L., Fuchs, P.F., Vanni, S., and Antonny, B. (2018). PackMem: A Versatile Tool to Compute and Visualize Interfacial Packing Defects in Lipid Bilayers. Biophys. J. *115*, 436–444. https://doi.org/10.1016/j.bpj.2018.06.025.

66. Guixà-González, R., Rodriguez-Espigares, I., Ramírez-Anguita, J.M., Carrió-Gaspar, P., Martinez-Seara, H., Giorgino, T., and Selent, J. (2014). MEMBPLUGIN: studying membrane complexity in VMD. Bioinformatics *30*, 1478–1480. https://doi.org/10.1093/bioinformatics/btu037.

67. Lee, J., Patel, D.S., Ståhle, J., Park, S.J., Kern, N.R., Kim, S., Lee, J., Cheng, X., Valvano, M.A., Holst, O., et al. (2019). CHARMM-GUI Membrane Builder for Complex Biological Membrane Simulations with Glycolipids and Lipoglycans. J. Chem. Theor. Comput. *15*, 775–786. https://doi.org/10.1021/acs.jctc.8b01066.

68. Surma, M.A., Gerl, M.J., Herzog, R., Helppi, J., Simons, K., and Klose, C. (2021). Mouse lipidomics reveals inherent flexibility of a mammalian lipidome. Sci. Rep. *11*, 19364. https://doi.org/10.1038/s41598-021-98702-5.

69. Ejsing, C.S., Sampaio, J.L., Surendranath, V., Duchoslav, E., Ekroos, K., Klemm, R.W., Simons, K., and Shevchenko, A. (2009). Global analysis of the yeast lipidome by quantitative shotgun mass spectrometry. Proc. Natl. Acad. Sci. USA *106*, 2136–2141. https://doi.org/10.1073/pnas.0811700106.

70. Porter, M.J., Zhang, G.L., and Schnaar, R.L. (2021). Ganglioside extraction, purification and profiling. J. Vis. Exp. https://doi.org/10.3791/62385.

71. Surma, M.A., Herzog, R., Vasilj, A., Klose, C., Christinat, N., Morin-Rivron, D., Simons, K., Masoodi, M., and Sampaio, J.L. (2015). An automated shotgun lipidomics platform for high throughput, comprehensive, and quantitative analysis of blood plasma intact lipids. Eur. J. Lipid Sci. Technol. *117*, 1540–1549. https://doi.org/10.1002/ejlt.201500145.

72. Liebisch, G., Binder, M., Schifferer, R., Langmann, T., Schulz, B., and Schmitz, G. (2006). High throughput quantification of cholesterol and cholesteryl ester by electrospray ionization tandem mass spectrometry (ESI-MS/MS). Biochim. Biophys. Acta *1761*, 121–128. https://doi.org/10.1016/j.bbalip.2005.12.007.

73. Herzog, R., Schuhmann, K., Schwudke, D., Sampaio, J.L., Bornstein, S.R., Schroeder, M., and Shevchenko, A. (2012). LipidXplorer: a software for consensual cross-platform lipidomics. PLoS One *7*, e29851. https://doi.org/10.1371/journal.pone.0029851.

74. Herzog, R., Schwudke, D., Schuhmann, K., Sampaio, J.L., Bornstein, S.R., Schroeder, M., and Shevchenko, A. (2011). A novel informatics concept for high-throughput shotgun lipidomics based on the molecular fragmentation query language. Genome Biol. *12*, R8. https://doi.org/10.1186/gb-2011-12-1-r8.

75. Kuchel, P.W., Cox, C.D., Daners, D., Shishmarev, D., and Galvosas, P. (2021). Surface model of the human red blood cell simulating changes

in membrane curvature under strain. Sci. Rep. *11*, 13712. https://doi.org/10.1038/s41598-021-92699-7.

76. Dupuy, A.D., and Engelman, D.M. (2008). Protein area occupancy at the center of the red blood cell membrane. Proc. Natl. Acad. Sci. USA *105*, 2848–2852. https://doi.org/10.1073/pnas.0712379105.
77. Pasini, E.M., Kirkegaard, M., Mortensen, P., Lutz, H.U., Thomas, A.W., and Mann, M. (2006). In-depth analysis of the membrane and cytosolic proteome of red blood cells. Blood *108*, 791–801. https://doi.org/10.1182/blood-2005-11-007799.
78. Bryk, A.H., and Wiśniewski, J.R. (2017). Quantitative Analysis of Human Red Blood Cell Proteome. J. Proteome Res. *16*, 2752–2761. https://doi.org/10.1021/acs.jproteome.7b00025.
79. Ravenhill, B.J., Kanjee, U., Ahouidi, A., Nobre, L., Williamson, J., Goldberg, J.M., Antrobus, R., Dieye, T., Duraisingh, M.T., and Weekes, M.P. (2019). Quantitative comparative analysis of human erythrocyte surface proteins between individuals from two genetically distinct populations. Commun. Biol. *2*, 350. https://doi.org/10.1038/s42003-019-0596-y.
80. Kooyman, D.L., Byrne, G.W., McClellan, S., Nielsen, D., Tone, M., Waldmann, H., Coffman, T.M., McCurry, K.R., Platt, J.L., and Logan, J.S. (1995). In vivo transfer of GPI-linked complement restriction factors from erythrocytes to the endothelium. Science *269*, 89–92. https://doi.org/10.1126/science.7541557.
81. Kinoshita, T., Medof, M.E., Silber, R., and Nussenzweig, V. (1985). Distribution of decay-accelerating factor in the peripheral blood of normal individuals and patients with paroxysmal nocturnal hemoglobinuria. J. Exp. Med. *162*, 75–92. https://doi.org/10.1084/jem.162.1.75.
82. Takamori, S., Holt, M., Stenius, K., Lemke, E.A., Grønborg, M., Riedel, D., Urlaub, H., Schenck, S., Brügger, B., Ringler, P., et al. (2006). Molecular anatomy of a trafficking organelle. Cell *127*, 831–846. https://doi.org/10.1016/j.cell.2006.10.030.
83. Sharpe, H.J., Stevens, T.J., and Munro, S. (2010). A comprehensive comparison of transmembrane domains reveals organelle-specific properties. Cell *142*, 158–169. https://doi.org/10.1016/j.cell.2010.05.037.
84. Mucksch, F., Citir, M., Luchtenborg, C., Glass, B., Traynor-Kaplan, A., Schultz, C., Brugger, B., and Krausslich, H.G. (2019). Quantification of phosphoinositides reveals strong enrichment of PIP(2) in HIV-1 compared to producer cell membranes. Sci. Rep. *9*, 17661. https://doi.org/10.1038/s41598-019-53939-z.
85. de Jong, D.H., Singh, G., Bennett, W.F.D., Arnarez, C., Wassenaar, T.A., Schäfer, L.V., Periole, X., Tieleman, D.P., and Marrink, S.J. (2013). Improved Parameters for the Martini Coarse-Grained Protein Force Field. J. Chem. Theor. Comput. *9*, 687–697. https://doi.org/10.1021/ct300646g.
86. Fábián, B., Thallmair, S., and Hummer, G. (2023). Optimal Bond Constraint Topology for Molecular Dynamics Simulations of Cholesterol. J. Chem. Theor. Comput. *19*, 1592–1601. https://doi.org/10.1021/acs.jctc.2c01032.
87. Thallmair, S., Javanainen, M., Fábián, B., Martinez-Seara, H., and Marrink, S.J. (2021). Nonconverged Constraints Cause Artificial Temperature Gradients in Lipid Bilayer Simulations. J. Phys. Chem. B *125*, 9537–9546. https://doi.org/10.1021/acs.jpcb.1c03665.
88. Yu, Y., Krämer, A., Venable, R.M., Brooks, B.R., Klauda, J.B., and Pastor, R.W. (2021). CHARMM36 Lipid Force Field with Explicit Treatment of Long-Range Dispersion: Parametrization and Validation for Phosphatidylethanolamine, Phosphatidylglycerol, and Ether Lipids. J. Chem. Theor. Comput. *17*, 1581–1595. https://doi.org/10.1021/acs.jctc.0c01327.
89. Doktorova, M., and Weinstein, H. (2018). Accurate in silico modeling of asymmetric bilayers based on biophysical principles. Biophys. J. *115*, 1638–1643. https://doi.org/10.1016/j.bpj.2018.09.008.
90. Tripathy, M., Thangamani, S., and Srivastava, A. (2020). Three-Dimensional Packing Defects in Lipid Membrane as a Function of Membrane Order. J. Chem. Theor. Comput. *16*, 7800–7816. https://doi.org/10.1021/acs.jctc.0c00609.
91. Chakraborty, S., Doktorova, M., Molugu, T.R., Heberle, F.A., Scott, H.L., Dzikovski, B., Nagao, M., Stingaciu, L.R., Standaert, R.F., Barrera, F.N., et al. (2020). How cholesterol stiffens unsaturated lipid membranes. Proc. Natl. Acad. Sci. USA *117*, 21896–21905. https://doi.org/10.1073/pnas.2004807117.
92. Doktorova, M., Heberle, F.A., Eicher, B., Standaert, R.F., Katsaras, J., London, E., Pabst, G., and Marquardt, D. (2018). Preparation of asymmetric phospholipid vesicles for use as cell membrane models. Nat. Protoc. *13*, 2086–2101. https://doi.org/10.1038/s41596-018-0033-6.
93. Buboltz, J.T., and Feigenson, G.W. (1999). A novel strategy for the preparation of liposomes: rapid solvent exchange. Biochim. Biophys. Acta *1417*, 232–245. https://doi.org/10.1016/s0005-2736(99)00006-1.
94. McIntosh, A.L., Gallegos, A.M., Atshaves, B.P., Storey, S.M., Kannoju, D., and Schroeder, F. (2003). Fluorescence and multiphoton imaging resolve unique structural forms of sterol in membranes of living cells. J. Biol. Chem. *278*, 6384–6403. https://doi.org/10.1074/jbc.M205472200.
95. Lakowicz, J.R. (2006). Principles of Fluorescence Spectroscopy (Springer).
96. Schroeder, F., Barenholz, Y., Gratton, E., and Thompson, T.E. (1987). A fluorescence study of dehydroergosterol in phosphatidylcholine bilayer vesicles. Biochemistry *26*, 2441–2448. https://doi.org/10.1021/bi00383a007.
97. Waithe, D., Clausen, M.P., Sezgin, E., and Eggeling, C. (2016). FoCuSpoint: software for STED fluorescence correlation and time-gated single photon counting. Bioinformatics *32*, 958–960. https://doi.org/10.1093/bioinformatics/btv687.
98. Jaiswal, A., Hoerth, C.H., Zúñiga Pereira, A.M., and Lorenz, H. (2019). Improved spatial resolution by induced live cell and organelle swelling in hypotonic solutions. Sci. Rep. *9*, 12911. https://doi.org/10.1038/s41598-019-49408-2.
99. Diaz-Rohrer, B.B., Levental, K.R., Simons, K., and Levental, I. (2014). Membrane raft association is a determinant of plasma membrane localization. Proc. Natl. Acad. Sci. USA *111*, 8500–8505. https://doi.org/10.1073/pnas.1404582111.
100. Sezgin, E., Sadowski, T., and Simons, K. (2014). Measuring lipid packing of model and cellular membranes with environment sensitive probes. Langmuir *30*, 8160–8166. https://doi.org/10.1021/la501226v.
101. Owen, D.M., Rentero, C., Magenau, A., Abu-Siniyeh, A., and Gaus, K. (2011). Quantitative imaging of membrane lipid order in cells and organisms. Nat. Protoc. *7*, 24–35. https://doi.org/10.1038/nprot.2011.419.
102. Sezgin, E., Waithe, D., Bernardino de la Serna, J., and Eggeling, C. (2015). Spectral Imaging to measure heterogeneity in membrane lipid packing. ChemPhysChem *16*, 1387–1394. https://doi.org/10.1002/cphc.201402794.
103. Steck, T.L., Ye, J., and Lange, Y. (2002). Probing red cell membrane cholesterol movement with cyclodextrin. Biophys. J. *83*, 2118–2125. https://doi.org/10.1016/S0006-3495(02)73972-6.
104. Steck, T.L., and Lange, Y. (2012). How slow is the transbilayer diffusion (flip-flop) of cholesterol?author reply 947. Biophys. J. *102*, 945–946. https://doi.org/10.1016/j.bpj.2011.10.059.
105. Bennett, W.F.D., MacCallum, J.L., Hinner, M.J., Marrink, S.J., and Tieleman, D.P. (2009). Molecular view of cholesterol flip-flop and chemical potential in different membrane environments. J. Am. Chem. Soc. *131*, 12714–12720. https://doi.org/10.1021/ja903529f.
106. Fisher, K.A. (1976). Analysis of membrane halves: cholesterol. Proc. Natl. Acad. Sci. USA *73*, 173–177. https://doi.org/10.1073/pnas.73.1.173.
107. Schroeder, F., Nemecz, G., Wood, W.G., Joiner, C., Morrot, G., Ayraut-Jarrier, M., and Devaux, P.F. (1991). Transmembrane distribution of sterol in the human erythrocyte. Biochim. Biophys. Acta *1066*, 183–192. https://doi.org/10.1016/0005-2736(91)90185-b.
108. Mondal, M., Mesmin, B., Mukherjee, S., and Maxfield, F.R. (2009). Sterols are mainly in the cytoplasmic leaflet of the plasma membrane and the endocytic recycling compartment in CHO cells. Mol. Biol. Cell *20*, 581–588. https://doi.org/10.1091/mbc.E08-07-0785.

109. Solanko, L.M., Sullivan, D.P., Sere, Y.Y., Szomek, M., Lunding, A., Solanko, K.A., Pizovic, A., Stanchev, L.D., Pomorski, T.G., Menon, A.K., et al. (2018). Ergosterol is mainly located in the cytoplasmic leaflet of the yeast plasma membrane. Traffic *19*, 198–214. https://doi.org/10.1111/tra.12545.

110. Igbavboa, U., Avdulov, N.A., Schroeder, F., and Wood, W.G. (1996). Increasing age alters transbilayer fluidity and cholesterol asymmetry in synaptic plasma membranes of mice. J. Neurochem. *66*, 1717–1725. https://doi.org/10.1046/j.1471-4159.1996.66041717.x.

111. Hale, J.E., and Schroeder, F. (1982). Asymmetric transbilayer distribution of sterol across plasma membranes determined by fluorescence quenching of dehydroergosterol. Eur. J. Biochem. *122*, 649–661. https://doi.org/10.1111/j.1432-1033.1982.tb06488.x.

112. Ingólfsson, H.I., Melo, M.N., van Eerden, F.J., Arnarez, C., Lopez, C.A., Wassenaar, T.A., Periole, X., de Vries, A.H., Tieleman, D.P., and Marrink, S.J. (2014). Lipid organization of the plasma membrane. J. Am. Chem. Soc. *136*, 14554–14559. https://doi.org/10.1021/ja507832e.

113. Bittman, R., and Rottem, S. (1976). Distribution of cholesterol between the outer and inner halves of the lipid bilayer of mycoplasma cell membranes. Biochem. Biophys. Res. Commun. *71*, 318–324. https://doi.org/10.1016/0006-291x(76)90285-0.

114. Lange, Y., and Slayton, J.M. (1982). Interaction of cholesterol and lysophosphatidylcholine in determining red cell shape. J. Lipid Res. *23*, 1121–1127. https://doi.org/10.1016/S0022-2275(20)38048-2.

115. Courtney, K.C., Pezeshkian, W., Raghupathy, R., Zhang, C., Darbyson, A., Ipsen, J.H., Ford, D.A., Khandelia, H., Presley, J.F., and Zha, X. (2018). C24 Sphingolipids Govern the Transbilayer Asymmetry of Cholesterol and Lateral Organization of Model and Live-Cell Plasma Membranes. Cell Rep. *24*, 1037–1049. https://doi.org/10.1016/j.celrep.2018.06.104.

STAR★METHODS

KEY RESOURCES TABLE

REAGENT or RESOURCE	SOURCE	IDENTIFIER
Biological samples		
isolated human erythrocytes	isolated in-house from deidentified, informed healthy donors	N/A
Chemicals, peptides, and recombinant proteins		
Fluorescein isothiocyanate–dextran (MW ~3000 Da)	Sigma Aldrich	FD4
Rhodamine-dextran (MW ~3000 Da)	Sigma Aldrich	T1037
AnnexinV-AlexaFluor488	ThermoFisher Scientific	A13201
AnnexinV-AlexaFluor647	ThermoFisher Scientific	A23204
propidium iodide	ThermoFisher Scientific	P3566
Hexakis-(2,3,6-tri-O-methyl)-alpha-Cyclodextrin	Cyclodextrin-Shop	CDexA-032
Hydroxypropyl-alpha-cyclodextrin	Sigma Aldrich	390690
methyl-beta-cyclodextrin	Sigma Aldrich	C4555
dehydroergosterol	Cayman Chemical	19709
Di-4-ANEPPDHQ	Invitrogen	D36802
TopFluor-sphingomyelin	Avanti	810265
TopFluor-cholesterol	Avanti	810255
fluorescein diacetate	Cayman Chemical	35701
Sphingomyelinase from Bacillus cereus, lyophilized powder, ≥100 units/mg protein	Sigma Aldrich	S7651
myriocin	Cayman Chemical	63150
C-laurdan	SFC Ltd / TPProbes	N/A
bodipy 493/503	Cayman Chemical	25892
A23187	Cayman Chemical	11016
Phorbol 12-myristate 13-acetate	Cayman Chemical	10008014
Sandoz 58-035	Santa Cruz Biotechnology	sc-215839
18:1 (Δ9-Cis) PC (DOPC)	Avanti	850375P
Critical commercial assays		
Amplex Red Cholesterol Assay Kit	ThermoFisher Scientific	A12216
Experimental models: Cell lines		
RBL-2H3 cell line (rat basophilic leukemia)	ATCC	CRL-2256
NIH-3T3 cell line (mouse embryonic fibroblast)	ATCC	CRL-1658
Recombinant DNA		
EGFP-GRAM-H	Yasunori Saheki	N/A
EGFP-GRAMD1A	Yasunori Saheki	N/A
EGFP-GRAMD1B	Yasunori Saheki	N/A
SH4-GFP	Sarah Veatch	N/A
tH-mEmerald	John Hancock	N/A
Software and algorithms		
Fiji: an open-source platform for biological-image analysis	Schindelin et al.[61]	https://imagej.net/software/fiji/downloads
Nanoscale Molecular Dynamics (NAMD)	Phillips et al.[62]	https://www.ks.uiuc.edu/Research/namd/
Gromacs	Abraham et al.[63]	https://www.gromacs.org/

(*Continued on next page*)

Continued

REAGENT or RESOURCE	SOURCE	IDENTIFIER
MATLAB	The MathWorks Inc. (2022). MATLAB version 23.2.0.2485118 (R2023b) Update 6, Natick, Massachusetts: The MathWorks Inc.	https://www.mathworks.com
Visual Molecular Dynamics (VMD)	Humphrey et al.[64]	https://www.ks.uiuc.edu/Development/Download/download.cgi?PackageName=VMD
PackMem	Gautier et al.[65]	https://packmem.ipmc.cnrs.fr/
MEMBPLUGIN	Guixà-González et al.[66]	https://sourceforge.net/p/membplugin/wiki/Home/
CHARMM-GUI	Lee et al.[67]	https://www.charmm-gui.org/

EXPERIMENTAL MODEL AND STUDY PARTICIPANT DETAILS

Cell culture

RBL-2H3 cells were purchased from ATCC and grown in Eagle's Minimum Essential Medium (EMEM) media (Gibco) with 10% fetal bovine serum (FBS, Genessee) and 1% penicillin-streptomycin (Gibco). NIH-3T3 cells were grown in Dulbecco's Modified Eagle Medium (DMEM) supplemented with 10% FBS and 1% penicillin-streptomycin (Gibco). In all microscopy experiments, confluent cells at passage between 10 and 16 were split the day before imaging in glass-bottom plates at a 1:4 dilution.

METHOD DETAILS

Lipidomics

Human erythrocytes (freshly isolated and intact) were treated with two enzymes, phospholipase 2 (PLA2) and sphingomyelinase (SMase) to digest exclusively the lipid species on the exoplasmic PM leaflet. Enzyme-treated cells were compared to untreated controls to determine the abundance of ~600 unique phospholipid species on the exoplasmic leaflet via the extent of digestion. The analysis included all major phospholipid species in erythrocytes together with glycosphingolipids (GSLs). Hemolysis was monitored to ensure that the integrity of the erythrocytes was preserved, and enzyme treatment of sonically disrupted cells verified the optimality of experimental conditions (i.e., the enzymes successfully degraded all available target lipids). Additional controls including lack of spontaneous phospholipid flipping on the experimental timescales can be found in Lorent et al.[6]

The lipidome of the inner leaflet was inferred from the lipid species remaining after digestion of intact cells, while the outer leaflet was calculated by subtracting the abundance of each lipid species remaining after digestion from the untreated controls for each target of the enzyme used. These data were highly consistent between multiple healthy adult donors (N = 3) and repeated samples from the same donor. These measurements produced raw lipidomes of the inner and outer leaflets. The total lipid amounts per leaflet were determined by adding the mol% of each individual species and averaging across experiments (n > 3).

Quantitative accuracy of these approaches is supported by the fact that the products of the lipolysis reactions (lysolipids and ceramide) are quantitatively equivalent to the abundances of the parent lipids (PL and SM) consumed by the reaction (see supplement of Lorent et al.[6]).

Lipid names and abbreviations used in the study include: 1-palmitoyl-2-oleoyl-glycero-3-phosphocholine (POPC), 1-palmitoyl-2-oleoyl-sn-glycero-3-phospho-L-serine (POPS), 1,2-dipalmitoyl-sn-glycero-3-phosphocholine (DPPC), 1,2-diarachidonoyl-sn-glycero-3-phosphocholine (DAPC), 1,2-dioleoyl-sn-glycero-3-phosphocholine (DOPC), 1,2-dioleoyl-sn-glycero-3-phospho-L-serine (DOPS), egg sphingomyelin (eSM), 1-palmitoyl-2-oleoyl-sn-glycero-3-phosphoethanolamine (POPE), 1-palmitoyl-2-oleoyl-sn-glycero-3-phospho-(1'-rac-glycerol) (POPG), N-palmitoyl-D-erythro-sphingosylphosphorylcholine (PSM), 1-palmitoyl-2-linoleoyl-sn-glycero-3-phosphocholine (PLPC), 1-palmitoyl-2-docosahexaenoyl-phosphoethanolamine (PDPE), 1-palmitoyl-2-arachidonoyl-phospho-L-serine (PAPS), N-lignoceroyl-D-erythro-sphingosylphosphorylcholine (24:0 SM, LSM), N-nervonoyl-D-erythro-sphingosylphosphorylcholine (24:1 SM, NSM), 1-palmitoyl-2-arachidonoyl-phosphocholine (PAPC), 1-stearoyl-2-oleoyl-phosphocholine (SOPC), 1-stearoyl-2-arachidonoyl-phospho-L-serine (SAPS), 1-oleoyl-2-arachidonoyl-phosphoethanolamine (OAPE), 1-oleoyl-2-arachidonoyl-phospho-L-serine (OAPS), 1-stearoyl-2-arachidonoyl-phosphoinositol (SAPI), 18:1,20:4 PE-plasmalogen (PLAS), 18:1,22:4 PE-plasmalogen (PLQS), and 18:2,20:4 PE-plasmalogen (PLAO). Structures of OAPE, OAPS, PLAO, PLAS, PLQS, and SAPI are shown in Figure S1D.

Sample preparation

Samples (300 μl) of packed, freshly isolated, intact human erythrocytes from healthy donors with informed consent were treated with 10 IU PLA2 (Apis mellifera) or 0.5 IU SMase (Bacillus cereus) in 5 ml isotonic saline solution (50 mM Tris HCl, 0.25 mM CaCl2, 0.25 mM MgCl2, 150 mM NaCl, pH 7.4) for 30 min at 30 °C to specifically digest only the lipid species present on the exoplasmic leaflet of the

PM. After treatment for the indicated time, the cells were fast-frozen in liquid nitrogen, and their detailed lipid compositions were analyzed by shotgun electron spray ionization with tandem MS-MS (ESI-MS/MS) by Lipotype and detailed below. Lipidomes were prepared from at least three independent human donors for all experiments, using the following procedures.

Lipid extraction for mass spectrometry lipidomics

Mass spectrometry-based lipid analysis was performed by Lipotype GmbH (Dresden, Germany) as described (Surma et al.[68]). Lipids were extracted using a two-step chloroform/methanol procedure.[69] Gangliosides were extracted from the water phase of the preceding chloroform/methanol extraction with a solid phase extraction protocol.[70] Samples were spiked with internal lipid standard mixture containing: cardiolipin 14:0/14:0/14:0/14:0 (CL), ceramide 18:1;2/17:0 (Cer), diacylglycerol 17:0/17:0 (DAG), hexosylceramide 18:1;2/12:0 (HexCer), dihexosylceramide 18:1;2/12:0 (DiHexCer), Globoside 3 18:1;2/17:0 (Gb3), GM3-D3 18:1;2/18:0 (GM3), GM1-D3 18:1;2/18:0 (GM1), lyso-phosphatidate 17:0 (LPA), lyso-phosphatidylcholine 12:0 (LPC), lyso-phosphatidylethanolamine 17:1 (LPE), lyso-phosphatidylglycerol 17:1 (LPG), lyso-phosphatidylinositol 17:1 (LPI), lyso-phosphatidylserine 17:1 (LPS), phosphatidate 17:0/17:0 (PA), phosphatidylcholine 15:0/18:1 D7 (PC), phosphatidylethanolamine 17:0/17:0 (PE), phosphatidylglycerol 17:0/17:0 (PG), phosphatidylinositol 16:0/16:0 (PI), phosphatidylserine 17:0/17:0 (PS), cholesterol ester 16:0 D7 (CE), sphingomyelin 18:1;2/12:0;0 (SM), sulfatide d18:1;2/12:0;0 (Sulf), triacylglycerol 17:0/17:0/17:0 (TAG) and cholesterol D6 (Chol). Gb4 was estimated semi-quantitatively, using the Gb3 standard. After extraction, the organic phase was transferred to an infusion plate and dried in a speed vacuum concentrator. 1st step dry extract was re-suspended in 7.5 mM ammonium acetate in chloroform/methanol/propanol (1:2:4; V:V:V) and 2nd step dry extract in 33% ethanol solution of methylamine in chloroform/methanol (0.003:5:1; V:V:V). All liquid handling steps were performed using Hamilton Robotics STARlet robotic platform with the Anti Droplet Control feature for organic solvents pipetting.

Validation of standards for quantitation

Our quantitative lipidomics approach uses non-natural analogs as internal standards. We have performed a control experiment to demonstrate that acyl chain length does not introduce a major systematic bias in lipid quantification. Using PE 34:0(17:0/17:0) as the internal standard, we quantified lipid abundances in a known sample, the UltimateSPLASH ONE mix from Avanti. The measured abundances of PE 31:1, PE 33:1, PE 35:1, PE 37:3, and PE 39:4 were all within 5% (and often within 2%) of expectation, despite those analytes containing biologically meaningful variety in acyl chain length and unsaturation. Further, there was no systematic bias with degree of saturation or length.

We further confirmed the accuracy of the quantification by comparing three different standards of varying chain length and degree of unsaturation within a complex sample (here, blood plasma). Independent of the internal standard used, quantification of reference substances is accurate within 20%, in most cases within 10%.

MS data acquisition

Samples were analyzed by direct infusion on a QExactive mass spectrometer (Thermo Scientific) equipped with a TriVersa NanoMate ion source (Advion Biosciences). Samples were analyzed in both positive and negative ion modes with a resolution of $R_{m/z=200}$=280000 for MS and $R_{m/z=200}$=17500 for MSMS experiments, in a single acquisition. MSMS was triggered by an inclusion list encompassing corresponding MS mass ranges scanned in 1 Da increments.[71] Both MS and MSMS data were combined to monitor CE, Chol, DAG and TAG ions as ammonium adducts; LPC, LPC O-, PC, PC O-, as formiate adducts; and CL, LPS, PA, PE, PE O-, PG, PI and PS as deprotonated anions. MS only was used to monitor LPA, LPE, LPE O-, LPG and LPI as deprotonated anions; Cer, HexCer, and SM as formiate adducts and cholesterol as ammonium adduct of an acetylated derivative.[72]

Data analysis and post-processing

Data were analyzed with in-house developed lipid identification software based on LipidXplorer.[73,74] Data post-processing and normalization were performed using an in-house developed data management system. Only lipid identifications with a signal-to-noise ratio >5 and a signal intensity 5-fold higher than in corresponding blank samples were considered for further data analysis.

Lipidomic analysis yielded a list of >600 individual lipid species and their picomolar abundances. These were processed by first removing the TAG and sterol esters from the analysis and expressing the remaining lipids as mol% of membrane lipids. Within a class (depending on which enzyme was used per experiment) each lipid species was then compared separately for each individual biological replicate (that is, the enzymatically treated samples were directly compared to the untreated parallel sample for each individual experiment to control for variance across erythrocyte isolation or human donor). The outer leaflet contents of lipid L (χ_L^{out}) were obtained by subtracting the relative abundance of L in the enzyme-treated samples (χ_L^{enz}) from that in the untreated samples (χ_L) with each being expressed as mol% of total membrane lipids:

$$\chi_L^{out} = \chi_L - \chi_L^{enz}.$$

Each species calculated to be on the inside (that is, χ_L^{enz}) was summed to give the total inner leaflet composition, and each species calculated to be on the outside was summed to give the total outer leaflet composition. All measured glycosphingolipids were assumed to be on the outer leaflet. These values then report on the total contents of lipids in each leaflet. The ranges reported here for each lipid class are determined from the mean and standard deviations for the individual lipid species within the lipid class. To obtain the range of total lipid abundances for each leaflet, the means of the lipid classes from that leaflet were summed, and their errors propagated accordingly.

Hemolysis measurements

For all enzyme treatments, hemolysis was monitored to ensure that the erythrocytes remained intact, and only conditions that yielded no hemolysis were considered for asymmetry studies. Hemolysis was quantified by measuring the absorbance of the supernatant of the enzyme-treated cells at 540 nm on a Tecan plate reader. As an additional test, erythrocytes were incubated with FITC-dextran (MW = 3 kDa) during treatment with SMase and imaged on a Nikon A1R laser scanning confocal microscope immediately after treatment to ensure no leakage of dye into the erythrocyte cytoplasm.

Estimation of the abundances of other unreported membrane components

To estimate the proportion of GPI-anchored proteins as a mole fraction of erythrocyte lipids, we used published values to estimate the abundance of both. From Kuchel et al.,[75] we estimated the surface area of an erythrocyte as $\sim$150 μ m^2, subtracted 20% of this surface area for transmembrane domain-containing proteins[76] and another 20% for cholesterol, giving a total erythrocyte phospholipid surface area of 90 μ m^2 (9 × 10^9 Å^2). Assuming a conservative average phospholipid surface area of 60 Å^2,[6] the approximate number of phospholipids to cover the outer leaflet erythrocyte surface area is thus on the order of 1.5 × 10^8.

The four abundantly expressed GPI-APs in erythrocytes are CD59, DAF, Semaphorin-7a, and AChE.[77–79] The expression levels (molecules/erythrocyte) of CD59 and DAF have been estimated using biochemical approaches as being 2 × 10^4[80] and 3.3 × 10^3,[80,81] respectively. A more recent proteomic analysis[78] attempted to quantify protein copy numbers in erythrocytes, with impressive consistency with the older biochemical measurements (e.g., CD59 and DAF detected in the range of 1 × 10^3 - 3 × 10^4 molecules/erythrocyte). This analysis also reported copy numbers for AChE ($\sim$1-5 × 10^3) and Semaphorin-7a (0.9-2.2 × 10^4). None of the other known erythrocyte GPI-APs had abundance above 0.5 × 10^3. Thus, the combined GPI-APs comprise $\sim$5 × 10^4 molecules / erythrocyte, which compared to $\sim$1.5 × 10^8 phospholipids in the outer leaflet suggests them to be a negligible fraction of the membrane lipidome.

Transmembrane proteins comprise $\sim$20% of plasma membrane area,[76,82] which would not be sufficient to counterbalance the area imbalances implied by differential phospholipid abundances of the two PM leaflets we report. Moreover, transmembrane domains are generally asymmetric in their shape, occupying more area in the inner leaflet,[6,82,83] which would exacerbate rather than alleviate the area mismatch due to phospholipid imbalances.

Finally, there are likely lipid components that are not identified in our lipidomics analysis. The most prominent among these are phosphoinositide lipids, whose hydrophilicity and charge present a challenge for quantitative shotgun lipidomics; however, phosphoinositides have been reported to comprise on the order of 1 mol% of cellular lipids.[84] Similarly, lysolipids, cardiolipins, ceramides, etc. comprise <1 mol% each. Other minor components (including potentially yet-unidentified ones) are likely even less abundant.

Molecular Dynamics (MD) simulations

Tolerance for PL imbalance: CG simulations

To examine the effect of cholesterol (Chol) on the tolerance of lipid membranes to phospholipid (PL) imbalance, we built a series of asymmetric membranes with a lipid composition mimicking that of the erythrocyte plasma membrane but with fixed PL imbalance (35% more PLs in the cytoplasmic leaflet) and varying amounts of Chol (ranging between 10 and 50 mol% of all membrane lipids). Table S2 summarizes the initial lipid make-up of the membranes.

All bilayers were built with the Martini bilayer builder in CHARMM-GUI.[67] In addition to the bilayer lipids each system was solvated with water molecules comprising a 40 Å-thick layer above and below the bilayer, charge-neutralized with Na^+ ions, and additional Na^+ and Cl^- ions were added amounting to a final salt concentration of 150 mM (the number of ions was determined by CHARMM-GUI).

Equilibration of the systems was carried out in Gromacs[63] with the Martini 2.2 force-field,[85] following the 6-step protocol provided by CHARMM-GUI. After equilibration all cholesterol molecules were replaced with a recently optimized cholesterol model[86] which circumvents previously reported problems with cholesterol in Martini.[87]

A subsequent production run of 10 μ s was carried out with Gromacs. The simulations were run with a timestep of 20 fs at a temperature of 45°C. Van der Waals interactions were modeled with a Potential-shift-verlet algorithm and a cutoff of 1.1 nm. Long-range electrostatic interactions were modeled with the Martini 2 reaction field electrostatics and a Coulomb cutoff of 1.1 nm. The lincs_iter and lincs_order parameters were set to 1 and 4, respectively, in accordance with the parameterization of the improved Chol model.[86] The remaining simulation parameters included the standard set of input parameters for the production run provided by CHARMM-GUI including a semi-isotropic pressure coupling with the Parrinello-Rahman barostat and a reference pressure of 1 bar, and temperature control with velocity rescaling and a time constant for coupling of 1 ps.

Cholesterol interleaflet distribution was determined from the orientation of the Chol molecules. In particular, the angle between the vector defined by the ROH and R5 beads of Chol was calculated with respect to the bilayer normal (0,0,1) from the last 5 μ s of the trajectories. All molecules with tilt angles less than 90 degrees were counted in the top exoplasmic-like leaflet and all molecules with tilt angles greater than or equal to 90 degrees were counted in the bottom cytoplasmic-like leaflet. Phospholipids did not change their leaflet residence during the simulations.

The maximal phosphate-to-phosphate distance was calculated from the difference between the minimum and maximum z positions of all phosphate (PO4) beads in each frame of the trajectory, and plotted as histograms.

Effect of PS flip-flop on tension: AA simulations

To evaluate the effect of flipping PS lipids to the opposite leaflet, we performed a series of all-atom (AA) simulations in which the total number of lipids in the bilayer remained fixed and we mimicked PS flipping by generating different starting configurations with respect

to PS interleaflet distribution. The effects of Chol flipping were examined in the same way. These simulations were relatively short (not much more than a microsecond) with the goal of equilibrating lipid packing for calculation of the respective leaflet tensions while avoiding any spontaneous translocation of lipids and Chol between leaflets.

All bilayer systems were constructed with CHARMM-GUI's Bilayer Builder. Their lipid compositions and system sizes are listed in Table S3. The bilayers were initially equilibrated in NAMD[62] with CHARMM-GUI's 6-step equilibration protocol using the CHARMM36 force-field.[88] The same software and force field were used for the subsequent production runs which utilized a 2 fs timestep with *rigidbonds* set to all. Van der Waals interactions were truncated at 12 Å and CHARMM's force switching function was applied between 10 and 12 Å with the *vdwforceswitching* option in NAMD. Electrostatic interactions were modeled with the Particle Mesh Ewald (PME) method with a grid spacing of 1 Å. The simulations were run in the NPT ensemble with a semi-isotropic pressure coupling. The temperature and pressure were maintained at 37°C and 1 atm respectively using Langevin thermostat (damping coefficient of 5 ps^{-1}) and barostat (period 200 fs and decay 50 fs). The total lengths of these production runs are indicated in Table S3.

The tension in each leaflet of the simulated asymmetric bilayers was calculated as described previously.[89] Briefly, each system was first centered so that the average z position of the terminal methyl carbons of all phospholipids was in the center of the simulation box at $z = 0$ (note that the results did not change significantly when we calculated the average z positions of the terminal methyl carbons of the two leaflets separately and centered the bilayer using their mean instead). The lateral pressure profile of each system was computed with NAMD 2.11 since later versions have a bug preventing the calculation. The system was divided in N_s slabs where N_s was chosen so that the average slab thickness was ~ 0.8 Å, and the non-Ewald and Ewald (with Ewald grid size in each direction set to 30) contributions to the pressure tensor were calculated separately from the stored atomic coordinates and velocities with the Harasima contour, and summed to obtain the final X (p_{xx}) and Y (p_{yy}) components of the pressure tensor. The normal Z component of the pressure tensor (p_N) in each slab was estimated as the constant $p_N = L_N^{-1} \int \frac{1}{2}(p_{xx}(z) + p_{yy}(z))dz$ where L_N is the length of the simulation box along the bilayer normal. The pressure profile was then computed as $p(z) = \frac{1}{2}(p_{xx}(z) + p_{yy}(z)) - p_N$ and the tension in each leaflet was obtained by integrating $p(z)$ from $-\infty$ to 0 (bottom leaflet) or from 0 to $+\infty$ (top leaflet) and multiplying the result by (-1). Errors on the tension were estimated with a bootstrapping approach in which a dataset with the same total number of frames was reconstructed by picking frames from the original dataset at random and allowing repetitions. The pressure profile and leaflet tensions were then obtained from the resampled data. This procedure was repeated multiple times to obtain the error (i.e. standard deviation) of the leaflet tension.

Cholesterol distribution in asymmetric membranes: CG/AA simulations

To examine the effects of phospholipid imbalance and tension on cholesterol distribution in asymmetric membranes, we performed a series of simulations first in coarse-grained (CG) and then in all-atom (AA) representations.

Coarse-grained simulations. Initially, 8 asymmetric bilayers with one saturated leaflet (composed of 100 DPPC lipids) and one unsaturated leaflet (composed of a varying number of DAPC lipids), each containing 30 mol% cholesterol (Chol), were constructed with the Martini maker in CHARMM-GUI. Table S4 lists the starting configurations of all bilayers. The systems were equilibrated with CHARMM-GUI's 6-step protocol and simulated at 40°C for 10 μ s with Gromacs. The standard set of parameters for the production run are the same ones as listed above and included a timestep of 20 fs, 1.1 nm cutoffs for Coulomb and Van der Waals interactions, and Martini 2 reaction field electrostatics. While the lincs_iter and lincs_order parameters were set to 1 and 4 respectively, as above, the simulations were run with the old Martini 2.2 version of cholesterol since the newer model was not available at the time. For two of the systems, (A.5 and A.10), we later reran the simulations with the new Chol model[86] and verified that there were no observable differences in their equilibrium Chol interleaflet distributions.

To count the number of lipids and Chol in each leaflet, the bilayer was first centered so that the bilayer midplane was in the center of the simulation box in every frame. Then, the DAPC and DPPC lipids whose phosphate (PO4) beads were below/above the bilayer center were counted as belonging to the bottom/top leaflets respectively. Chol was treated the same way except that its headgroup OH bead was used instead. Chol distribution equilibrated within the first few μ s in all systems and all reported quantities are averaged over the last 5 μ s of the trajectories. None of the phospholipids changed its leaflet residence during the simulations.

All-atom simulations. The equilibrated lipid distributions from the CG simulations were used to construct all-atom bilayers with CHARMM-GUI's Membrane Builder. Table S4 lists the respective lipid leaflet compositions. The bilayers were hydrated with more than 40 waters per lipid and no added salt. They were simulated with NAMD 2.12 first following CHARMM-GUI's 6-step equilibration protocol, then a production run utilizing a 2 fs timestep with *rigidbonds* set to all. Van der Waals interactions were truncated at 12 Å and CHARMM's force switching function was applied between 10 and 12 Å with the *vdwforceswitching* option in NAMD. Electrostatic interactions were modeled with the Particle Mesh Ewald (PME) method with a grid spacing of 1 Å. The simulations were run in the NPT ensemble with a semi-isotropic pressure coupling. The temperature and pressure were maintained at 40°C and 1 atm respectively using Langevin thermostat (damping coefficient of 5 ps^{-1}) and barostat (period 200 fs and decay 50 fs). The total lengths of these production runs are indicated in Table S4.

The tension in each leaflet of the simulated asymmetric bilayers was calculated from the AA trajectories as described in Section 2.2.

PM models: AA simulations

To examine the effects of PL imbalance on cholesterol interleaflet distribution and bilayer properties we built 3 asymmetric models of the plasma membrane. Each had ~40 mol% overall cholesterol and the same leaflet phospholipid compositions modeled after the

lipidomics results, but differed in the relative total abundances of PLs in their two leaflets (see Table S5 for the exact numbers and types of lipids in each leaflet). The bilayers were constructed and simulated as described below.

The "Equal" bilayer (asymmetric lipid composition, but matched leaflet areas) was built by first simulating two symmetric bilayers, one with the inner leaflet composition and one outer leaflet composition (previously published in Lorent et al.[6]). After the areas of each were relaxed, an asymmetric bilayer was constructed by taking one leaflet from each simulation, placing them tail to tail, and resolvating with the VMD plugins "solvate" and "ionize." The final system contained ~69,000 water molecules (~53 waters per lipid) and sodium and chloride ions for a final salt concentration of 156 mM. The system was then relaxed using the 6-step CHARMM-GUI protocol described below.

The other two PM models with larger PL imbalances were built with CHARMM-GUI with the initial numbers of PLs and Chol in each leaflet as indicated in Table S5. At the time of construction some lipids were not available in CHARMM-GUI and the bilayers were first constructed with similar available lipids whose structure was subsequently modified. These lipids were as follows: DGPE (20:1,20:1 PE) in place of OAPE; PAPC in place of PAPS; and DEPE (22:1,22:1 PE) in place of PDPE and PLQS. After the structural modifications the systems were hydrated with ~25,000 water molecules (~80.5 waters per lipid) and sodium and chloride ions for a final salt concentration of 150 mM. The hydration and ionization were done with the solvate plugin in VMD.

Additional symmetric bilayers with the lipid compositions of the exo (exo-sym), cyto (cyto-sym) leaflet or overall bilayer (scramble) of the Cyto+ model were built in a similar way. Their lipid compositions were as follows: LSM/NSM/PSM/PAPC/PLPC/SOPC/Chol 7/8/10/3/11/6/55 mol% in exo-sym, OAPE/PAPS/PDPE/PLPC/PLQS/POPC/Chol 6/22/13/15/15/6/23 mol% in exo-cyto and LSM/NSM/PSM/OAPE/PAPC/PAPS/PDPE/PLPC/PLQS/POPC/SOPC /Chol 4/4/6/3/2/9/6/13/6/3/3/41 mol% in scramble.

All systems were first equilibrated with CHARMM-GUI's 6-step equilibration protocol in NAMD (an updated list of dihedral angle constraints was generated and used instead of the one supplied by CHARMM-GUI after the structural modifications of the lipids described above). The systems were then transferred to Anton2 for long production runs as detailed in Table S6. The Anton-specific system set-up and parameters were as described in Lorent et al.[6] The final snapshots of the simulations were then used to start subsequent NAMD production runs with simulation lengths outlined in Table S6. The NAMD runs utilized the same simulation parameters as those described in the all-atom simulations in Section 3.3.

Prior to analysis the system was centered so that the bilayer was in the middle of the simulation box and the average (x,y,z) of the bilayer midplane was at (0,0,0). The last 1.2 μ s of the simulations (with output frequency of 120 ps) were used for all analysis except for lipid diffusion which was calculated over the trajectory lengths indicated in Table S6 with output frequency of 20 ps.

Individual lipid areas were calculated with the Area per Lipid tool in MEMBPLUGIN[66] which performs Voronoi analysis with user-specified sets of atoms defining the position of each type of lipid in the bilayer. Here the corresponding definitions consisted of the three glycerol backbone carbon atoms for all phospholipids and the oxygen atom for cholesterol.

The acyl chain order parameters were calculated with custom Tcl and MATLAB scripts with the formula:

$$S_{CD}(C_i) = \langle \frac{1}{2}(3\cos^2\beta - 1) \rangle$$

where β is the angle between a CH bond at carbon C_i and the bilayer normal (the z dimension of the simulation box) and $\langle \cdot \rangle$ denotes ensemble average over all CH bonds, lipids and trajectory frames.

The 3-dimensional bilayer density was calculated with the VolMap plugin in VMD at a resolution of 1 Å in a 25 x 25 x 40 Å box centered in the middle of the simulation box. The reported density was the average over the analyzed trajectory frames.

The differential stress (tension/compression) in the leaflets was calculated from the lateral pressure profile of the bilayer as described in Section 3.2. The first moments were obtained by integrating the product $zp(z)$ over each leaflet, i.e., $0 \rightarrow +\infty$ or $0 \rightarrow -\infty$ for the top and bottom leaflets, respectively.

To analyze the permeability of a membrane we first identified all water molecules that at some point in time were found 10 Å or more below the instantaneous average z position of the lipid phosphate groups in either leaflet. We then recorded the time evolution of the z coordinates of each of these water molecules throughout the trajectory frames. This data was then used to count the number of times water molecules entered the bilayer from one side, reached within 10 Å of the bilayer midplane, i.e. with $-10 \leq z \leq 10$ Å, and either moved through the opposite leaflet and exited from the other side (full transitions) or turned back and exited from the same side (partial transitions). The number of full and partial transitions was normalized by the lateral area of the bilayer and the total simulation time of the analyzed portion of the trajectory.

Defects in the bilayer, defined broadly as inhomogeneities on the surfaces of the two leaflets, were calculated with two different algorithms. The first one utilized the PACKMEM tool as detailed in Gautier et al.[65] which performs a 2-dimensional analysis of the defects in each leaflet. The output included the numbers of shallow and deep defects defined as above or below 1 Å under the glycerol backbone surface of the lipids, and the mean and standard deviation of the average defect sizes calculated from block averaging.

The second algorithm analyzed defects in 3D as detailed in Tripathy et al.[90] The reference atoms were the same as in Tripathy et al.,[90] that is C2 for non-sphingomyelin and C2S for sphingomyelin phospholipids and O3 for cholesterol in CHARMM36 notation. The output contained the distributions of both defect sizes and their depths, and the defect size constant was obtained from the former by taking the inverse of the slope of the semi-log relationship (size vs. log of distribution) in the size range 150–250 Å^2.

To analyze the lipid and Chol diffusion from each trajectory, we first took the raw coordinates of the lipid phosphate atoms (P in CHARMM36 notation) or Chol's oxygen atom (O3 in CHARMM36 notation) from every trajectory frame output at a frequency of 20 ps, and unwrapped them (that is, removed any jumps in the coordinates between frames due to wrapping around the periodic boundaries). We then used the time evolution of these atoms' (x,y) positions to calculate the 2-dimensional mean squared displacement, $msd(t)$, and average it over all lipids (or all Chol molecules) in each leaflet. A small region of the $msd(t)$ function was then fit to $f(t) = 4Dt$ where D is the diffusion coefficient. This small region was chosen with a heuristic approach where consecutive 100-ns-long blocks of the $msd(t)$ function were fit to $g(t) = ax^b$ and the block with the largest b parameter was the one used for obtaining D. Representative plots of the data and fits is shown in Figure S7. Errors on the diffusion coefficients for each leaflet were calculated with a bootstrapping approach in which a dataset with the same total number of lipids was constructed by picking lipids at random, then the respective $msd(t)$ profiles were averaged and analyzed as above. The procedure was repeated multiple times and the standard deviation of the resulting diffusion coefficients was reported.

Calibration of APL and Di4 lifetime: AA simulations

To calibrate the Di4 lifetime obtained from GUV experiments (see section 4.4) to the area per lipid calculated from MD simulations, we performed a series of AA simulations of symmetric bilayers with the same lipid compositions as those of the experimentally measured liposomes. All bilayers were constructed, equilibrated and simulated as outlined in section 2.2, except that the temperature of the simulations was set to 25°C to match the experimental conditions. Each bilayer had 100 lipids per leaflet (including Chol) and the reported area per lipid was calculated by dividing the equilibrated lateral box size by the number of lipids in the leaflet (i.e. 100). Note that the data for the DOPC bilayers with 0, 10, 20, 30, 40 and 50 mol% Chol was taken from Chakraborty et al.[91] The lengths of the new simulations analyzed here were as follows: 710, 704, 970, 935, 1034 and 1175 ns for POPC with 0, 10, 20, 30, 40 and 50 mol% Chol respectively, 570 ns for DOPC/DOPS 80/20 and 1400 ns for DPPC/Chol 70/30.

In vitro experiments with liposomes

Cholesterol and membrane tolerance for PL imbalance: LUVs

Three types of liposomes (POPC with 0, 20 and 40% Chol) were prepared as follows. Lipids were mixed in organic solvent at the appropriate concentrations then dried first under gas nitrogen until the solvent evaporated, then in a vacuum oven at ambient temperature overnight. The dry films were warmed to 40°C, then pre-warmed water was added to a final lipid concentration of 24 mM. Hydration was done for one hour at 40°C with intermittent vortexing. The resulting multilamellar vesicles were frozen with liquid nitrogen, then thawed at 40°C for 5 min for a total of 5 freeze/thaw cycles. The samples were extruded for 31 total passes through a 100 nm pore size filter with a manual Avanti extruder either at room temperature (without Chol) or at elevated temperature of ~50°C (with Chol). The resulting large unilamellar vesicles (LUVs) were stored at room temperature and subsequent measurements were done within one week of preparation.

A concentrated stock solution of (2-Hydroxypropyl)-α-cyclodextrin (HP α CD, Sigma Aldrich) was prepared by weighing 14.75 g of HP α CD in a beaker, then adding ~15 mL water and incubating at room temperature without agitation for 1−2 days until visually dissolved and uniform. The solution was then transferred to a 25 mL volumetric flask, brought up to 25 mL with water for a nominal concentration of 500 mM, and mixed by slowly inverting the flask multiple times. The concentrated stock solution contained a small amount of large micron-sized aggregates as determined by DLS. To remove these aggregates the solution was transferred to a pre-washed centricon filter device (Ultra-15, 100,000 Da molecular weight cutoff; Amicon; MilliporeSigma, Burlington, MA), and spun at 3500 x g until ~1 mL was left in the retentate. The filtrate which contained particles of sizes between 1 and 5 nm was transferred to a falcon tube and used for subsequent measurements.

POPC extraction from the liposomes was achieved by incubating LUVs with HP α CD as follows. First, varying amounts of the HP α CD solution were brought up to 1 mL with water and pipette-mixed until no strands of HP α CD were visible in the solution. Then, 7 μ L of the LUVs were added for a final lipid concentration of 170 μ M and pipette-mixed again until the solution looked uniform. Equilibration of POPC between the liposomes and HP α CD was very rapid and the samples were incubated at room temperature without further agitation for anywhere between a few minutes and an hour prior to measurement.

Light scattering was measured on an Anton Paar Litesizer 100 with disposable cuvettes. Immediately prior to the measurement the 1 mL-sample was pipette-mixed and the cuvette was capped. Each sample was measured at 22°C three times in a repetition series using automatic modes for filter, focus and quality control (i.e. number of runs). The raw light scattering data from each repetition was recorded and the data was used to obtain the mean and standard deviation for that sample.

To quantify and compare the amounts of extracted POPC lipids, after the light scattering measurement each sample was first spun through a pre-washed centricon filter device (Ultra-15, 100,000 Da molecular weight cutoff; Amicon; MilliporeSigma, Burlington, MA) at 3500 x g for 10−20 minutes until the retentate reached dead stop volume. The filtrate was transferred to a glass culture tube and 2 μ l of DMPC (25.27 mg/mL in chloroform) were added with a glass Hamilton syringe as a standard. The sample (total volume ~1 mL) was lyophilized by first storing it at -80°C overnight, then dipping in liquid nitrogen immediately prior to placing in a lyophilizer overnight. The lyophilized powder was subjected to acid-catalyzed methanolysis to extract the fatty acid methyl esters for analysis with gas chromatography-mass spectrometry (GC/MS) as done previously.[92] Briefly, 1 mL of 1 M methanolic HCl was added to the powder and vortexed until completely dissolved, then flushed with argon and capped with a Teflon-lined cap. The sample was incubated at 85°C for 1 hr and allowed to cool for a few minutes. Then, 1 mL water and 1 mL hexane were added one after the other with vigorous

vortexing after each addition to extract the FAMEs. The sample was spun for 5 min at 400 x g to break the resulting emulsion and the upper phase (containing hexane) was transferred to a GC autosampler vial and brought up to about 1 mL with hexane. FAME analysis was done on an Agilent 5890A gas chromatograph (Santa Clara, CA) with a 5975C mass-sensitive detector operating in electron-impact mode and an HP-5MS capillary column (30 m x 0.25 mm, 0.25-mm film thickness). A preprogrammed column temperature routine was performed as described in detail in Doktorova et al.[92] Total ion chromatogram peaks were assigned and integrated with the GC/MSD ChemStation Enhanced Data Analysis software. The respective peak areas of the FAMEs corresponding to the myristoyl chain of DMPC and the palmitoyl chain of POPC were recorded and used to calculate the normalized amount of POPC in the sample.

DHE self-quenching in liposomes

Vesicles were prepared following the rapid solvent exchange (RSE) protocol.[93] Briefly, lipid mixtures (each totaling 20 nmol) without and with DHE were prepared in chloroform in a glass culture tube. Prior to mixing, the mass of the tube (m_0) was recorded, 25 μ L chloroform were added to it and lipid stock solutions were diluted appropriately so that the total volume of the 20 nmol lipid mixture in the tube was less than 100 μ L. Following that, 400 μ L pure water were added to the tube and the sample was subjected to the RSE protocol by applying vacuum while vortexing for 90 seconds, followed by short purging with argon. Immediately after that, the mass of the tube (m_1) was recorded again and 200 μ L of the RSE vesicle suspension were taken out and mixed with 1.8 mL of pure water. The 2 mL sample was transferred to a 1 cm path length quartz cuvette and measured on a spectrofluorometer as detailed below. Due to potential slight differences in the total volume of the RSE vesicle suspension (due to small variations in the applied vacuum and argon purging), the deviation of the mass of the sample, $m_{sample} = m_1 - m_0$, from the mass of 400 uL pure water measured in similar way was used to normalize the sample volume (and thus lipid and DHE concentration) across all samples.

The fluorescence intensity was measured on a Horiba Fluorolog 3 spectrofluorometer by exciting the sample at 327.8 nm and collecting the emission in the range 340–640 nm. The excitation and emission slits were set to 2.5 and 3 nm, respectively and the integration time was 0.1 s. The 2 mL sample was continuously stirred during the measurement via a flea stir bar placed in the cuvette.

To compare the DHE fluorescence across samples, the full spectrum of each sample was first normalized by subtracting the spectrum of the respective lipid-only (without DHE) sample. The normalized spectra were then integrated to obtain total DHE fluorescence, and the value was corrected for the volume difference measured during sample preparation. Integration of the DHE spectra, as opposed to using the fluorescence at a fixed wavelength, was necessary due to changes in the shape of the spectrum as a result of the formation of various DHE configurational states at higher DHE concentrations[94] (Figure S4).

FRET experiments with DHE and Di4: LUVs

Aqueous lipid dispersions at 25 mg/mL were prepared by first mixing appropriate volumes of lipid stocks in organic solvent with a glass Hamilton syringe. The solvent was evaporated with an inert gas stream followed by high vacuum overnight. The dry lipid film was hydrated with ultrapure water above the main transition temperature of the highest-melting lipid in the sample for at least 1 h with intermittent vortex mixing. The resulting multilamellar vesicle (MLV) suspension was subjected to at least 5 freeze/thaw cycles using a −80 °C freezer, then extruded through a polycarbonate filter using a handheld mini-extruder (Avanti Polar Lipids) by passing the suspension through the filter 31 times. Unsaturated lipids were extruded at room temperature, and multicomponent mixtures were extruded at 45°C. For DHE-containing vesicles, DHE was incorporated into the lipid mixture in organic solvent (prior to drying and hydration). DHE titrations were performed by replacing cholesterol for DHE and keeping total sterol concentration constant.

Measurements were done on a PTI fluorimeter. To minimize inner filter effect (IFE), measurements were taken using a 10 × 2mm pathlength cuvette oriented with 2mm pathlength facing detector and minimal sample volume: 1 μ L of 2.5 mg/mL LUVs was diluted into 165 μ L of Ringer's solution, yielding ∼15 μg/mL LUVs in the cuvette. Di4 (stock dissolved in ethanol) was first diluted 10x in Ringer's solution, then 1.5 μL from the diluted solution were added to the LUV suspension and pipette mixed (3 strikes with 100 μL volume). IFE was negligible due to minimal absorbance measured at the DHE and Di4 absorbance ranges. Excitation and emission slits were open to 5 nm and the gain was optimized for increased signal. All measurements were taken at a scan rate of 0.1 s/nm to minimize photobleaching. Samples were checked for risk of photobleaching via time-based emission scans. DHE emission spectra was obtained by excitation at 310 nm and emission between 340–500 nm at 37°C. Measurements with Di4 were taken immediately after addition with each sample of LUVs discarded after each measurement and the cuvette thoroughly washed.

Calibration of APL and Di4 lifetime: GUVs

Giant unilamellar vesicles (GUVs) were prepared by electroformation as described previously.[6] Briefly, 1 μl of the lipid solution (1:2 methanol/chloroform at 2.5 mg/mL) was applied to Pt electrodes of an electroformation chamber. The solution was dried in vacuum for 3 h, then rehydrated in 0.4 M sucrose. Electroformation was performed at 500 Hz and 2.5 V for 2 h at 50 °C and left overnight in heat block to return to room temperature naturally.

Measurements of Di4 lifetime of GUVs were performed as previously described.[6] Briefly, GUVs were stained with Di4 by adding Di4 dissolved in a mixture of ethanol (10%) and 0.4 M sucrose (90%) to the sample at a final concentration of 250 nM (the amount of ethanol in the GUV suspension did not exceed 0.1% v/v). The sample was incubated for 5 min at room temperature, following which 10 μl of the stained GUVs were diluted into 200 μl of 0.4 M glucose solution (containing 0.5% agarose to prevent vesicle movement during FLIM). The samples were imaged at room temperature on a Leica SP8 FLIM confocal microscope with excitation at 485nm

with an 80MHz pulsed laser, and the lifetime collected in an emission window of 550−800nm. The data was then fit using a 2-component reconvolution fit, and the intensity-weighted average lifetime was reported.

In vivo experiments with erythrocytes

DHE exchange in erythrocytes

Erythrocytes were isolated from healthy donors with informed consent via the Institutional Biosafety Committee of the University of Texas Health Science Center. In short, 90μ L of whole blood was obtained by finger prick method and mixed with 10μ L acid citrate dextrose solution. The mixture was then layered atop equi-volume of purchased polymorph prep solution and spun at 2,000 x g for 5 minutes at room temperature. All solution except the erythrocyte pellet was aspirated, and the erythrocyte pellet was resuspended and washed three times in Ringer's solution (125 nM NaCl; 5 mM KCl; 3 mM CaCl2; 1 mM MgSO4; 30 mM HEPES; 5 mM glucose; pH 7.4).

Lipids were extracted using a two-step extraction protocol.[69] First, a 5x volume of 10:1 chloroform:methanol (v:v) solution was added to cells followed by nutation at room temperature for 30 minutes. The sample was centrifuged at 2350 rcf for 15 minutes and the organic (bottom) phase was transferred into a separate tube. The procedure was repeated with 3:2 chloroform:methanol, with the resulting organic phase added to the organic phase previously set aside. Finally, the sample was dried under N_2 and reconstituted in 100% ethanol.

To identify DHE for cholesterol exchange conditions that did not affect total sterol levels in RBCs (see Figure S3A), the Amplex Red assay was performed (according to manufacturer instructions; Invitrogen) to determine total sterol abundance (i.e. cholesterol and DHE combined). We validated that the assay is approximately equally sensitive to DHE and cholesterol by measuring a standard curve for DHE and cholesterol separately. Each reading was normalized to cell count. Technical triplicates were measured for each sample. Values shown in Figure S3A are normalized to untreated cells and are the average and standard deviations from at least two independent biological replicates.

DHE was first solubilized in ethanol as follows: 5 mg DHE (Sigma E2634) were dissolved in 628 μ L of 100% ethanol to give a final concentration of 20 mM. The sample was sonicated in a bath sonicator to completely solubilize any aggregates. Next, 42.4 mg of M β CD were dissolved in 200 μ L of Ringer's solution to yield final concentration of 160 mM M β CD and vortexed until clear. To complex DHE and M β CD, 100 μ L of the DHE solution was dried under N_2 for ~30 min and the film was dissolved with 100 μ L of the M β CD solution for a MβCD to DHE molar ratio of 8:1. The M β CD solution was clear in the absence of DHE and cloudy in the presence of DHE. Full solubilization of DHE in M β CD could not be achieved with sonication or overnight incubation at 37°C with a thermomixer. Insoluble DHE aggregates were spun out with a brief spin.

3.5×10^8 cells/mL were spun down and suspended in a mixture of the DHE/M β CD solution and free M β CD in Ringer's solution for final concentrations of 50 μ M DHE and 1.2 mM M β CD, unless otherwise specified, and nutated for 10 minutes at room temperature. The sample was washed 3 times with Ringer's solution with 2,000-rcf spins for 3 minutes at room temperature. The supernatant from the first spin was saved to test for hemolysis.

Cells were imaged by light microscopy with an epifluorescence microscope with 40x objective to assess maintenance or loss of discoid shape.

DHE quantification was performed by measuring DHE emission spectra of lipid extracts in 100% ethanol of erythrocytes labeled with DHE by subtracting emission spectra of lipid extracts from unlabeled cells (no DHE). DHE content was calculated by direct comparison to a calibration curve of increasing DHE concentration in ethanol. Total sterol was measured with the amplex red assay as described above. The mol% DHE of total PM lipids, χ^{PM}_{DHE}, was calculated from the amount of DHE relative to total sterol, χ^{sterol}_{DHE}, and the mol% sterol of total PM lipids, χ^{PM}_{sterol}, as:

$$\chi^{PM}_{DHE} = \chi^{sterol}_{DHE}\,\chi^{PM}_{sterol}.$$

DHE quenching in erythrocytes

Di4 was diluted 10-fold to 100 μg/mL in Ringer's buffer before adding to cells (1.5×10^7 cells/mL) at room temperature at the indicated Di4 concentrations. Di4 addition was directly followed by measurement of DHE emission for quantification of quenching via FRET.

The Förster distance R_0 for energy transfer between DHE donor and Di4 acceptor was calculated as[95]:

$$R_0 = \left(\frac{9000\kappa^2\Phi_D \ln(10)}{128\pi^5 N_A n^4} J(\lambda)\right)^{1/6} \approx 0.211\left(\kappa^2 n^{-4}\Phi_D J(\lambda)\right)^{\frac{1}{6}}\,[\text{Å}],$$

where N_A is Avogadro's number, κ^2 is the unitless dipole orientation factor (2/3 in the limit of isotropic motion and dynamical averaging), n is the refractive index of the medium (taken to be 1.42 for a lipid bilayer), Φ_D is the donor quantum yield (0.4 for DHE[96]), and $J(\lambda)$ is the spectral overlap integral:

$$J(\lambda) = \frac{\int_0^\infty F_D(\lambda)\varepsilon_A(\lambda)\lambda^4 d\lambda}{\int_0^\infty F_D(\lambda) d\lambda}.$$

In the calculation of J, $F_D(\lambda)$ is the DHE emission spectrum, $\varepsilon_A(\lambda)$ is the Di4 excitation spectrum normalized to a peak absorbance of $\varepsilon_A = 10{,}110\ M^{-1}cm^{-1}$, and wavelengths are in nm. Excitation and emission spectra were obtained from fluorescence spectroscopic measurements described below. Based on these calculations and assumptions R0 is 28.3 Å or 29.5 Å depending on which Di4 excitation spectrum is used.

Measurements were taken on a PTI fluorimeter as described in Section 4.3. Cells were measured at 1.5×10^7 cells/mL and the temperature was controlled to 37°C. DHE emission spectra was obtained by excitation at 310 nm and emission from 340−500 nm with 2 nm step size and 0.1 s/nm integration time. Di4 emission spectra was obtained by excitation at 488 nm and emission from 550−600 nm with 2 nm step size and 0.1 s/nm integration time.

Measurements were always taken for control (untreated) erythrocytes and subtracted. This was necessary since erythrocytes cause high scattering effects due to their shape and hemoglobin content. For counterpart measurements, cell concentration was checked via cell count. DHE quenching was monitored by measuring the decrease in emission at 385 nm after adding increasing amounts of Di4 until a plateau was reached. The relative amount of quenched DHE fluorescence at this plateau was used to estimate the fraction of DHE residing in the outer leaflet of the membrane.

It is important to emphasize that some fluorescence effects are not fully accounted for in this calculation. Specifically, there is the likelihood of some quenching of inner leaflet DHE from outer leaflet Di4, effects of membrane environment/hydration on DHE and Di4 spectral properties, and cell-to-cell variation in DHE and/or Di4 labeling. Fully characterizing and controlling for these effects would be necessary for quantitatively accurate measurements of DHE transbilayer distribution. However, definitive quantification of cholesterol asymmetry is not the central focus of this manuscript, rather that polar lipid imbalances and preferential lipid-lipid interactions are key determinants of this asymmetry. Our DHE measurements strongly support enrichment of sterol in the outer PM leaflet, consistent with simulations and other experiments (see Figure 4).

Scrambling of erythrocytes

DHE-labeled cells were suspended in 100 μ M phorbol-12-myristate acetate (PMA) for 10 minutes on nutate at room temperature, unless otherwise specified. Di4 was then immediately added to the suspension and cells were measured for DHE distribution as described in the previous section.

Permeability measurements

Equal numbers of erythrocytes (~3.4×10^8 cells/mL), were treated with or without 100 μM PMA for 10 minutes. 2×10^6 cells/mL were resuspended in Ringer's solution to a quartz 2 mL cuvette. Just prior to reading on the spectrofluorometer, 1 μg/mL fluorescein diacetate (stock 1 mg/mL in acetone) was added to the cells and mixed by pipetting. The fluorescence intensity was read at 450 nm excitation and 510 nm emission over a period of 1 min (1 read/second) with 5 nm excitation and emission slits. In each of the samples measured, the slope of the fluorescence increase over time remained constant over the 60 s, consistent with a constant flux (Q) (Figure S5G).

The permeability coefficient (P) of a membrane to a particular substrate is then defined by Fick's Law as:

$$Q = PA(C_{out} - C_{in})$$

where P is permeability, A is the area of the membrane, and C_{out} and C_{in} are the concentrations of the solute outside and inside the cells, respectively. In our experiments, $C_{in} = 0$ because FDA is quickly converted into fluorescein upon entering the cell. With equal A (due to same number of cells and cellular membranes) and C_{out} across samples, permeability can be directly compared by normalizing to control samples to evaluate changes in scrambled PMs.

Experiments with nucleated cells

Chol extraction and PM scrambling/permeability

A CaR buffer containing 145 mM NaCl, 5 mM KCl, 10 mM HEPES at pH 7.4 was prepared, filtered and stored at 4°C until use. A stock solution of 70−90 mM M β CD was prepared in CaR buffer and stored at 4°C until use. A concentrated solution of $CaCl_2$ was also prepared in water, its osmolarity measured with an osmometer (Advanced Instruments) to be 83 mM, and used to add calcium to the CaR buffer when needed. A concentrated (0.5 M) stock solution of EDTA (Thermo Scientific) was used to add EDTA to the calcium-free CaR buffer when needed. Imaging buffer consisted of CaR buffer with either 0.5−0.95 μ M LactC2-mClover (purified via His-tag) and 2 mg/mL Rhodamine-dextran (Sigma-Aldrich T1037, MW 4,400, dissolved in CaR buffer) or 50 μ g/mL propidium iodide (PI, Alfa Aesar J66764, dissolved in water).

Cells were first washed with CaR buffer twice, then incubated with either 2 mM $CaCl_2$ or 2 mM EDTA in the absence or presence of 6 mM M β CD. For monitoring PS exposure and dextran permeability the buffer also contained LactC2-mClover and Rhodamine-dextran. For PI permeability the buffer contained PI. Cells and buffer were incubated at room temperature (20−22°C) and imaged at the indicated time points (30, 60 and 90 minutes). Confocal fluorescence imaging of cells was performed at 21°C using a Nikon C2+ point scanning system attached to a Nikon Eclipse Ti2-E microscope equipped with a Plan Apo Lambda 60X oil immersion objective and a Bioptech objective cooling collar.

Imaging data was analyzed with FIJI. The contour of each cell was first manually traced with a line with Line Width 5. The raw intensity of the green fluorescence (coming from the interaction of LactC2-mClover with the membrane) was recorded and normalized first to the length of the perimeter outlining the cell, then to the background of the image measured in an analogous way by selecting 3

empty regions (with no cells) from different parts of the image. PI permeability was measured by counting PI-positive and PI-negative cells using saponin treatment (dissolved in CaR buffer and added at concentration of 1.6 mg/mL) as a positive control.

Di4 lifetime measurements in untreated and scrambled 3T3 cells

To determine the Di4 lifetime of the outer leaflet of 3T3 cells, cells were incubated with 1 μg/mL Di4 at 4°C for 8 min in CaR buffer (145 mM NaCl, 5 mM KCl, 10 mM HEPES) supplemented with 2 mM $CaCl_2$ and 2 mM $MgCl_2$ at pH 8.0. Cells were briefly washed twice in the same buffer at ambient temperature before imaging at room temperature on a Leica SP8 confocal microscope with a 63x water immersion objective. FLIM images were obtained with 485 nm excitation and emission from 550–800 nm and fit using Leica LAS n-exponential reconvolution with two lifetimes. We report the intensity-weighted mean value. To prevent any contaminating signal from internalization of the dye, all images were acquired within 20 minutes. To determine the Di4 lifetime of scrambled plasma membranes, 3 mM A23187 (Cayman, #11016) was added to cells in the same CaR buffer for 15 minutes at 37°C. Following this treatment, the cells were washed with CaR buffer, and Di4 incubation and imaging occurred as above.

Cholesterol and lipid diffusion in 3T3 cells

3T3 cells were maintained in DMEM medium supplemented with 10% FBS. They were seeded on glass-bottom dishes two days before the diffusion experiments. For fluorescent labeling, the fluorescent lipid analogs (Topfluor SM and Topfluor Chol, Avanti Polar Lipids) were first dissolved in DMSO at a final concentration of 1 mg/ml. Before labelling, the cells were washed twice with L15 medium to remove the full media. Later the fluorescent analogs were mixed with L15 medium at a 1:1000 ratio (final concentration of 1 μg/ml). The cells were incubated with this suspension for three to five minutes at room temperature. After that, the cells were washed with L15 twice followed by fluorescence correlation spectroscopy (FCS) measurements. To measure diffusion of scrambled plasma membranes, 3T3 cells were treated with 3 μM A23187 (Cayman, #11016) ionophore for eight to ten minutes at 37°C before lipid labelling. Scrambling was confirmed by AnnexinV-AF647 labelling (ThermoFisher A23204).

FCS was carried out using a Zeiss LSM 780 microscope, 40X water immersion objective (numerical aperture 1.2). Briefly, before the measurement, the shape and the size of the focal spot was calibrated using Alexa 488 dye in water. To measure the diffusion on the membrane, the laser spot was focused on the bottom membrane of the cells by maximizing the fluorescence intensity. Then, 3-5 curves were obtained for each spot (five seconds each). To avoid the crosstalk from internalized fluorophores, measurements were done at the bottom of the nucleus. The obtained curves were fit using the freely available FoCuS-point software using 2D and triplet model.[97] Although it is possible that there are multiple diffusing populations (inner versus outer leaflet, protein interactions, lipid domains, etc) in these cellular experiments, the obtained FCS curves fit well to a single diffusing component, thus to avoid overfitting and overinterpretation, all FCS curves were fit to a single 'apparent' diffusion coefficient.

Lipidated protein binding to cell PM

The plasmid SH4-GFP was a kind gift from the Sarah Veatch lab (University of Michigan). Briefly, the N-terminal sequence of Lyn that codes for the myristol- and palmitoyl-acylation sites were inserted into the pEGFP-N1 vector (MGCIKSKRKDKDLELKLRILQSTV PRARDPPVAT – EGFP). The tH-KtoQ and tH-KtoA plasmids were generated from the tH-mEmerald plasmid (kind gift from John Hancock, University of Texas Health Science Center at Houston) that encodes for the two palmitoylation and one farnesylation sites of tH-Ras linked to an mEmerald fluorescent protein (mEmerald – SGLRSKLNPPDESGPGCMSC**K**CVLS*). The K (bold in previous sequence) was mutated to Q or A by site-directed mutagenesis to remove any additional electrostatic effects.

RBL cells at 70-80% confluency were harvested with 0.25% trypsin, and transfected with SH4-EGFP, mEmerald-tH-KtoQ or mEmerald-t-KtoA via electroporation. After 24 hours, cells were washed with PBS buffer, then maintained in Annexin V buffer (150 mM NaCl, 10 mM HEPES, 2 mM $CaCl_2$, pH 7.4, with 100 times diluted Annexin V AF647 from ThermoFisher, #A23204). Ionophore A23187 (Cayman, #11016) diluted in Annexin V buffer was added to the cells with a final concentration of 6 mM. Cells were imaged immediately after the addition of A23187 with a 63X water immersion objective on a Leica SP8 confocal microscope. Images were taken with 10 second intervals for up to 40 minutes.

Manipulation of plasma membrane lipids in RBL cells

For extraction and loading of phospholipids from/to cells, Hexakis-(2,3,6-tri-O-methyl)-alpha-Cyclodextrin, MαCD (CyclodextrinShop) was used. A stock solution was prepared in CaR buffer by incubation overnight at room temperature at a nominal concentration of 65 mM. Precipitates were removed by light centrifugation and pelleting, and the purity of the final clear solution was verified with dynamic light scattering.

RBL cells at 70-80% confluency were washed three times with CaR buffer and incubated with 6.5 mM (nominal concentration) MαCD in CaR buffer (or CaR buffer alone as parallel control) for 5 min at 37 °C. The supernatant was carefully removed and added to another washed plate of RBL cells and incubated for 5 min at 37 °C to fully saturate MαCD with outer leaflet PLs. The lipid-saturated MαCD-containing supernatant from this second incubation was then removed and spun through a 5 μ m centrifugal filter to remove any contaminating cells, producing a PL-loaded MαCD solution (PL-aCD). This filtered supernatant was then added to a fresh plate of RBL cells for 15 min at 4 °C (after washing 2x in cold CaR buffer). This solution was then removed, and fresh PL-aCD was added to the same plate for another 15 min at 4 °C. For DOPC loading, DOPC (Avanti Polar Lipids) was dissolved to 10 mM in 100% ethanol. This was then diluted to 0.1 mM in CaR buffer and added to cells at room temperature for 15 min.

For sphingomyelinase (SMase) treatment, ~25,000 RBL cells were treated with 0.1 U in Tyrode's buffer (25 mM HEPES, 150 mM NaCl, 5 mM KCl, 5.4 mM glucose, 1 mM CaCl2, 0.4 mM MgCl2, pH 7.2) for 20 min at 37 °C.

The abundance of phospholipids in the PL-aCD solutions was quantified with a colorimetric inorganic phosphate assay. After incubation of MαCD with cells to extract or load lipids, the supernatants from several samples were spun down to remove cell debris

(5 min at 200xg) and a fixed volume of the top fraction (500 μ L) from each was transferred to a 13 x 100 mm disposable glass culture tube (Fisher) for replicate measurements. Tubes were left uncapped on a hot plate at 94°C overnight to evaporate the solvent. The next day, tubes were removed from the hot plate and allowed to cool to room temperature. Each experiment contained at least 3 replicates and 3 controls, in addition to a set of 11 samples prepared from an inorganic phosphate standard solution (Phosphate Standard, LabChem) for a calibration curve covering a range of 0–61 nanomoles phosphate. All subsequent steps were performed identically on samples and calibration standards.

First, 200 μ L of 10% (v/v) sulfuric acid (Ricca Chemical) was added to each tube. The tubes were then returned to the hot plate and the temperature was set to 200°C. After 90 min, 20 μ L of 30% H_2O_2 (MilliporeSigma Supelco) was added directly to each tube on the hot plate followed by incubation for another 40 min. This step (addition of hydrogen peroxide and subsequent 40 min incubation at 200°C) was repeated until the solution was visibly transparent (typically four times). Tubes were then removed from the hotplate and allowed to cool to room temperature. A color reagent was prepared by mixing 0.5 mL 5% (w/v) ammonium molybdate (Thermo Scientific Chemicals) in H2O with 4.5 mL H2O and 0.1 g ascorbic acid (Spectrum Chemical), followed by vortexing until fully mixed. To each tube, 500 μ L of color reagent was added followed immediately by vortexing before moving on to the next tube. After all tubes received color reagent, 500 μ L of water was added to each tube followed again by immediate vortexing. The tubes were then moved to a 45°C water bath and incubated for 20 min. After removing the tubes from the water bath, absorbance was measured immediately at 820 nm on a UV/vis spectrometer (Mettler Toledo). The absorbance from each sample was converted to nanomoles phosphate using the calibration curve (Figure S8A).

The measurements from the phosphate assay revealed that the transfer of PL-aCD from donor to acceptor cells added 4 nmol of PLs to ~3×10^5 cells, which yields ~8.0×10^9 PL molecules/cell. From estimates of the typical surface area of mammalian cells (5,000 μm^2)[98] and the area/lipid in the PM outer leaflet (~40 $Å^2$/lipid, Figure 4C), we approximate a typical PM outer leaflet contains ~1.25×10^{10} lipids. According to these rough estimates, the delivered PLs represent ~40% of the PM outer leaflet after loading.

Quantification of cholesterol

Following incubation of cells with PL-MαCD, cells were scraped into 2% SDS, 50 mM Tris, 5 mM EDTA, pH 7.4 and sonicated for 3x 10s. An Amplex Red assay was performed (according to manufacturer instructions; Invitrogen) to determine total sterol abundance. A commercial BCA assay (Pierce) was performed to normalize the measured cholesterol amounts to total protein.

Imaging of cholesterol-binding proteins

RBL cells were transfected with EGFP-GRAM-H, EGFP-GRAMD1A, or EGFP-GRAMD1B (kind gift from Yasunori Saheki lab, Nanyang Technological University, Singapore) 48 h prior to the experiment via electroporation to give a final confluency of 40-50%. GRAMD1A and GRAMD1B were co-transfected with a PM-resident synthetic protein (trLAT).[99] For EGFP-GRAM-H, EGFP-GRAMD1A, or EGFP-GRAMD1B imaging, after PL-MαCD, DOPC, or SMase incubation, the cells were washed in CaR buffer and imaged at room temperature with a 63X water immersion objective on a Leica SP8 confocal microscope. 10–15 cells were quantified for each condition per experiment.

C-laurdan imaging

C-laurdan imaging was performed as previously described.[100,101] Briefly, after PL-MαCD incubation, the PL-MαCD supernatant was removed, cells washed 2x with PBS, and incubated with 5 μg/mL C-laurdan for 20 min at RT. Finally, the cells were washed with PBS and then imaged at room temperature with a 63X water immersion objective on a Leica SP8 confocal microscope with spectral imaging with excitation at 405 nm. The emission was collected as two images: 420–460 nm and 470–510 nm. MATLAB (MathWorks, Natick, MA) was used to calculate the two-dimensional (2D) GP map, where GP for each pixel was calculated as previously described.[102] Briefly, each image was background subtracted and thresholded to keep only pixels with intensities greater than 3 standard deviations of the background value in both channels. The GP image was calculated for each pixel with the following equation (where G is the G-factor and I_x is intensity at wavelength x):

$$GP = \frac{\sum_{420}^{460} I_x - G\sum_{470}^{510} I_x}{\sum_{420}^{460} I_x + G\sum_{470}^{510} I_x}$$

The G-factor was determined before each experiment using a previously published protocol.[101] GP maps (pixels represented by GP value rather than intensity) were imported into ImageJ. The average GP of the internal membranes was calculated by determining the average GP of all pixels in a mask drawn on each cell just inside of the PM. Histograms of the GP values for individual cells were determined and fit to two Gaussian peaks to isolated lipid droplet values from the other internal membranes. 10-15 cells were quantified for each condition per experiment.

Lipid droplet quantification

After PL-MαCD, DOPC, or SMase incubation, the cells were washed 2x with CaR buffer, and incubated in Tyrode's buffer for 45 min at 37 °C. After 45 min, 2 μ M Bodipy 493/503 (Thermo Fisher) in Tyrode's buffer was added to the cells and incubated at 37 °C for another 15 min. The cells were then washed in Tyrode's buffer 2x and imaged at room temperature with a 63X water immersion objective on a Leica SP8 confocal microscope with spectral imaging with excitation at 493 nm and emission from 503-603 nm. Z-stacks of images were taken every 1 μ m from just above to just below the cell to capture the entire cellular volume. Using ImageJ, the z-stacks were converted to a maximum projection. ROIs were drawn around the perimeter of the cells. Images were then background subtracted using the mean + 3x SD of background cellular signal. The total pixel intensity and percent area covered by non-zero pixels

were calculated on a per-cell basis. 15-25 cells were imaged for each condition per experiment. For ACAT inhibition the cells were treated with 1 ug/mL Sandoz 58-035 (Santa Cruz Technologies) overnight prior to the experiment and throughout the experimental incubations. For a positive control, cells were treated with 200 μM cholesterol in complete medium (water soluble, Sigma Aldrich) overnight.

QUANTIFICATION AND STATISTICAL ANALYSIS

Statistical tests used in this study are stated in the individual figure legends.

Supplemental figures

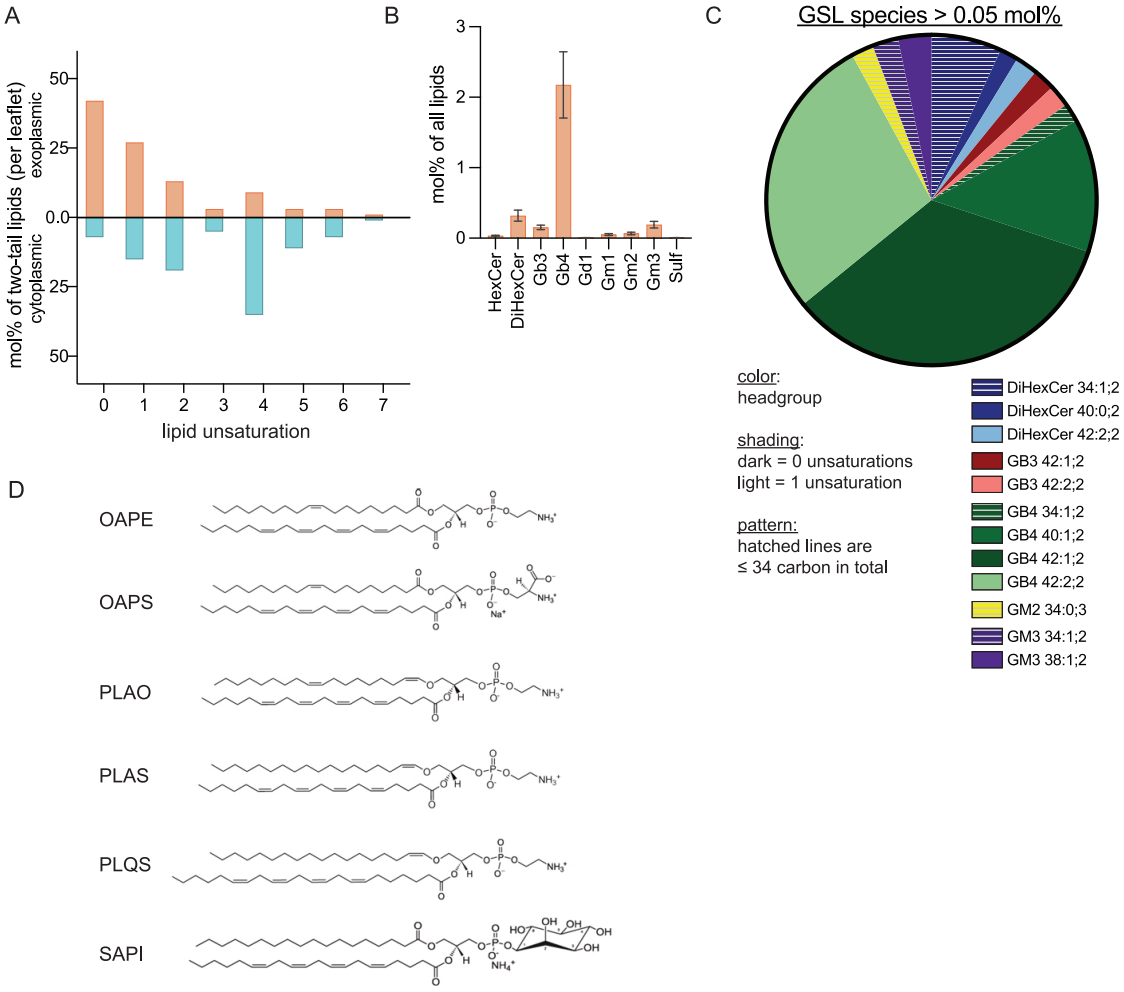

Figure S1. Lipidomics and lipid structures, related to STAR Methods

(A) Lipid unsaturation distribution for all lipids (including GSLs) in the exoplasmic and cytoplasmic leaflets show the exoplasmic leaflet is much more saturated.

(B) Distribution of GSL headgroups as mol % of all erythrocyte lipids.

(C) Abundance of all GSL species >0.05 mol % of erythrocyte lipids as a fraction of all GSLs. Color represents the GSL headgroup, shading represents the total unsaturation of the two acyl chains (not including the double bond in the Cer backbone). Hatched bars represent shorter GSLs, with $\leq$34 carbons in the two acyl chains combined.

(D) Names and structures of lipids used in the all-atom PM model simulations.

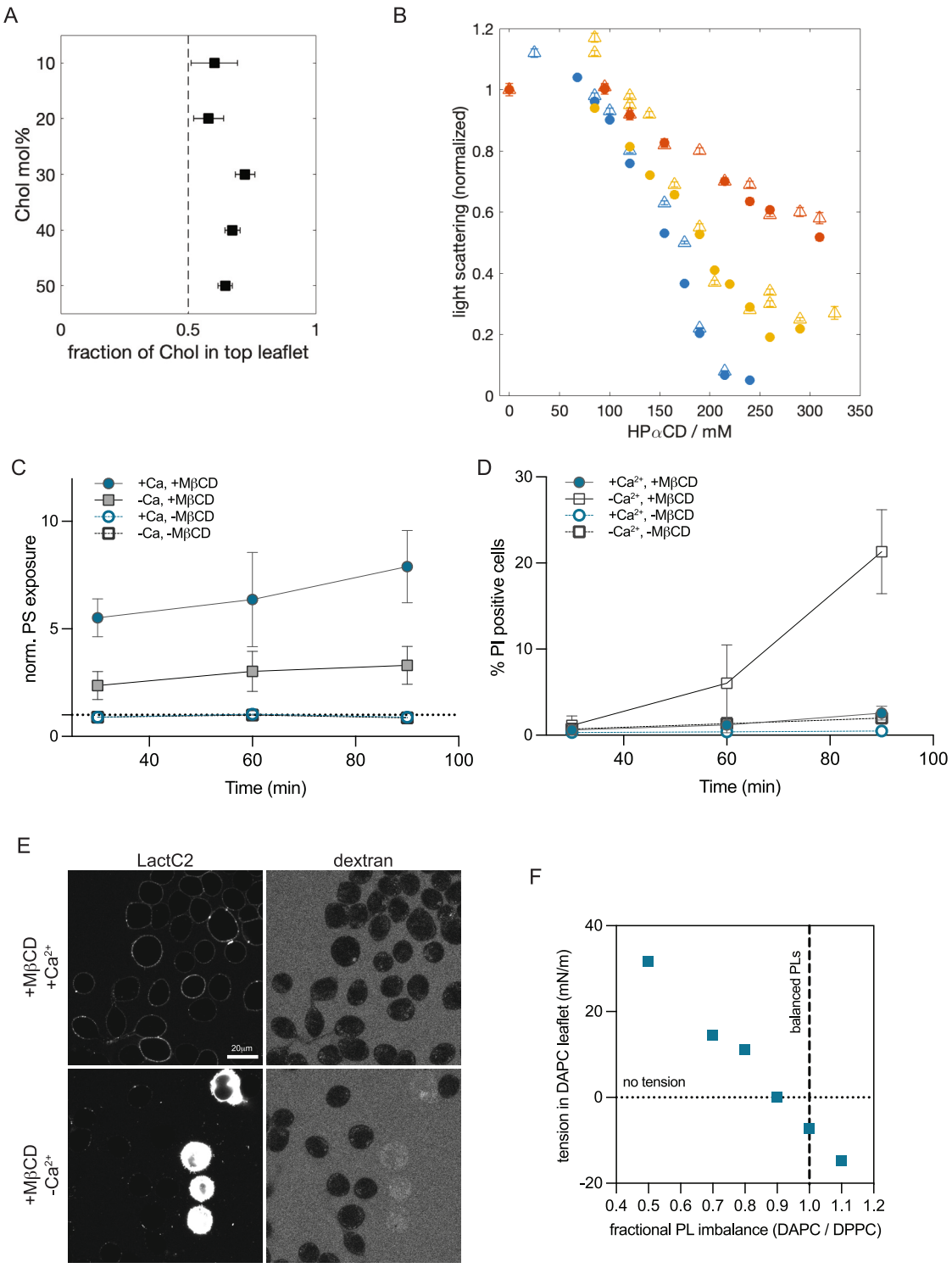

Figure S2. Chol effects in simulations and experiments, related to Figure 2

(A) In all coarse-grained simulations (each 10-μ s long), Chol accumulates in the "exoplasmic" top SM-rich leaflet. Specific leaflet lipid compositions and abundances are listed in Table S2.

(B) Dynamic light scattering measured for extruded 100-nm liposomes composed of POPC with 0 (blue), 20 (yellow), and 40 (red) mol % Chol and incubated with increasing concentrations of hydroxy-propyl-alpha cyclodextrin (HP α CD). HP α CD extracts POPC lipids (but not Chol) from the outer leaflet of the

(legend continued on next page)

membranes. A decrease in light scattering indicates destruction of the liposomes due to increased PL imbalance. Chol decreases liposome solubilization by HP α CD. Circles and triangles indicate independent replicate experiments.

(C) Time course of PS exposure on the surface of RBL cells treated with M β CD either in the presence or absence of calcium. PS exposure measured via binding of PS-marker LactC2-mClover and normalized to the respective $-$M β CD conditions.

(D) Time course of membrane integrity in RBL cells treated with M β CD in the presence or absence of calcium. Membrane integrity was measured by percentage of cells with PI stained nuclei. PI is not membrane permeable and therefore only stains cells with disrupted PM integrity. Saponin treatment was used as a positive control, leading to 100% of cells becoming PI positive.

(E) Membrane disruption can also be measured by leakage of fluorescent dextran into the cytoplasm. Images show RBL cells treated with M β CD either in the presence (top) or absence (bottom) of calcium for 90 min at 23°C. The former results in PS exposure and preserved membrane integrity as evidenced by impermeability to dextran. M β CD treatment in the absence of calcium suppresses PS exposure and compromises membrane integrity, with some cells becoming permeable both to dextran and LactC2 (which has a similar size).

(F) Asymmetric bilayers with 30 mol % Chol and one fully saturated DPPC leaflet opposing a highly unsaturated DAPC leaflet with varying relative number of lipids. Chol re-distributes due to both its preference for saturated lipids and the PL imbalances between leaflets, as evidenced from long coarse-grained simulations (Figure 3B). Fully atomistic trajectories of the equilibrated bilayer compositions (Table S4) were used to calculate the tension in all membrane leaflets. As the relative PL abundance in the DAPC leaflet (i.e., number of DAPC/number of DPPC) decreases, the tension in the DAPC leaflet increases.

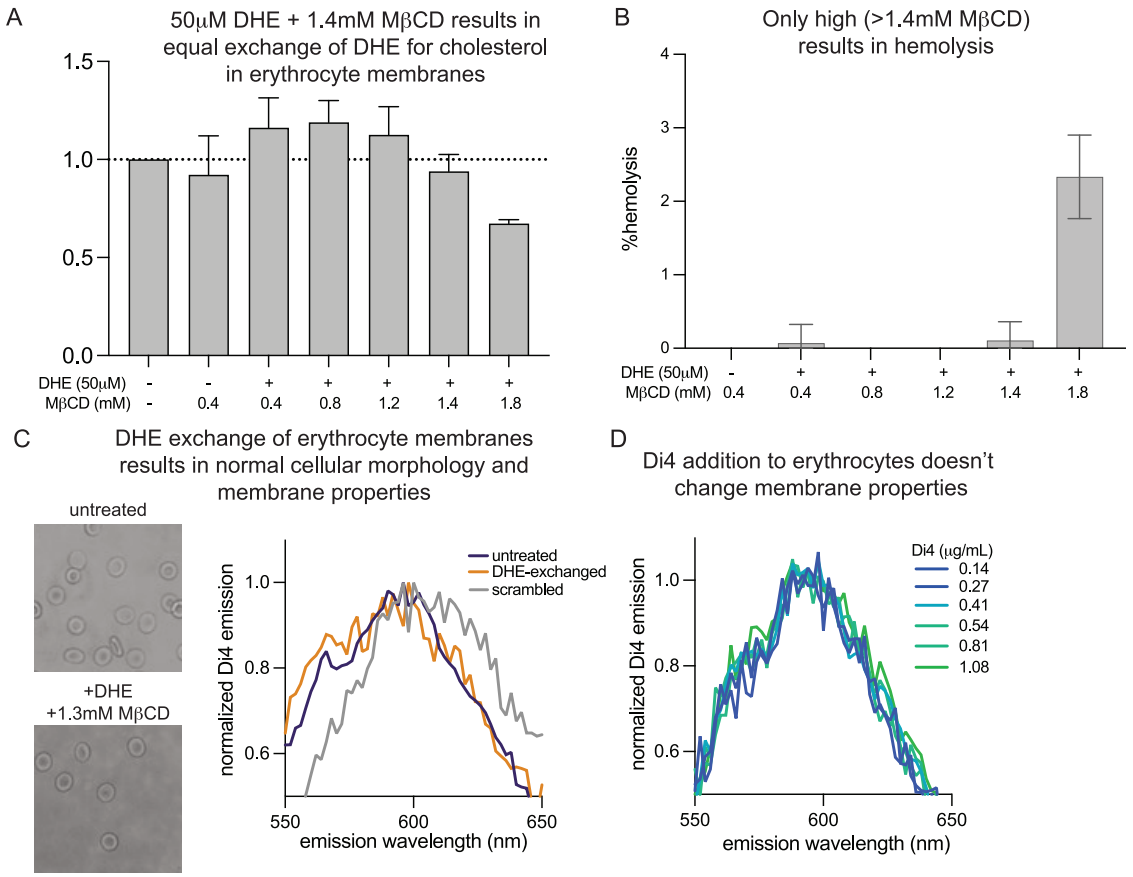

Figure S3. Optimization of DHE exchange conditions in erythrocytes, related to STAR Methods

(A) Incubation of 50 μ M DHE with 1.2–1.4 mM M β CD yields a 1-to-1 exchange of DHE for Chol and maintains integrity of PM sterol composition as determined by Amplex Red of erythrocyte membranes after exchange.

(B) M β CD concentrations greater than 1.4 mM result in erythrocyte hemolysis.

(C) Erythrocytes with DHE exchanged for Chol at optimized conditions (1.3 mM MβCD + 50 μ M DHE) do not exhibit altered cellular morphology (left) or lipid packing as measured by lack of shift in Di4 emission spectra (right). Gray line shows erythrocytes scrambled by treatment with 100 mM PMA for 10 min to illustrate a perturbation in membrane properties.

(D) Addition of Di4 to erythrocytes does not change membrane properties as indicated by lack of shift in Di4 emission spectra.

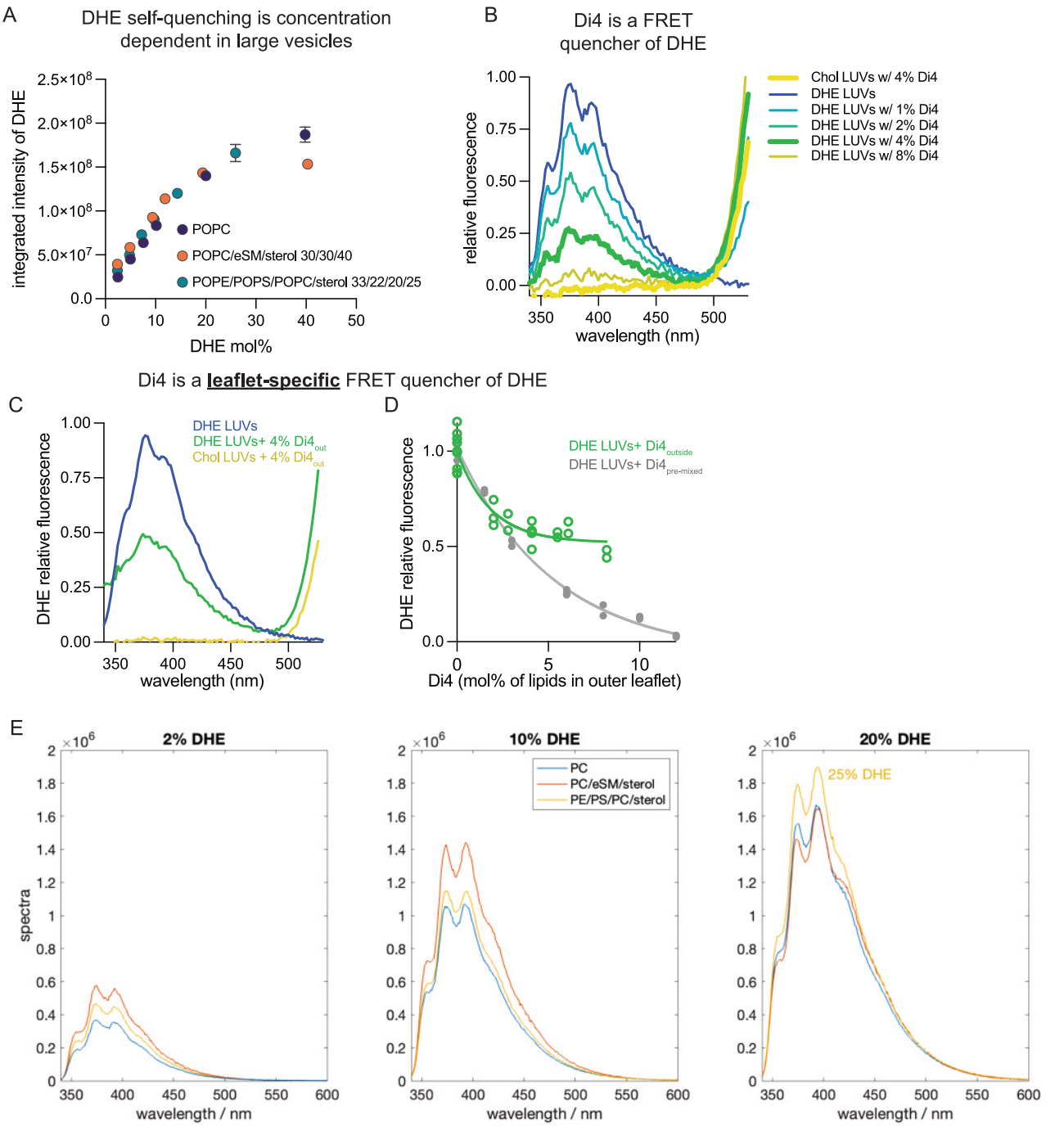

Figure S4. Quenching of DHE, related to STAR Methods

(A) DHE fluorescence in large liposomes with increasing amounts of DHE. The liposomes were prepared with the indicated lipid compositions where the added DHE either replaced part of the lipid (for POPC-only) or the sterol (for the multi-component mixtures) in the membrane. All lipid and DHE were mixed in organic solvent and prepared via rapid solvent exchange as detailed in STAR Methods. Since increasing amounts of DHE result in changes in the shape of the emission spectra, the integrated intensity of the full spectra is used for comparison between the samples. A clear linear regime is observed up to ~10–15 mol % DHE followed by a deviation from it indicating DHE self-quenching at higher concentrations. This behavior is independent of lipid composition as it is observed in mixtures with a wide range of fluidity.

(B) Effect of Di4 on DHE fluorescence in extruded large unilamellar vesicles (LUVs) composed of 40% sterol (including 2.5% DHE), 5% POPG, and 55% (DOPC + Di4). Controls with Chol (instead of DHE) and DHE with no Di4 show the range of DHE fluorescence between 350 and 500 nm. Increasing amounts of Di4 (premixed with the lipids) reduce DHE fluorescence until it is barely detectable at Di4:DHE of ~3:1.

(legend continued on next page)

(C) Externally added Di4 at 8 mol % of outer leaflet lipids quenches roughly half of the 2.5 mol % DHE symmetrically distributed in the LUVs composed of 40% sterol, 5% POPG, and 55% DOPC.

(D) Increasing amounts of Di4 added externally to LUVs progressively reduces DHE fluorescence measured at 385 nm, plateauing at ~50%. The data demonstrate that when added from the outside, Di4 preferentially quenches outer leaflet DHE.

(E) Representative spectra of DHE in liposomes (large vesicles prepared by rapid solvent exchange) composed of POPC (PC), egg SM (eSM), POPE (PE), POPS (PS), and Chol (lipid compositions same as in (A) with increasing amounts of DHE indicated in the title of each plot. The shape of the spectra changes at higher DHE concentrations, making trends with composition or DHE content dependent on the choice of wavelength. This problem can be circumvented by integration of the spectra.

Discussion of previous measurements of DHE asymmetry: Chol asymmetry has proven difficult to define because sterols rapidly flip-flop between leaflets.[18,103–105] This rapid equilibration presents a unique difficulty in trying to measure Chol's residence in a single leaflet, since all Chol molecules sample both leaflets frequently.[17] Unsurprisingly, previous reports have diverged dramatically: a report in the 1970s claimed ~3-fold enrichment in the outer leaflet,[106] contradicted 15 years later by claims of 3-fold enrichment in the cytoplasmic leaflet.[107] More recently, evidence for cytoplasmic,[108–110] exoplasmic,[111–113] or neither[114] leaflet being Chol enriched has been presented. In recent years, two high-profile papers again presented conflicting claims of either strong inner PM leaflet enrichment[115] or almost exclusive enrichment in the outer leaflet.[52]

Methods relying on DHE quenching, similar to our approach, have also been used previously to infer Chol asymmetry. In both yeast and mammalian cells, quantifying DHE fluorescence intensity by imaging cells before and after addition of external DHE quenchers was used to conclude that most DHE (and by inference, most Chol) resided in the cytoplasmic PM leaflet.[108,109] The yeast experiments were cleverly constructed to allow essentially all (native) ergosterol to be replaced by fluorescent DHE. However, one potential issue with this approach is the strong self-quenching of DHE at high concentrations, which has been previously reported[96] and which we reproduce here in (A). Such self-quenching is likely to affect conclusions based on external quenching in cell PMs and this problem would be especially acute if sterol is asymmetrically distributed. An extreme, illustrative case would be one leaflet with high DHE concentration leading to complete self-quenching, while the other leaflet has low, sub-self-quenching concentration. In this case, most (or even all) observable fluorescence could come from the leaflet with *lower* DHE concentration. In our experiments, we avoided the possibility of self-quenching by minimizing the fraction of DHE exchanged into erythrocytes, keeping it below 10% of all PM lipids.

Further, previous experiments often relied on highly reactive oxidizing quenchers like trinitrobenzenesulfonic acid (TNBS), which covalently react with biomolecules and lead to cellular toxicity. We used a bio-orthogonal fluorophore (Di4) as the fluorescence quencher, with the added benefit that Di4 also reports on changes in membrane properties (or lack thereof in our measurements; see Figures S3C and S3D). However, while our measurements strongly support enrichment of sterol in the outer PM leaflet, they do not provide absolute quantification of molar enrichment between leaflets (see STAR Methods). Absolute quantification would require detailed information about how the spectral properties of both the donor (DHE) and acceptor (Di4) depend on various membrane environments, absolute quantifications of their lateral density in erythrocyte membranes, and careful modeling to interpret and frame the results. Such characterization is outside the scope of the present study. Further, we emphasize that sterol asymmetry is likely to vary between cell types and almost certainly between yeast and mammalian cells. Thus, our study does not absolutely contradict previous reports.

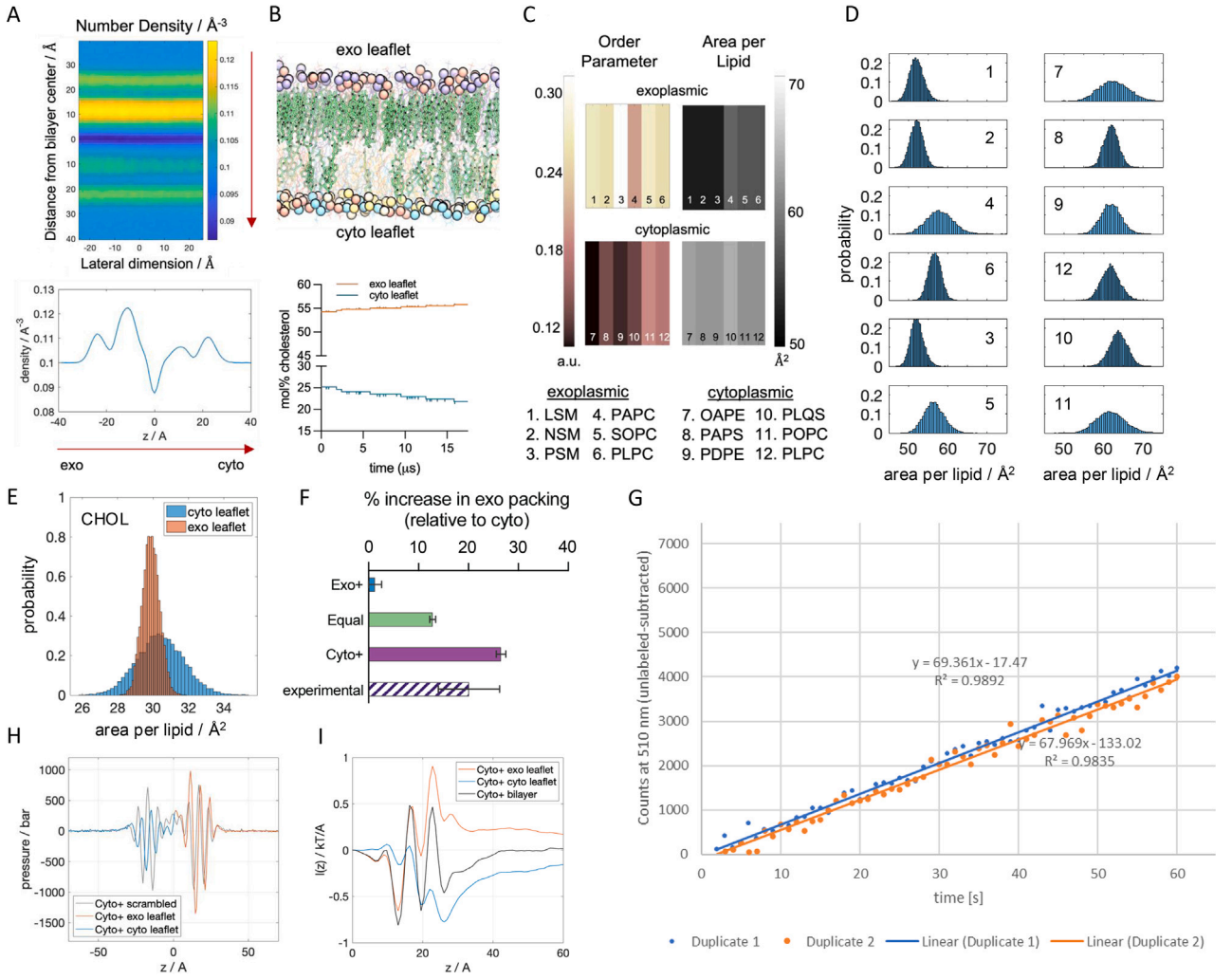

Figure S5. Structural properties of PM, related to Figure 5 and STAR Methods

(A) (Top) Number density of all atoms (including lipids and water) calculated in 3D and projected onto the xz plane. y axis of the heatmap shows distance from bilayer center and from top to bottom goes through water region, exoplasmic leaflet, bilayer center, cytoplasmic leaflet, and water region, as indicated by the red arrow (as shown in B for reference). (Bottom) Laterally averaged number density profile for more direct quantitative comparison of the density peaks.

(B) (Top) Snapshot of the equilibrated simulated Cyto+ membrane (as detailed in the caption of Figure 1D). Water atoms not shown. (Bottom) Chol concentration (expressed as mol % of each leaflet) in the Cyto+ membrane shows the time evolution of Chol interleaflet distribution.

(C) Average order parameter (left) and APL (right) for each type of lipid in the exoplasmic (top) and cytoplasmic (bottom) leaflets. Order parameter was averaged over all carbon atoms on both chains. APL was calculated from Voronoi tessellation analysis detailed in STAR Methods, where lipid names and structures are also detailed.

(D) Histograms of individual lipid areas for exoplasmic (left) and cytoplasmic (right) leaflet lipids whose averages are shown in the heatmaps in (C).

(E) Histograms of the lipid areas of Chol in the exoplasmic (SM) leaflet and cytoplasmic (PUFA) leaflet calculated from Voronoi analysis in every frame of the trajectory. The analyses in (A) and (C)–(E) are from the last 1.2 μ s of the trajectory.

(F) Comparison of the area/lipid difference between exoplasmic and cytoplasmic leaflets in simulations versus experiments (shown as percent increase in the packing: $[APL_{cyto} - APL_{exo}]/APL_{cyto}$). Experimental measurements represent APLs inferred from Di4 lifetime measurements in fibroblast 3T3 cells and the calibration curve in Figure 4A. The Cyto+ model is within error of experiment, while the Exo+ and Equal models are significantly different.

(G) Flux of FDA across the PM of intact untreated erythrocytes is measured via the slope of linear increase in fluorescein fluorescence (due to cytoplasmic FDA hydrolysis). Two representative replicates are shown with linear fits.

(H) Lateral pressure profiles of the asymmetric Cyto+ bilayer (with the Exo and Cyto leaflets colored red and blue, respectively) and its symmetric scrambled counterpart (gray). Scrambling membrane lipids equalizes the lipid compositions of the two leaflets and makes the pressure distribution on the two sides of the bilayer midplane (z = 0) the same.

(I) First moment of the pressure profile for each leaflet in the Cyto+ membrane and their sum, i.e., for the bilayer. The plateau values far from the membrane (i.e., at large z values) represent the torque densities of either individual leaflets or the whole bilayer. Torque density quantifies the propensity for a membrane to curve, with positive values representing positive curvature and vice versa. Torque density close to zero implies a bilayer with a tendency to remain flat. In the Cyto+ bilayer, although both individual monolayers have a significant torque density, the net bilayer torque density is essentially 0, indicating that differential and curvature stresses in the membrane are balanced and result in preference for flat morphology.

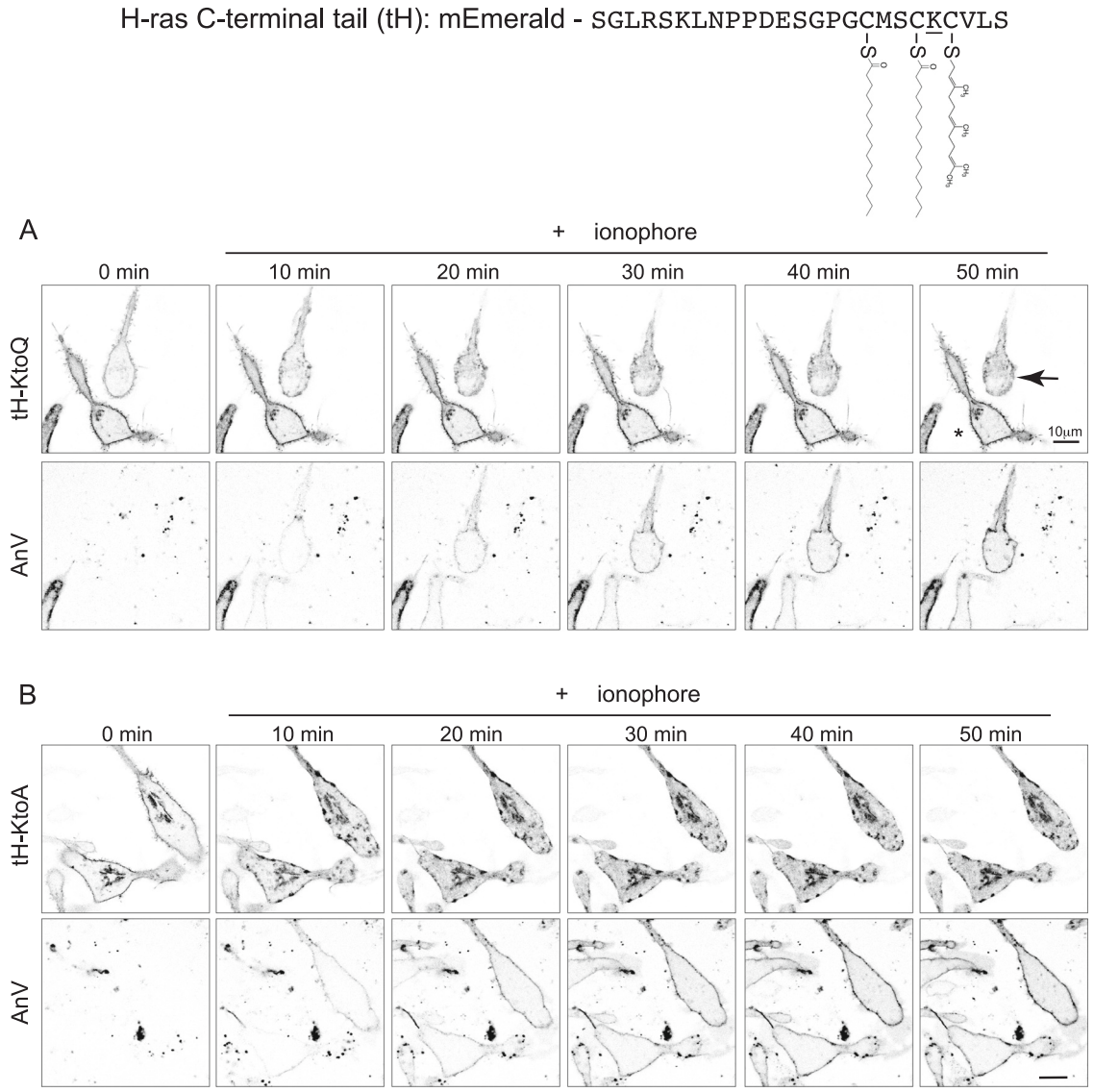

Figure S6. Effects of PM lipid scrambling on the interaction of lipidated peptides with the membrane's cytoplasmic leaflet, related to Figure 5

(A and B) Confocal images of the cellular distribution of two variants of the tH-Ras peptide in RBL cells following membrane scrambling. tH-Ras is composed of the 20 C-terminal amino acids of H-Ras, which contains its farnesylation signal (CAAX) and two sites for palmitoylation; thus, this peptide has up to 3 lipid anchors. The peptide is tagged with mEmerald for visualization. To eliminate the possibility of electrostatic interactions, we mutated the lysine of the peptide which is located between the farnesyl and palmitoyl chains to either glutamine (A) or alanine (B). The sequence of the probe is given, with the acylation sites noted and mutated lysine underlined. Scrambling of PM lipids was initiated with the ionophore A23187 while exposure of PS on the cell surface was monitored with AnxV Alexa Fluor 647. Both variants of the peptide localized largely to the PM at steady state but redistributed to inner membranes upon release of asymmetry (indicated by AnV binding). The favorable interaction with the asymmetric PM is consistent with hydrophobic defects present in the cytoplasmic leaflet (Figures 5E and 5F), which promote the insertion of the lipid anchors and disappear after PM scrambling. As a control, in (A) the cell marked with an asterisk does not scramble during this time course, and the peptide remains at the PM; in contrast, the cell marked with an arrowhead does scramble, and the peptide is redistributed to inner membranes.

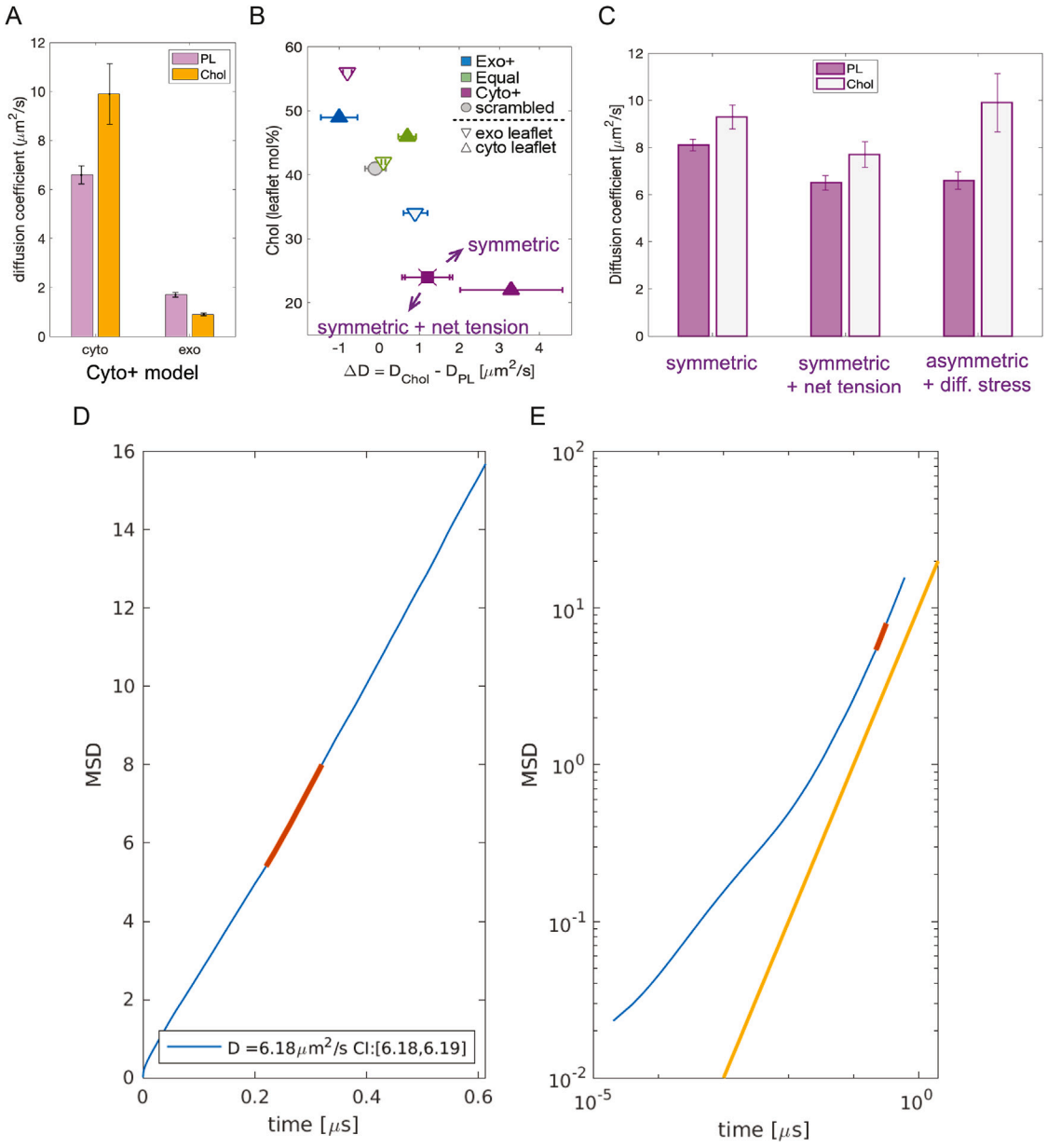

Figure S7. Lipid diffusion in simulations, related to STAR Methods

(A) PL and Chol diffusion in each leaflet of the Cyto+ membrane.

(B) Difference between Chol (D_{Chol}) and PL (D_{PL}) diffusion ΔD in each leaflet of the three PM models and the Cyto+ scrambled membrane is plotted versus Chol concentration in the leaflet. A high correlation between the two shows that the cytoplasmic leaflet of the Cyto+ model, which is differentially stressed and has tension of ~8 mN/m, has the largest ΔD. A symmetric membrane with the same lipid composition has a smaller ΔD both in the absence (symmetric) or presence of 8 mN/m net tension (symmetric + net tension). These results indicate that the fast diffusion of Chol relative to PLs is related to both low Chol concentration in the leaflet and tension arising from differential stress.

(C) PL and Chol diffusion coefficients in mixtures having the lipid and Chol composition of the cytoplasmic leaflet of the Cyto+ model: symmetric membrane with no differential stress or tension (left), symmetric membrane with applied net tension (middle), and the Cyto leaflet of the Cyto+ model which has differential stress of the same magnitude (right). These results show that tension of 8 mN/m reduces PL diffusion to the same extent, irrespective of its source; however, Chol diffusion is only slightly affected by differential stress and to a much greater extent by net bilayer tension. Thus, differential stress contributes to a large ΔD by its differential effects on PL and Chol diffusion.

(D and E) Representative plots showing mean square displacement (MSD) as a function of time in a linear (D) and a log-log (E) scale. Red indicates the 100-ns block from which the diffusion coefficient was calculated (see STAR Methods). Data shown are for the PLs in the cytoplasmic leaflet of the Cyto+ model.

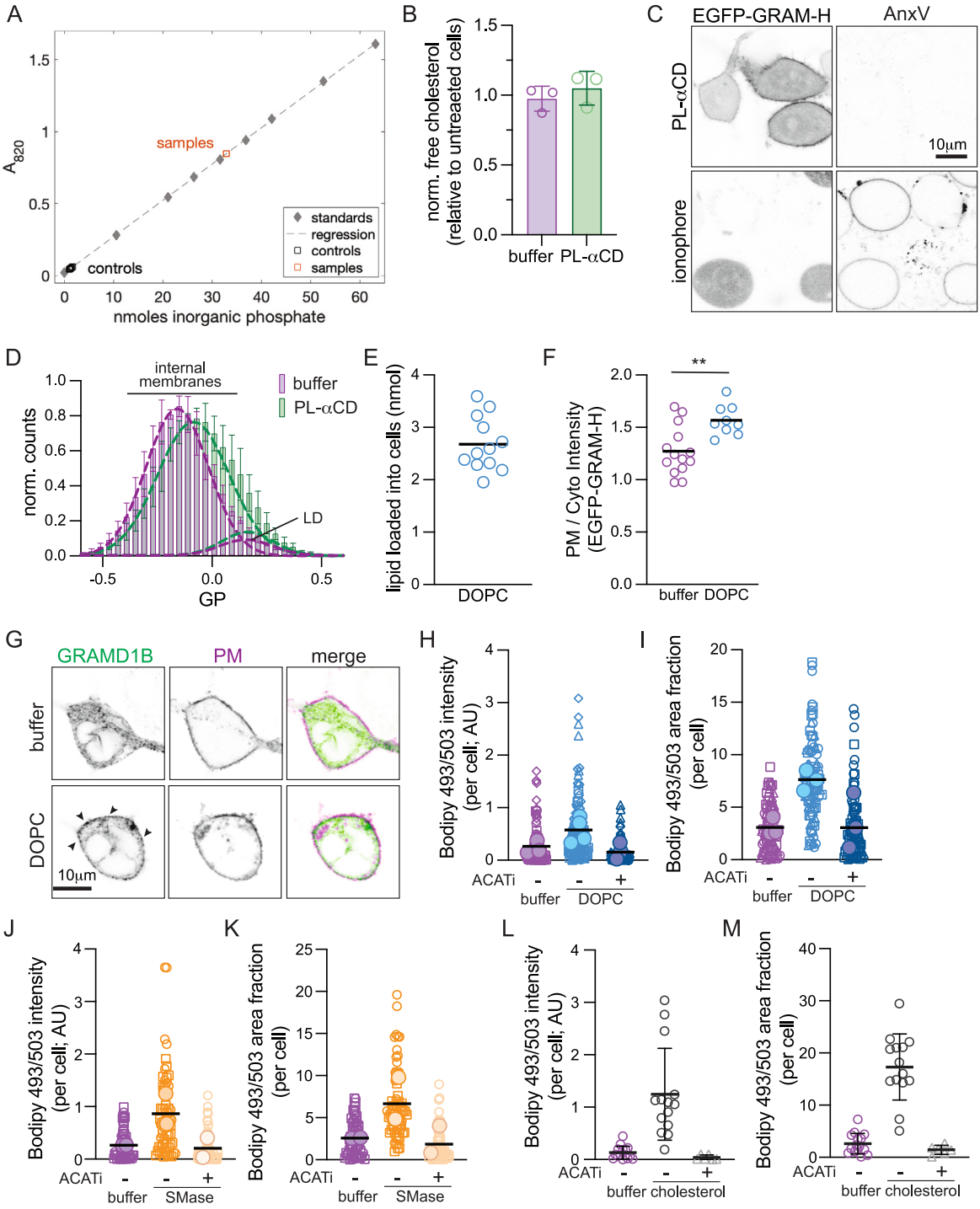

Figure S8. Manipulation of PM outer leaflet composition, related to Figure 7

(A) Calibration curve of phosphate standards (diamonds) used to quantify the nanomoles lipid in a sample (orange squares) relative to controls (black squares). Data shown are for two replicates of MαCD solution after incubation with cells to extract lipids. Corresponding controls were done with the same conditions but in the absence of MαCD.

(B) Chol abundance in cells treated with PL-αCD relative to protein amount and normalized to untreated cells. Analyzed by AmplexRed assay; data points represent independent experiments.

(C) AnxV staining of cells treated with PL-αCD or 3 mM A23187 as a positive control. PL-αCD treatment does not induce PS scrambling as indicated by a lack of AnxV external staining.

(legend continued on next page)

(D) Histograms of C-Laurdan GP in cells. To determine the GP of the internal membranes (i.e., non-LD), a histogram of all pixels excluding the PM was generated (for each experiment), and the data fit to two Gaussian peaks (with one mean fixed at GP > 0.1, representing the very high GP of LDs). PL-αCD treatment results in a higher amplitude for the LD peak (more LD) and a higher mean for the internal membranes (tighter lipid packing).
(E) The abundance of DOPC loaded into cells quantified by phosphate assay.
(F) EGFP-GRAM-H translocation to the PM in DOPC-loaded cells.
(G) Imaging of RBL cells expressing full-length EGFP-GRAMD1B and trLAT (PM marker) with and without DOPC treatment. Arrowheads show translocation of GRAMD1B to the PM after DOPC treatment.
(H and I) Quantification of LDs in DOPC-treated cells with and without ACAT inhibition (1 μg/mL Sandoz 58-035).
(J and K) Quantification of LD in SMase-treated cells with and without ACAT inhibition (1 μg/mL Sandoz 58-035).
(L and M) Quantification of LD in Chol-loaded cells with and without ACAT inhibition (1 μg/mL Sandoz 58-035).
Using maximum projection of volumetric imaging, the total intensity of staining (H, J, and L) and area fraction covered by LDs (I, K, and M) are reported. In (F), (H)–(J), (L), and (M), small symbols represent individual cells, with symbol shapes denoting independent experiments. Filled larger symbols are means of independent experiments.

Cell, Volume *188*

Supplemental information

Cell membranes sustain phospholipid imbalance via cholesterol asymmetry

Milka Doktorova, Jessica L. Symons, Xiaoxuan Zhang, Hong-Yin Wang, Jan Schlegel, Joseph H. Lorent, Frederick A. Heberle, Erdinc Sezgin, Edward Lyman, Kandice R. Levental, and Ilya Levental

Ref	Species	Leaflet	Mol% of lipid class					Mol% of total lipids						Relative PL abundance cyto/exo
			SM	PC	PE	PI	PS	SM	PC	PE	PI	PS	Total PLs	
1	Human	exo-	85	68	0	-	0	21.25	19.99	0.00	-	0.00	41.24	1.34 [1.23; 1.42]
		cyto-	15	32	100	-	100	3.75	9.41	27.00	-	15.00	55.16	
		overall						23.50	29.40	27.00	3.00	15.00	97.90	
14	Rat	exo-	100	48	8	0		12.00	20.16	2.00	0.00		34.16	1.78 [1.55; 1.93]
		cyto-	0	52	92	100		0.00	21.84	23.00	16.00		60.84	
		overall						12.00	42.00	25.00	16.00		95.00	
13	Human	exo-	85	68	0	-	0	19.98	19.99	0.00	-	0.00	39.97	1.37 [1.22; 1.5]
		cyto-	15	38	100	-	100	3.53	9.41	27.00	-	15.00	54.93	
		overall						23.50	29.40	27.00	3.00	15.00	97.90 [a]	
15	Mouse	exo-	85	30	20	42	0	9.78	13.62	4.86	1.72	0.00	29.98	2.21 [1.95; 2.34]
		cyto-	15	70	80	58	100	1.73	31.78	19.44	2.38	10.80	66.12	
		overall						11.50	45.40	24.30	4.10	10.80	96.10	
16	Monkey	exo-	82	42	5	0	0	12.87	16.17	1.38	0.00	0.00	30.42	2.19 [1.98; 2.29]
		cyto-	18	58	95	100	100	2.64	22.33	26.22	5.10	10.20	66.49	
		overall						15.50	38.50	27.60	5.10	10.20	96.90	
6	Human	exo-	89	48	4	0	15	14.98	14.57	1.10	0.00	1.46	32.11	2.02 [1.84; 2.11]
		cyto-	11	52	96	100	85	1.85	15.78	26.51	1.26	19.41	64.81	
		overall						16.83	30.34	27.62	1.26	20.87	96.92	

Table S1. Re-analyzed lipidomics data from literature, related to Figure 1. Combining previous reports of overall phospholipid (PL) compositions for the PMs of various mammalian erythrocytes with reported asymmetries for specific lipid classes allowed us to calculate the relative PL abundances of each leaflet. Note that the sum of exo and endo lipids as mol% of total lipids is different from the total overall lipids for the cases where the asymmetry of PI was not reported. Last column shows the relative PL abundances in the cyto and exo leaflets with upper and lower bounds calculated by placing all non-reported lipids either in the exo or endo leaflet. Reported quantities are with white background, and calculated ones are shaded in color.

system	exoplasmic leaflet				cytoplasmic leaflet				
	PSM	PLPC	Chol	total	PDPE	PAPS	PLPC	Chol	total
A10	45	45	10	100	40	40	41	14	135
A20	40	40	20	100	36	36	36	27	135
A30	35	35	30	100	31	31	32	41	135
A40	30	30	40	100	27	27	27	54	135
A50	25	25	50	100	22	22	23	68	135

Table S2. Leaflet compositions of CG bilayers used to test cholesterol effect on bilayer tolerance for PL mismatch, related to Figure 2. Number of lipids used to construct asymmetric coarse-grained (CG) bilayers mimicking the cell PM and having varying Chol concentration. Each bilayer has 35% more phospholipids in the model cytoplasmic leaflet, and the same starting concentration of Chol in both leaflets. The corresponding lipid names in Martini are DPSM (PSM), PEPC (PLPC), PRPE (PDPE) and PAPS (PAPS). Shown are the numbers of Chol molecules in each leaflet at the beginning of the simulation.

bilayer	# lipids (POPC/POPS/Chol)		# flipped lipids		Simulation length (ns)	
	top	bottom	POPS	Chol	analysis	total
0PS	64 / 16 / 20	64 / 16 / 20	0	0	460	960
1PS	64 / 15 / 20	64 / 17 / 20	1	0	650	900
1PS-1Ch	64 / 15 / 21	64 / 17 / 19	1	1	910	1050
1PS-2Ch	64 / 15 / 22	64 / 17 / 18	1	2	806	806
5PS	64 / 11 / 20	64 / 21 / 20	5	0	500	750
5PS-5Ch	64 / 11 / 25	64 / 21 / 15	5	5	970	1020
5PS-10Ch	64 / 11 / 30	64 / 21 / 10	5	10	880	1013
5PS-13Ch	64 / 11 / 33	64 / 21 / 7	5	13	806	806

Table S3. All-atom simulations for studying the effect of PS flipping on leaflet tension, related to Figure 3. Shown are the numbers of POPC, POPS, and Chol in each leaflet of the simulated bilayers and the effective number and type of *flipped* lipids modeled by the system (POPS is always "flipped" from the top to the bottom leaflet while Chol is "flopped" from the bottom to the top leaflet). The total length of the respective trajectories and the length of the last portion used for analysis are indicated in the last two columns (the latter was chosen based on equilibration of the bilayer area). Each bilayer was hydrated with 45 waters per lipid and charge-neutralized with potassium ions.

bilayer	start CG (DPPC/DAPC/Chol)		end CG / start AA (DPPC/DAPC/Chol)		AA simulation length (ns) analysis / total
	top	bottom	top	bottom	
A.5	70 / 0 / 30	0 / 35 / 15	70 / 0 / 29	0 / 35 / 16	400 / 1260
A.7	70 / 0 / 30	0 / 49 / 21	70 / 0 / 37	0 / 49 / 14	392 / 1130
A.8	70 / 0 / 30	0 / 56 / 24	70 / 0 / 43	0 / 56 / 11	400 / 1102
A.9	70 / 0 / 30	0 / 63 / 27	70 / 0 / 47	0 / 63 / 10	400 / 1060
A.10	70 / 0 / 30	0 / 70 / 30	70 / 0 / 52	0 / 70 / 8	400 / 1040
A.11	70 / 0 / 30	0 / 77 / 33	70 / 0 / 56	0 / 77 / 7	400 / 1077
A.12	70 / 0 / 30	0 / 84 / 36	-	-	-
A.13	70 / 0 / 30	0 / 91 / 39	-	-	-

Table S4. Coarse-grained and all-atom simulations for investigating the determinants of cholesterol distribution in lipid bilayers, related to Figure 3. Name of each system, initial numbers of lipids in each leaflet in the CG simulations, and the equilibrated numbers of lipids from the 10-μs-long trajectories. The latter were used to construct corresponding AA bilayers whose leaflet compositions did not change in the course of the production runs. Both the total length of the respective trajectories and the length of the last portion used for analysis are indicated for each simulation. Bilayers A.12 and A.13 did not tolerate the lipid number mismatch between the leaflets and exhibited an altered morphology as shown in Figure 2A in the main text. They were not used for subsequent simulation and analysis in AA representation.

model	exoplasmic leaflet		cytoplasmic leaflet		cholesterol exo/cyto number (leaflet mol%)	
	lipid	number	lipid	number	beginning	end
Cyto+	LSM NSM PSM PAPC PLPC SOPC	12 14 18 6 20 10	OAPE PAPS PDPE PLQS PLPC POPC	8 30 18 20 20 8	95/35 (54/25)	101/29 (56/22)
total		80		104	130	
Equal	LSM NSM PSM PAPC PLAS PLPC SAPS SOPC	54 63 81 36 18 99 9 45	DPPC PSM OAPE OAPS PAPS PDPE PLAO PLPC PLQS POPC POPE SAPI	16 8 25 8 82 49 16 57 57 25 16 16	267/261 (40/41)	294/234 (42/38)
total		405		375	528	
Exo+	LSM NSM PSM PAPC PLPC SOPC	16 18 22 8 28 12	OAPE PAPS PDPE PLQS PLPC POPC	6 22 14 16 16 6	35/95 (25/54)	54/76 (34/49)
total		104		80	130	

Table S5. Phospholipid and cholesterol compositions of simulated PM models, related to Figures 4 and 5. The compositions of three simulated PM models (Cyto+, Equal, Exo+), with types and numbers of lipids in each leaflet, as well as the corresponding number and leaflet mol% of cholesterol at the beginning and end of the simulations. Figure S1 shows the structures and full names of all lipids.

bilayer	initial anton run (μs)	subsequent NAMD run (μs)		diffusion analysis (μs)
		$\gamma = 5$ (ps)	$\gamma = 1$ (ps)	
Cyto+	15	0.4	2	2
Equal	25	-	1.51	1.5
Exo+	22.8	-	3.15	2.7
Cyto+ exo-sym	3	-	3	2.5
Cyto+ cyto-sym	3	-	1	1
Cyto+ scramble	5	-	1.4	1.24

Table S6. Trajectory lengths of fully atomistic PM models, related to STAR Methods. Production runs of the PM models and their symmetric counterparts were simulated first on the Anton supercomputer with the Desmond software, then with NAMD. Short NAMD trajectories with Langevin damping coefficient $\gamma = 5$ ps were followed by longer ones with γ set to 1 ps; last 1.2 μs (or 1 μs for Cyto+ cyto-sym) were used for most subsequent analyses. Last column shows the total length of the last portion of the NAMD trajectories with $\gamma = 1$ ps used for calculation of lipid and cholesterol diffusion coefficients.